ABSTRACT

SRIKANTH, VISHAL. Numerical Simulations of Turbulence in Porous Media – A Study on the Vortex Structure and Vortex Interactions at the Pore Scale (Under the direction of Dr. Andrey V. Kuznetsov).

Turbulent microscopic flow is simulated in homogeneous porous media using numerical methods by employing the Large Eddy Simulation (LES) and Reynolds Averaged Navier-Stokes (RANS) modelling techniques. Turbulence model independence is verified using Direct Numerical Simulation (DNS). A periodic domain consisting of a single Turbulence Representative Elementary Volume (REV-T) represents the porous medium in simulations. Since the Benard-von Karman vortex street, which is a product of the von Karman instability, cannot occur in porous media with low porosity, a build-up of vortices in the void space is observed to cause a complex interaction between the vortices. When the von Karman instability emerges in microscopic flow in a homogeneous porous medium with periodically arranged solid obstacles, the confinement that is inherent in the medium causes the macroscopic flow to deviate from the principal flow direction. The causation is investigated and several governing parameters are identified. A breakdown of the transient process from aligned to deviatory flow is provided to illustrate the developmental stages. A suitable explanation as to why the deviation is sustained is provided as well.

Numerical Simulations of Turbulence in Porous Media – A Study on the Vortex Structure and Vortex Interactions at the Pore Scale

by
Vishal Srikanth

A thesis submitted to the Graduate Faculty of
North Carolina State University
in partial fulfillment of the
requirements for the degree of
Master of Science

Mechanical Engineering

Raleigh, North Carolina

2018

APPROVED BY:

_____	_____
Dr. Andrey V. Kuznetsov Committee Chair	Dr. Pramod Subbareddy
_____	
Dr. Tarek Echekki	

BIOGRAPHY

Vishal Srikanth was born and raised in Chennai, India. He attended university in Coimbatore, India to obtain his undergraduate degree in Aerospace Engineering. To continue his studies, he enrolled in a Master's program in Mechanical Engineering at NC State University. At NC State, he works at the Computational Bio Fluids and Heat Transfer Laboratory under the guidance of Dr. Andrey V. Kuznetsov, where he is pursuing his interest in fundamental fluid mechanics and numerical simulations in the context of flows in porous media.

ACKNOWLEDGMENTS

I wish to express my gratitude for the support and guidance of Prof. Andrey Kuznetsov and for providing me with the opportunity to work with the state of the art computational resources available at NC State University.

I wish to acknowledge the contribution of the members of the research group in the Computational Bio-Fluids and Heat Transfer Laboratory - Huang Ching-Wei and Timothy Su, who are also working on simulating turbulence in porous media flows. The critical thinking of the research group, which involved many lively debates, has made this work possible. I also wish to acknowledge Tim's contribution towards providing data for the simulations with surface roughness on the porous media obstacles.

I wish to thank the support staff at NCSU OIT HPC for helping me setup the simulations and for their prompt troubleshooting.

I wish to thank my friends and family for their support.

TABLE OF CONTENTS

LIST OF TABLES

LIST OF FIGURES

1. INTRODUCTION

In fluid mechanics, the phenomenological effects of the agglomeration of microscopic events often contribute to radical macroscale behaviour. The impact of such behaviour is drastically influential to the constructive applicability of the phenomenon in practice for better or for worse. Such a phenomenon, whose occurrence is hardly a rarity in nature, is the vortex shedding resulting from flow separation [1].

Vortex shedding is a simple phenomenon in appearance that draws its roots from a complex, non-linear symmetry breaking instability [2] [3] [4]. The Bernard-von Karman Vortex street cannot occur in its entirety in porous media in practical scenarios since the flow is constrained by solid obstacles. However, the effect of the von Karman instability is significant with repercussions that lead to an asymmetric solution to a symmetrically posed problem. The asymmetric nature of flow is seen to extend to the macroscopic (bulk) behaviour of the flow which is present only if the obstacles are arranged in a specific repetitive manner.

The discovery draws its roots from a quest to study the suppression of turbulent structures in a porous medium with low porosity. The diameter of the solid obstacles d, or the pore size s (obstacle array spacing distance) are used in practice to describe the characteristic length scale of the microscopic flow, neither of which can adequately describe the variation in size of the turbulent structures for the entire range of porosity. Having observed that the turbulent length scale suppression is, in fact, quite significant [5] [6], examination of the associated flow field revealed that the flow deviates significantly from the principal direction in which the driving force (momentum source) is applied. The deviatory flow has been observed by other researchers as well in the context of heat exchangers [7]. The abundance of porous media with low porosity in applications makes it worthwhile to understand the mechanics of this phenomenon [8].

The number of flow systems that can be approximated to be porous is substantial [9] [10]. Modelling macroscopic flow in porous media is, in essence, a lumped parameter method with the added complexity of non-linearity. Although sufficiently accurate macroscopic models are available [10], the sheer versatility of applications invalidates several models. For instance, when simulating turbulence in porous media, the closure models for the fluctuating macroscopic terms still require development [11]. Modelling symmetry breaking in the turbulent flow regime in flows with low porosity requires careful consideration, since the phenomenon is strongly dependent on geometry and boundary conditions. The mechanism by which the microscopic events are transferred to the macroscopic variables, which would result in macroscopic symmetry breaking, is dependent on a range of parameters. Some of these parameters are identified in this work. To understand the interplay between microscopic and macroscopic variables, a comprehensive momentum budget is required in future work.

Turbulent flow in porous media has been studied recently with much rigor. The advent of High Performance Computing has facilitated high resolution studies using numerical simulations, which have enabled resourceful extraction of intricate details that are associated with microscopic scales of turbulent flow. However, the simulations are still subject to reasonable, yet unnatural simplifications. One such simplification that is utilized here is the abstraction of a porous medium as a periodic domain with a uniform arrangement of solid obstacles, called the Generic Porous Matrix (GPM). The GPMs used in this work are two dimensional, deriving from the fact that the voids are distributed in a single plane and extruded in the plane normal direction.

The periodic GPM domain is called a Representative Elementary Volume (REV). The Turbulence REV (REV-T) is defined as the smallest control volume beyond which microscopic

features at the centroid of the control volume cease to have a macroscopic influence. The size of the REV-T is determined based on the expected size of the largest turbulent eddies, which is less than four times the pore size, 4s [6]. The two-dimensional nature of the GPM allows for smaller domain bounds (2s) in the 2-D plane normal direction. Even though the flow features for a 2-D GPM are three dimensional, their influence in the plane normal direction is small. It should be noted that several researchers have successfully utilized smaller domains for turbulence simulations [7] [12].

Significance of Work

Turbulent flow simulations in infinitely spanning homogeneous porous media have revealed a directional deviation of momentum from the principal plane of symmetry. The temporal progression of symmetry breakdown is effectuated through the amplification of a microscopic imbalance that arises from the emergence of a von Karman instability. Several geometric criteria determine the occurrence of symmetry breaking, but the parameters that control it are limited to the momentum supply and the magnitude of confinement. The phenomenon suggests a strong dependence of the macroscopic field variables on the interaction between microscopic vortices. In practice, macroscopic amplification of microscopic instability provides a platform for enhanced fluid mixing in porous media and a source for macroscopic instabilities that are larger in size than the pore scale.

1.1 Modelling Flow in Porous Media

A porous medium is a composite domain, typically defined as a fluid medium with solid obstacles. Since the applications of porous media are diverse, a single "concrete" definition is difficult to state. However, a porous medium should possess the following characteristics [9].

1. A porous medium is multiphase with at least one solid phase and one fluid phase.
2. The solid phase is distributed throughout the domain in a manner that creates voids for the fluid phase which saturate the entire domain.
3. The voids inside the domain have to be interconnected with numerous paths in a manner that allows the fluid to flow through majority of the domain.

The voids that are filled with fluid in a porous medium are called pores and the distributed solid matter is called the porous matrix. The governing geometric parameters of a porous medium are pore size, obstacle diameter, and the sample dimensions (which is not relevant for infinitely porous media). The porosity is defined as the fraction of void volume to domain volume, as written in Equation (1.1) . In this work, the obstacle diameter is defined as the hydraulic diameter of the individual solid obstacles in the porous matrix. The pore size is defined as the distance between the centroids of two adjacent solid obstacles.

$$\varphi = \frac{Void\ Volume}{Domain\ Volume} = \frac{\Omega_F}{\Omega_F + \Omega_S} \tag{1.1}$$

Porous media can be considered homogeneous or heterogeneous depending on the arrangement of the porous matrix. As the name suggests, the solid matter is uniformly distributed in a homogeneous porous medium to form a uniform distribution of pores/voids, resulting in a uniform distribution of porosity. In a heterogeneous porous medium, the arrangement is arbitrary. Most of the naturally occurring porous media are heterogeneous. However, due to the immense complexity and the strong dependence on geometry associated with heterogeneous

porous media, only homogeneous porous media are used in simulations in this work. Homogeneous porous media are more likely to occur in man-made porous media, like packed beds, heat exchangers, filters, etc. It is believed that the underlying physics is similar for both homogeneous and heterogeneous porous media and many researchers make use of the simplicity associated with homogeneity.

Simulating turbulence in a homogeneous porous medium is still a daunting task that requires a lot of computational power. Further simplifications have to be made based on reasonable assumptions. The concept of a Representative Elementary Volume (REV) is used in this work in order to reduce the size of the computational domain. An REV is defined based solely on geometric parameters for laminar flows. Starting from an infinitesimal volume, as the domain volume approaches the size of an REV, fluctuations in the variation of porosity in the domain volume decay to a constant value of porosity. The size of the REV based on this definition is equivalent to one cylindrical obstacle and the void volume that surrounds it. For turbulent flows, the variation of flow parameters should also be considered while deciding the size of the REV. In the work of Jin et al. [5] [6], the size of the largest turbulent structures in a porous medium was found to be of the order of the pore size (s). In more complex cases involving multiple porous length scales, the turbulent structures are seen to decay after a length equivalent to 4 times the pore size. The size of the REV-T for this simulation has been decided to be equal to 4 times the pore scale as shown in Figure 1.1. This REV-T consists of 16 unit cells, each unit cell consisting of a single cylindrical obstacle. For 3-D GPMs, the REV-T size is equal to $4s$ in all directions. For 2-D GPMs, the domain size in the transverse direction is chosen to be only $2s$ to reduce computational effort. This is a reasonable approximation since the flow is expected to have a smaller contribution in this direction, even though the flow is still highly three

dimensional. Periodic Boundary Conditions are applied in all directions to account for flow outside of the REV-T.

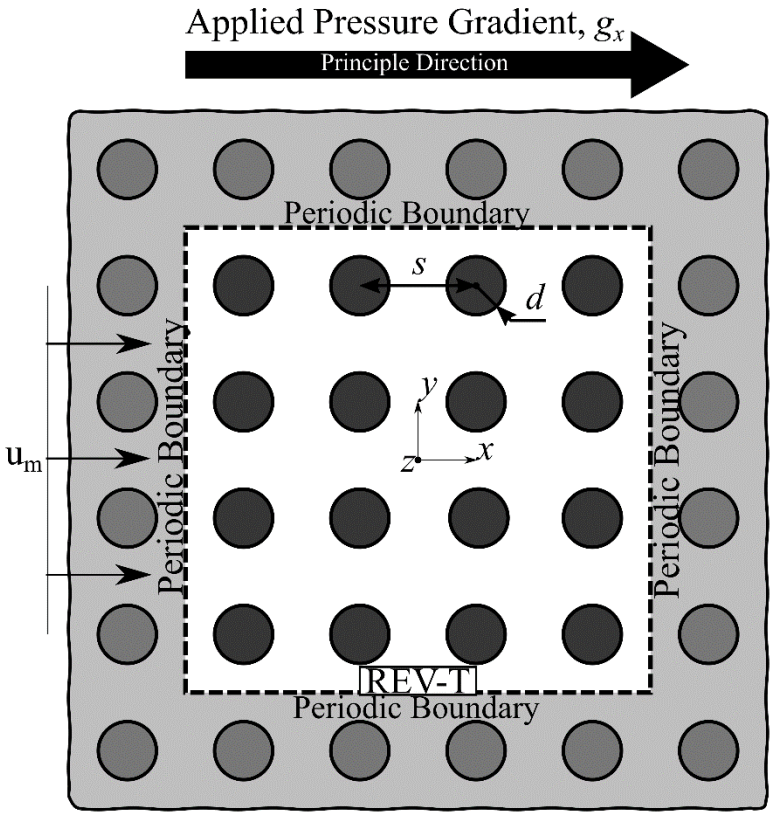

Figure 1.1: Cross-section of a 2-D GPM with the REV-T denoting the computational domain.

At this stage, the concept of macroscopic and microscopic perspectives in porous media flows must be introduced to illustrate the importance of simulations of this nature. While the microscopic perspective provides a highly accurate representation of the flow characteristics, engineers are interested in being able to abstract the microscopic flow behavior into volume averaged macroscopic variables that allow easy implementation for application oriented problems. A microscopic analysis is not possible in engineering problems since the size of the REV might be equivalent to the size of the entire domain. The smallest simulation in this work required 20,000 CPU-Hours on a High Performance Computer while utilizing 30 GB of memory. A simulation of this kind for an engineering problem might not even be viable with the

computational power available with most supercomputing facilities. Macroscopic volume averaging is, therefore, a very powerful tool in simulating porous media flows. The averaging procedure is shown in Equation (1.2). The field variable is decomposed as a sum of average and deviation. Since turbulence is a transient phenomenon, the double decomposition method utilized in this work to calculate macroscopic variables involves both spatial and temporal averaging (for details, see de Lemos [10]).

$$\Phi = \langle\Phi\rangle^i + {}^i\Phi;\ \langle\Phi\rangle^i = \frac{1}{\varphi\Omega_{REV-T}}\int_{\Omega_{REV-T}} \Phi\, d\Omega \tag{1.2}$$

$$Re_p = \frac{u_m d}{\nu};\ u_m = \langle\langle u_1\rangle^i\rangle \tag{1.3}$$

Where $\langle * \rangle^i$ is the spatial averaging operator defined in Equation (1.2), and $\langle * \rangle$ is the Reynolds Averaging operator that is defined in Section 2.2. Flows in porous media are also sensitive to variations in Reynolds number. To sustain turbulence, the pore scale Reynolds number (Re_p) should be high enough to amplify the microscopic disturbances to affect the macroscopic variables. The Reynolds number range of 0.1-10 is known as the Darcy Flow regime, where the drag due to porous obstacles varies linearly with the applied pressure gradient. Flows past the Darcy regime are more complex, where the drag varies in a non-linear manner when the applied pressure gradient is changed. For decades, the Brinkman and Forchheimer extensions to the Darcy equations have been used to simulate flow in the non-linear regime [8]. However, turbulence in porous media introduces an additional closure problem resulting from double decomposition of the macroscopic variables. Microscopic simulations are important to understand the behavior of turbulence in porous media as it helps to close the governing equations. Such simulations by de Lemos [10] have helped derive the model coefficients for the macroscopic turbulence models. DNS simulations by Jin and Kuznetsov [11] have shown that the pore scale suppression of turbulent scales can help derive turbulence models based on pore

scale mixing length. These models have been developed with the help of inferences drawn from the microscopic flow behavior of flow in porous media.

Turbulence is expected to occur in porous media only at Reynolds numbers of one order of magnitude higher than the beginning of the non-linear regime [9]. Experiments have shown that this happens at Reynolds numbers of around 140 [13]. However, this particular value cannot be generalized as a rule for all porous media, since a strong dependence on geometry exists. The Reynolds number is fixed at 10,000 for simulations in this work except while investigating the effect of Reynolds number. This high Reynolds number is chosen to be appropriate for the range of Reynolds numbers seen in 2-D GPMs (heat exchanger flows) while keeping the computational requirements in mind. This value of Reynolds number also satisfies the requirement of full-blown turbulence for the Realizable k-ε turbulence model to be valid [14].

1.2 Characteristics of Turbulent Flow

Since most flows in nature are turbulent, it is important to understand the characteristics that distinguish turbulence from other unsteady flows. In a book written by Tennekes [15], a list of characteristics of turbulence are provided that help in its identification. Some of the relevant characteristics are:

1. Irregular – A turbulent flow field is random in space and time. It can also be said that the lack of randomness is a non-turbulent characteristic. This is useful in the context of statistical analysis of turbulence.
2. Diffusive – Turbulence manifests with additional diffusion in the flow as a product of fluctuations and results in better mixing than laminar flows.
3. Turbulence is inherently three dimensional and time dependent. It occurs at large Reynolds numbers and is rotational.

4. Dissipative – Turbulent flows dissipate energy very well, thereby resulting in a higher mechanical energy loss. Turbulence also feeds off of kinetic energy. The inability to supply kinetic energy to feed the demand of energy loss in dissipation will lead to the decay of turbulence.

The fluctuations in turbulence are amplified by the inertial energy reservoir to form flow structures of scales that are larger than the size of the fluid molecules. These structures, called eddies, have a direction of propagation much different from the principle flow. The eddies vary in size from a smallest size, which is decided based on a balance between viscous and turbulent dissipation, to the largest size, which is determined by the geometry of the fluid domain. A wide range of scales exist in between whose behavior is coupled with its size and energy. It is important to understand the scales of turbulent flow and their contribution to the mean flow.

Scales of Turbulent Flow

In this section, a simple description of the scales of turbulence is provided, that is sufficient to understand the ideas presented in this work. A complete description of the scales is beyond the scope of this document. The scales of turbulence are explained in detail by Pope [16]. The scales of turbulent flow start at the largest eddy scale, which are highly anisotropic in nature. The largest eddy scales are strongly dependent on domain geometry and the boundary conditions. They carry the maximum amount of energy associated with turbulence amongst all the scales of turbulence. A large scale eddy interacts with solid obstacles or other eddies in the flow which cause it to break down into smaller eddies by transferring its energy to them. The individual small eddies possess less energy than the large scale eddy due to the break down operation, which divides the energy between the resultant eddies with some energy lost to the process itself in the form of dissipation.

The break down process continues for the entire range of scales until the smallest scale, known as the Kolmogorov length scale η. At the Kolmogorov scale, the size of the eddy is small enough for the viscous action present in the fluid molecules to dissipate the energy, rather than an inertial break down process. The Kolmogorov length scale is the smallest eddy size in the domain, where the energy is dissipated in the form of viscous heating. However, viscous dissipation starts before the Kolmogorov Length Scale is reached. The process of transferring energy from the largest to the smallest eddies is called the energy cascade. It is expected that the turbulent kinetic energy generation in the largest scales is transferred through the range of scales and ultimately dissipated in the smallest scales.

Based on the energy cascade process, the scales of turbulence are divided into 3 categories – Energy-Containing range, Inertial subrange, and dissipation range. The energy containing range consists of the largest eddies that carry the maximum fraction of the turbulent kinetic energy (TKE). The eddies in this category are expected to be highly anisotropic and show strong dependence on the boundary conditions.

Progressing down the ladder in the energy cascade process, the inertial subrange of eddies are less anisotropic than the Largest eddies. In this subrange, the effects on molecular viscosity are not significant yet, and the eddies are still dominated by breakdown due to turbulent viscosity.

The eddies of scale smaller than the inertial subrange (dissipation subrange) are expected to be universal according to the First and Second Kolmogorov hypothesis. These eddies are easily accounted for using simplistic models that are derived from semi-empirical and statistical methods. In the dissipative range, the effect of molecular viscosity is much more significant than in the inertial range. The turbulence kinetic energy that is generated in the large eddies is

dissipated in this range. The length scales of eddies and the different turbulence energy regimes are represented in Figure 1.2.

With this basic knowledge, the concepts presented in the previous work and in this thesis can be comprehended. Details of specific methods will be provided wherever necessary.

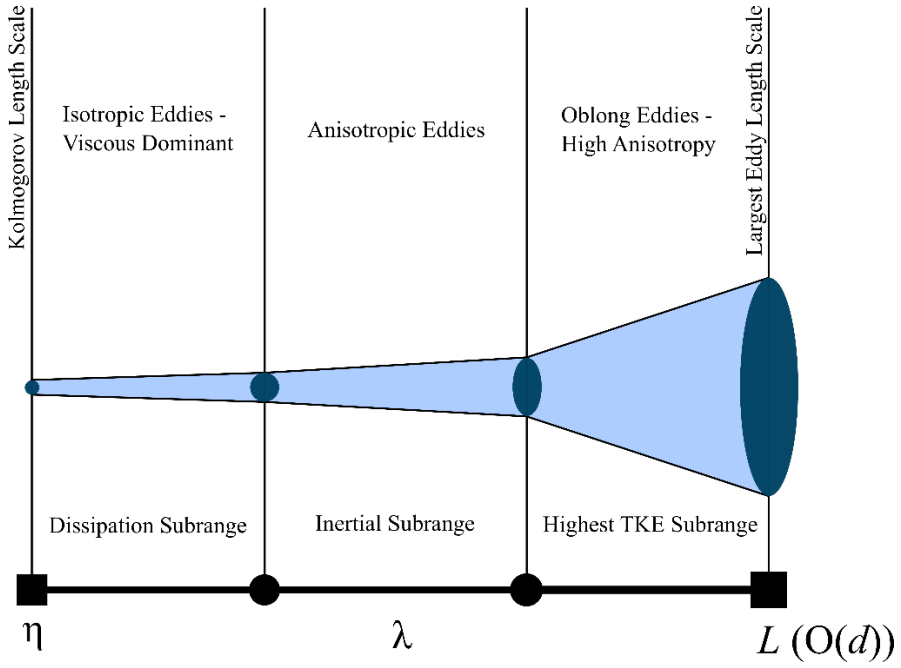

Figure 1.2: Turbulent length scale spectrum segregation based on the concept of the energy cascade.

1.3 Previous Work

Turbulence in porous media has seen renewed interest recently, primarily in the context of translation of turbulence from the micro scale to the macro scale. Simulating flow in porous media at the micro scale for finite domains is a computationally intensive task. To calibrate macroscopic flow models for use with finite domains, knowledge about the flow behaviour is extracted from microscale simulations in infinitely spanning domains. With the help of accurate closure models for the macroscopic governing equations, numerous practical problems with applications in atmospheric flows [17], soil science [18], city planning [12], heat exchangers [7],

and packed bed reactors [19] can be solved in minutes, which originally could take days to analyze credibly using the microscopic approach. The availability of reliable models can also enable engineers to push the limits of porous media, with the capacity to not only predict, but also control flows in porous media.

The flow regime of interest in this work is fully turbulent. Simulations of microscale turbulence with high-resolution methods that resolve the turbulence spectrum, entirely or in part, is not a novel concept. In fact, it can be inferred from current trends in numerical simulations that the volume of research work involving high-resolution CFD has grown at a commensurate rate to that of the development of microprocessors. Some of the efforts involving high-resolution simulations have been invested in understanding the physics behind flows in porous media and the derivation of the merits in using porous media. Microscale simulations are particularly important at this juncture, in a field that is dominated by empirical relations that are far from universal. From the perspective of turbulence modelling in porous media, de Lemos [20] introduced the concept of double decomposition of the macroscopic variables to segregate the variables into spatial and temporal means and fluctuations. The macroscopic equations are closed by modelling the fluctuating terms using data from microscale simulations of porous media using the k-ε RANS method in Pedras and de Lemos [21]. Prior to this work, several researchers have also succeeded in developing macroscopic models for turbulence, all of which involve translating the microscopic k-ε model to the macroscale. Most of these models are presented for reference in books by de Lemos [10], Nield and Bejan [8], Ingham and Pop [22]–[24]. In all of these works, the contribution of the microscopic turbulent structures to the macroscopic flow field is not addressed in detail. Even though a comprehensive study over the entire range of pore scales and shapes is not possible, using basic geometry to parametrize flow behaviour can

improve the understanding of flows in porous media. A well-known problem with using porous media models is that the model constants change drastically with the pore geometry. For example, to estimate permeability of a porous medium, the modelling relations differ with shape and arrangement. For those geometries that involve randomly arranged porous media with irregular void shapes, engineers have to resort to performing experiments to obtain the necessary input parameters. This would pose a serious issue if the porous medium is one that cannot be experimented with (for example, cities and vegetation). The underlying physics behind microscopic vortex shedding and the dynamics of vortices within the porous medium is believed to hold the key to understanding the vast range of behaviour that is sensitive to the obstacle geometry. However, a majority of works have not analyzed the flow dependence on vortex shedding in porous media. Some researchers have analyzed the influence of large scale turbulent structures on the macroscopic flow field.

The Direct Numerical Simulations performed by Uth et al. [5] form the basis of the work presented in this thesis. The researchers set out to analyze the maximum length scale of turbulence within the pores, in order to assess whether macroscopic turbulence models would need to address the issue of turbulent length scales that are larger in size than the pore scale. By using progressively smaller REVs for computations, the size of the largest turbulent eddies are calculated using statistical techniques and flow visualization. The size of the largest eddies were consistently below the pore scale of the geometry. The paper also discusses whether it is important to resolve the entire spectrum of eddies including the Kolmogorov Scales while performing simulations that are concerned with large scale eddies. Data from Low-Resolution DNS is compared with High-Resolution DNS performed with the Finite Volume Method and the more accurate Lattice Boltzmann Method.

In an article by Jin et al. [6], the authors use DNS to simulate turbulent flow in porous media with 2-D and 3-D solid obstacles. Both circular and square geometries are used to assess whether the shape of the obstacles has an impact on the size of the largest turbulent structures. For circular and square cylindrical and spherical obstacles, the turbulent length scales were limited by the size of the pore. Introducing an obstacle with a length scale that is larger than the size of the pore generates turbulent structures that are larger in size than the pore scale. However, the large scale turbulent structures vanish as they disintegrate under the influence of the porous solid obstacles.

Most of the researchers who have worked with generic porous media geometries assume high porosity, since turbulent structures are expected to diminish in size when porosity is lowered. The applications of porous media with low porosity in engineering is also questionable, since they require a larger pressure gradient to drive flow through them. However, porous media with low porosity are a frequent occurrence in nature. To simulate these flows, researchers often use an obscure obstacle geometry arranged randomly in space, derived from imagery of rock and soil samples. Using randomly formed geometry does not allow for a comprehensive study of the turbulent structures as it would be difficult to comment on whether certain phenomena are contributed by the geometry or by the flow features. The use of random geometry would also substantially increase the computation cost needed to resolve all the features.

Prior to the work presented in this thesis, a study was performed by Huang et al. [25] to study the effect of pore size on the turbulent structures in porous media with low porosity and the results were contrasted with flow behaviour in highly porous media. The premise of this work is that the strong suppression of turbulence in porous media must have an impact on the macroscale flow behaviour. Turbulence in porous media is bound by unconstrained behaviour at $\varphi = 1$ and

stationary flow at $\varphi = 0$. A range of flow behaviour is observed by the authors as the porosity is progressively lowered. When the value of porosity is high, the fluid passes through with little interference. The largest turbulent structures are still limited to the pore size, however. The wake behind the solid obstacles have a negligible interaction with the adjacent obstacles, with each obstacle behaving independently of the other.

As the porosity is reduced, the wake interaction among streamwise adjacent obstacles starts to become significant. This causes an increase in turbulence intensity on the flow incident surface of the obstacle where the vortices impinge on the wall of the obstacle. Turbulence generation is more significant in the presence of shear. The flow pattern is observed to be symmetric from $\varphi = 0.992$ until $\varphi = 0.8$. In this range of porosity, the size of the vortices scale with the radius of the solid obstacle. A change in the flow behaviour starts to occur when the porosity is lowered below 0.8. For the cylindrical obstacle geometry that is used in this work, this value of porosity corresponds to the pore size being equivalent to the obstacle diameter. Since the vortex size scales with the radius of the obstacle, the vortex can still be formed in the void space, but the vortex is too close to the wall for dissipation. This results in a high value of turbulence intensity that is distributed throughout the medium. This is an indicator of the effect of shear dominating the entire flow domain causing the flow to possess characteristics of "internal" flows.

When the porosity is reduced further, symmetry in the solution field is lost. From $\varphi = 0.72$ onwards, the flow is seen to deviate from the direction of applied pressure without external aid. The deviation in flow angle can be seen to increase as the porosity is reduced until $\varphi = 0.5$ (see Figure 1.3). This is a particularly important result that has led to the investigations that form this thesis. Within each unit cell in the porous medium, asymmetry exists in the vortex size and

shape, and the locations of the stagnation and separation points. A steady state RANS solver is used by the authors, which did not allow for a systematic investigation of the underlying cause of the deviation. The next logical step in this investigation is to use a transient scale resolving scheme to capture the vortex dynamics to analyse the progression of symmetry-breaking by starting from a uniform flow field.

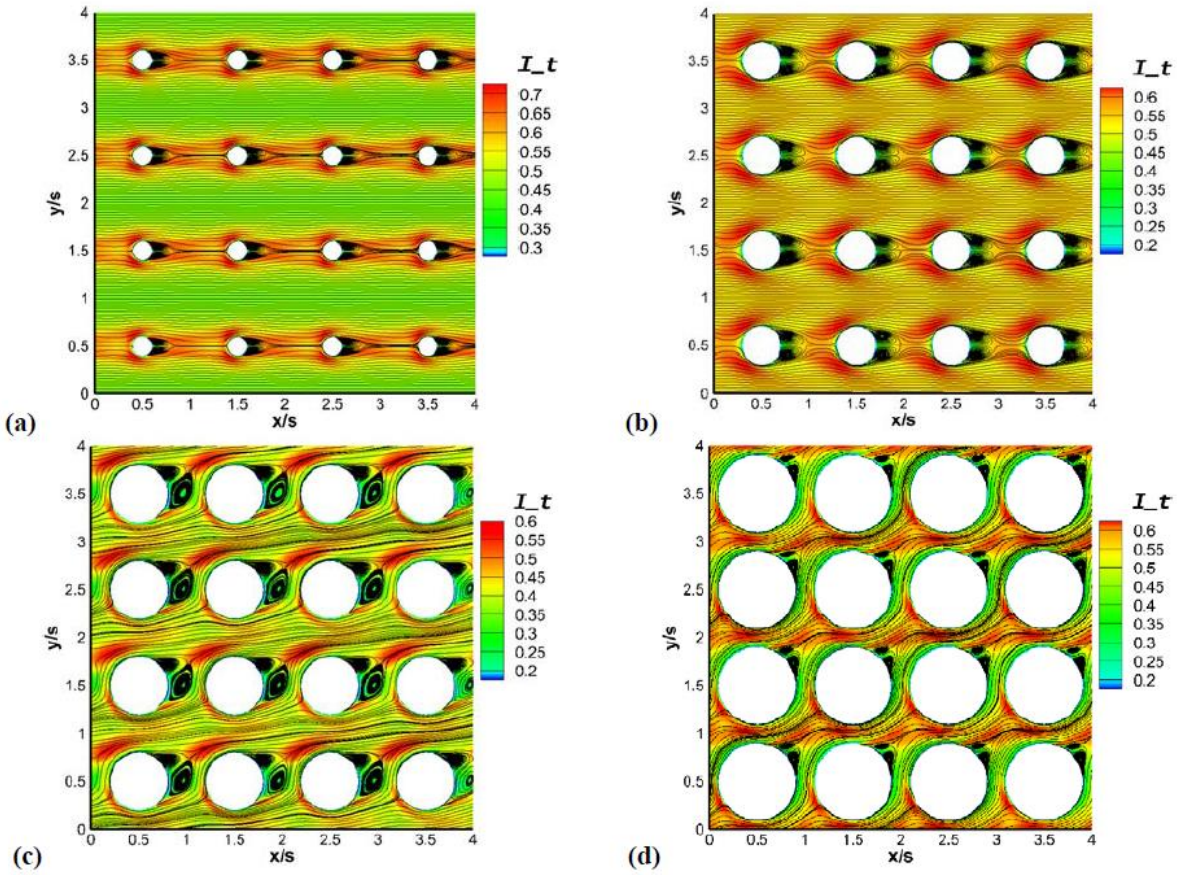

Figure 1.3: 2-D mean flow streamlines plot over contours of turbulence intensity show the different flow behaviour that is present when the porosity is changed [25].

2. TURBULENCE MODELLING AND NUMERICAL CONSIDERATIONS

2.1 Governing Equations of Flow

To investigate the fluid behavior in a microscale perspective, the technique of numerical simulation using Computational Fluid Dynamics is used in the present work. While working with numerical methods, the first step is to identify the governing equations of the flow, and also the variables and parameters of relevance that should be measured to conclusively build a case.

Since the flow is simulated in a microscale porous matrix, it is important to verify whether the principles of continuity are valid for the cases that are simulated in the present work. A non-dimensional number, called the Knudsen number (Kn), is used to verify the applicability of continuity. Knudsen number is defined as the ratio of mean free path of the fluid molecules to the characteristic length scale of the flow. A sufficiently small Knudsen number ($Kn<<1$) indicates that the degree of rarefaction of the flow is less, and that the principles of continuity can be applied with confidence. The Knudsen number, estimated using mean molecular spacing, in this work is of the order of 10^{-7}, which is well within the limits of the approximation of continuity.

The compressibility of the flow is evaluated using the Mach number. The Mach number is calculated to be less than 0.01, and therefore, the flow is approximated to be incompressible. The governing equations of flow used in this work, namely the Navier-Stokes equations of fluid flow, obey the principles of continuity and incompressibility. According to the principles of continuity, the properties of the fluid remain the same between the bulk and an infinitesimal control volume. Derived by conserving momentum in an infinitesimal control volume using Newton's Second Law of Motion, the Navier-Stokes equations are a set of three conservation equations for momentum defined in each Cartesian direction, which when coupled with the Mass Conservation equation yields a sufficiently accurate physical model of the flow. The Energy equation is

omitted in the present work, since the flow is incompressible and the focus is on fluid kinematics. The governing equations are written in (Equations (2.1), (2.2)) using the Einstein Summation Convention.

$$\frac{\partial u_j}{\partial x_j} = 0 \qquad (2.1)$$

$$\frac{\partial u_i}{\partial t} + \frac{\partial u_j u_i}{\partial x_j} = -\frac{1}{\rho}\frac{\partial P}{\partial x_i} + \nu \frac{\partial^2 u_i}{\partial {x_j}^2} + g_i \qquad (2.2)$$

A constant flow rate is prescribed by altering the momentum source parameter, g_i, at each iteration. For incompressible flows, the equation of state cannot be used to solve for Pressure. To evaluate the pressure, the Pressure Poisson equation is used, which is solved alongside the Navier-Stokes and continuity equations for completeness.

To simulate turbulent flow using the Navier-Stokes equations, the method of Direct Numerical Simulation is known to be one of the more accurate methods, where the Navier-Stokes equations are solved using an adequately refined mesh to capture the flow features in its entirety, with the smallest cells sufficient to capture the Kolmogorov length scale motions. The size of the computational grid required to resolve the smallest scales of turbulence scales with Reynolds number as $N \sim (Re)^{9/4}$. To perform simulations on such a colossal grid is an expensive task that requires immense computational power that is not available at this juncture. The inability to resolve the flow completely calls for the use of turbulence models that have to be implemented to compensate for the loss of resolution. The requirements of a turbulence model are as follows: “An ideal model should introduce the minimum amount of complexity while capturing the essence of the relevant physics” [14]. The relevant physics in this work is the vortex shedding behind elements of the porous matrix and the characteristics of the larger eddies, and the qualitative impact that they have on the bulk flow behavior.

2.2 Theory of RANS models

Reynolds Averages Navier-Stokes (RANS) turbulence models are a statistical approach to modelling the random turbulent flows in terms of the mean temporal behavior of the flow. To this end, the field variables are decomposed into a mean and a fluctuating component through the method of Reynolds Averaging. This decomposition process is called the Reynolds Decomposition. The field variable Φ is written as the sum of a mean value $\langle\Phi\rangle$ and a fluctuation Φ'. This is illustrated in Figure 2.1 with the help of a random signal in time imposed on a sine wave.

$$\langle\Phi(x_i,t)\rangle = \lim_{T\to\infty}\frac{1}{T}\int_t^{t+T}\Phi(x_i,t)dt \qquad (2.3)$$

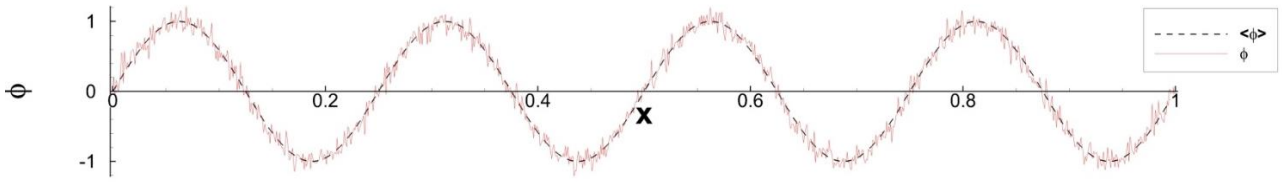

Figure 2.1: Random Signal (instantaneous) imposed on a sinusoidal wave (Reynolds averaged).

When this decomposition is incorporated in the Navier-Stokes equations (Equations (2.1), (2.2)), after arithmetic manipulation, the RANS equations can be written in the following form.

$$\frac{\partial\langle u_j\rangle}{\partial x_j} = 0 \qquad (2.4)$$

$$\frac{\partial\langle u_i\rangle}{\partial t} + \frac{\partial\langle u_j\rangle\langle u_i\rangle + \langle u'_i u'_j\rangle}{\partial x_j} = -\frac{1}{\rho}\frac{\partial\langle P\rangle}{\partial x_i} + \nu\frac{\partial^2\langle u_i\rangle}{\partial {x_j}^2} + \langle g_i\rangle \qquad (2.5)$$

The presence of an additional term, $\rho\langle u_i u_j\rangle$ (called the Reynolds Stress Term), which makes the RANS system of equations underdetermined. This "closure" problem can be tackled by writing additional transport equations for Reynolds Stress and solving them along with the RANS equations. The Reynolds Stress Model is well known for its accuracy, its ability to capture anisotropic effects and other complex interactions between the Reynolds Stresses.

However, this model is computationally expensive and requires special care to achieve convergence.

An alternate method to close the RANS system of equations is to represent the Reynolds Stress term as a relation to the mean field variables. The Boussinesq Hypothesis (eddy viscosity approximation) facilitates the use of the mean field variables to describe the Reynolds Stress. Boussinesq postulated that the mechanism of momentum transfer amongst eddies is similar to the mechanism of momentum transfer amongst the fluid molecules. The description of the associated stresses should be analogous, thereby introducing the parameter called eddy viscosity. Reynolds Stress is calculated as the product of eddy viscosity and strain rate in all of the eddy viscosity models. The eddy viscosity assumption removes the fluctuation terms from the RANS equations. However, it introduces a new unknown term in the equations, namely the eddy viscosity, which is a scalar quantity. Analogous to molecular viscosity, where the viscosity is proportional to molecular velocity and the length of the mean free path, the eddy viscosity is assumed to be proportional to the characteristic length scale and the characteristic velocity.

For the present work, the two equation Realizable k-ε model is used, where the velocity and length scale descriptions are derived from the Turbulent Kinetic Energy (k) and the Turbulent Dissipation Rate (ε) as shown in Equation (2.6). The Turbulent Kinetic Energy and Turbulent Dissipation rate are defined in Equation (2.7).

$$\nu_T \sim l_c v_c \; ; \; l_c = \frac{k^{1.5}}{\varepsilon}, v_c = k^{0.5} \tag{2.6}$$

$$k = 0.5\langle u'_i u'_i \rangle \; ; \; \varepsilon = \; \nu \langle \frac{\partial u'_i}{\partial x_j} \frac{\partial u'_i}{\partial x_j} \rangle \tag{2.7}$$

The transport equations for k and ε are derived by manipulating the Navier-Stokes Equation to fit the definitions provided in Equation (2.7). The exact equations thus obtained are quite complex and contain several undefined terms which are then modelled analytically and

closed using empirical data. The Realizable k-ε model is a semi-empirical model that has been implemented successfully for a wide range of flows with improved accuracy over the Standard k-ε model. The improvements in accuracy are attributed to the new formulation for ε and for $C_{\mu,}$ which is the proportionality constant in the eddy viscosity expression. The model is titled Realizable since it satisfies certain mathematical constraints on the Reynolds Stresses that make it physically realizable. The use of a constant C_{μ} results in unrealistic predictions of normal stress which is rectified in the Realizable model using a model constant that is dependent on the field variables. Further details regarding the model are available in the published work of Shih et al. [26]. The transport equations used in the model are summarized in Equations (2.8) – (2.13) (taken from ANSYS documentation [27] [28]). Note that C_{μ} is determined based on rate of rotation and strain in the flow. It has been observed that this formulation works admirably in flows involving rotation and boundary layers in adverse pressure gradients, separation, and recirculation. These flow features are expected to appear in simulations with the microscopic perspective in porous media.

$$\frac{\partial k}{\partial t}+\frac{\partial (ku_j)}{\partial x_j}=\frac{\partial}{\partial x_j}\left[\left(\nu+\frac{\nu_T}{\sigma_k}\right)\frac{\partial k}{\partial x_j}\right]+2\nu_T\langle S_{ij}\rangle\langle S_{ij}\rangle-\varepsilon \quad (2.8)$$

$$\frac{\partial \varepsilon}{\partial t}+\frac{\partial (\varepsilon u_j)}{\partial x_j}=\frac{\partial}{\partial x_j}\left[\left(\nu+\frac{\nu_T}{\sigma_\varepsilon}\right)\frac{\partial \varepsilon}{\partial x_j}\right]+C_1\sqrt{2\langle S_{ij}\rangle\langle S_{ij}\rangle}\varepsilon-C_2\frac{\varepsilon^2}{k+\sqrt{\nu\varepsilon}} \quad (2.9)$$

$$C_1=\max\left(0.43,\frac{\eta}{\eta+5}\right);\ \eta=\sqrt{2\langle S_{ij}\rangle\langle S_{ij}\rangle}\frac{k}{\varepsilon};\ C_2=1.9;\ \sigma_k=1.0;\ \sigma_\varepsilon=1.2 \quad (2.10)$$

$$\nu_T=C_\mu\frac{k^2}{\varepsilon};\ C_\mu=\frac{1}{A_o+A_s\frac{kU^*}{\varepsilon}};\ U^*=\sqrt{S_{ij}S_{ij}-\Omega_{ij}\Omega_{ij}} \quad (2.11)$$

$$A_o=4.04;\ A_s=6\cos\phi;\ \phi=\frac{1}{3}\cos^{-1}\sqrt{6W};\ W=\frac{S_{ij}S_{jk}S_{ki}}{(S_{ij}S_{ij})^{1.5}} \quad (2.12)$$

$$S_{ij}=0.5\left(\frac{\partial\langle u_j\rangle}{\partial x_i}+\frac{\partial\langle u_i\rangle}{\partial x_j}\right);\ \Omega_{ij}=0.5\left(\frac{\partial\langle u_j\rangle}{\partial x_i}-\frac{\partial\langle u_i\rangle}{\partial x_j}\right) \quad (2.13)$$

The use of the k-ε class of models introduces a complication that the value of ε is non-zero and unknown on the surface of walls. Implementing a wall boundary condition would require modifications to the original model equations, wherein the value of ε is calculated algebraically based on the independent variables and empirical data. A wall model is employed, called the Enhanced Wall Treatment in ANSYS Fluent, which is a blend of the Two Layer wall model and the Law of the Wall model. The Two Layer model is used in locations of adequate mesh resolution where the non-dimensional first cell layer distance is 5 or less. The Two Layer model uses a one equation turbulence model in the vicinity of the wall where the influence of molecular viscosity is expected to be significant, while the set of equations (2.8) – (2.13) are used in the fully turbulent regions. The two models are coupled at the interface to ensure continuous behavior. The Law of the Wall approximation is used in other locations, which approximates the boundary layer using a logarithmic profile in the wall-normal direction. A blending function is used to combine the laminar and fully turbulent wall laws in the buffer zone to obtain a single Law of the Wall that can be applied at any location in the boundary layer. The value of ε in the wall adjacent cells are computed, in the Law of the Wall model, by assuming that the production

of k in the wall adjacent cells is equivalent to its dissipation. Therefore, ε is estimated from the value of production of k, which in turn is calculated based on the strain rate extracted from the Law of the Wall. Details of the implementation of Enhanced Wall Treatment are available in the ANSYS Documentation [27] [28]. The ε formulation for the viscosity affected near wall region in the Two Layer model is provided below. The transport equation for k in both layers is similar to Equation (2.8).

$$\varepsilon = \frac{k^{1.5}}{l_\varepsilon} \tag{2.14}$$

$$\nu_{T_{2-Layer}} = C_\mu l_\mu \sqrt{k} \tag{2.15}$$

$$l_\varepsilon = yC_l^*\left(1 - e^{\frac{-Re_y}{A_e}}\right);\ l_\mu = yC_l^*\left(1 - e^{\frac{-Re_y}{A_\mu}}\right) \tag{2.16}$$

$$A_\mu = 70, A_e = 2C_l^*, C_l^* = \kappa C_\mu^{-0.75},\ Re_y = \frac{y\sqrt{k}}{\nu} \tag{2.17}$$

The justification behind using the Realizable k-ε model is quite rudimentary. Since the parameter of interest is the macroscopic/bulk contribution, the macroscopic flow velocity angle that is obtained from LES is compared with a variety of RANS models and the model with the closest resemblance is chosen for future simulations. The results are summarized in Table 2.1.

Table 2.1: Macroscopic Flow angle prediction with different RANS models compared with LES.

Model	**Macroscopic angle predicted**
LES TKE	33.7
Realizable K-ε	33.6
Standard K-ε	34.0
Standard K-ω	38.4
SST K-ω	38.5

2.3 Theory of Large Eddy Simulation

Large Eddy Simulation (LES) is a recent development in turbulent flow computations. The simulation procedure involves the resolution of the energy-carrying eddies in the flow, while the smaller eddies are modelled. The rationalization behind this procedure is that the larger eddies carry a substantial portion of the Reynolds Stresses and that these eddies are directly influenced by the boundary conditions. The smaller eddies on the other hand are expected to be weaker in their bulk contribution towards the Reynolds Stress, and their behavior is approximated to exhibit universality amongst different types of flows.

LES has been tested successfully for many problems of industrial and academic interest. Among the isotropic SubGrid Scale (SGS) models, the Dynamic class of models have been shown to perform well in modelling the SubGrid Scale effects, except in the near wall regions [29]. The Dynamic class of models have been shown to have superior performance in transitional flows and in fully turbulent flows. The Dynamic Smagorinsky and Dynamic One Equation Turbulent Kinetic Energy models have both been shown to reliably predict the natural transition of boundary layers [30]. This is particularly useful since the simulations in this work are performed for a wide range of Reynolds numbers.

The Dynamic class of models have also been shown to have superior performance for flows past bluff bodies which usually involves the same flow dynamics as the present case. A paper by Breuer [31] successfully tests the application of LES in flow past a circular cylinder showing good agreement with experimental data. Rodi [29] provided an insightful comparison of the RANS and LES models in simulating bluff body flows highlighting the superior performance of LES. He concluded that three dimensional effects associated with the flow are captured well by the Dynamic LES models. However, the RANS models are sufficient to obtain an overall

picture. At higher Reynolds numbers, the contribution of the SGS model is much more significant. The lack of grid resolution introduces a requirement for the SGS model to account for a large fraction of unresolved structures. This is the rationale behind solving an additional transport equation for SubGrid turbulent kinetic energy in this work. Krajnovic and Davidson [32] assessed the effectiveness of the Dynamic One-Equation model in predicting several parameters associated with vortex shedding (separation, reattachment, shedding frequency) in the absence of adequate mesh resolution. The model worked well in replicating the experimental results despite the absence of the near wall turbulence streaks in the resolved flow field. The Dynamic One-Equation model, however, is not the most sophisticated SGS models. Abba et al. [33] brought out the shortcomings of this model by comparing it with anisotropic and mixed SGS models. Future work must address these shortcomings, which are localized in the near wall region.

Several researchers have also applied LES models with confidence for flows in homogeneous porous media. Kuwahara et al. [12] used the Smagorinsky model to simulate flow in a staggered porous matrix with excellent agreement with Ergun's equation. Iacovides et al. [7] found that the Dynamic Smagorinsky model agreed well with experimental results for High Reynolds number flow in tube bank heat exchangers. The use of a One Equation model will improve on that in the near wall regions. Werner and Wengle [34] presented an application of LES for a channel flow with a single obstacle, the flow features of which are quite similar to an array of obstacles that is present in porous media. The Smagorinsky model was used to simulate this flow at a high value of Reynolds number of 50,000, with satisfactory results. The Reynolds number of simulations in this work assume a maximum value of only 10,000.

Existing literature suggests that the use of an algebraic SGS model (Dynamic Smagorinsky) is sufficient to capture the primary features of the flow. However, the use of a One-Equation model is necessary in the case of inadequate mesh resolution. The mesh resolution in this work is designed to be globally adequate, and the One-Equation model is used to account for local inadequacies. The contribution of anisotropic effects in the subgrid scale is not captured, since the solver package ANSYS Fluent 16.0 does not include an anisotropic subgrid scale model.

2.3.1 The Dynamic One-Equation SGS Model

The Navier-Stokes equations are a set of continuously defined equations in space. They are designed to capture the spectrum of motions in its entirety. From a mathematical standpoint, the Naveir-Stokes equations need to be operated on to filter out the contribution of the smaller eddies in LES. However, it will be shown later (in Equation (2.20)) that this filtering operation is implicit in the Finite Volume Methods that have been used in this work. The filtering operation is performed with the help of a low-pass filter, which as the name suggests filters out the higher frequency motions. In this work, note that the filtering operation is performed in space only.

$$\bar{\Phi}(x) = \iiint G(x,x')\Phi(x')dx' \qquad (2.18)$$

$$G(x,x') = \begin{cases} \frac{1}{\Delta}, x' \in V \\ 0, Otherwise \end{cases} \qquad (2.19)$$

A generic filtering operation is provided in Equation (2.18), where the variable $\Phi(x)$ is filtered in the fluid domain by the Filter Kernel, G(x,x'). The effect of the filtering operation is shown in Figure 2.3. In Equation (2.19), the Box Filter Kernel is described in terms of the Filter Width, Δ. Other types of filters that are also popular are the Gaussian Filter and the Spectral Cut-Off Filter. For the finite volume implementation of LES, the filtering process is implicit in the formulation. Since the equations are discretized in physical space, the implicit filter kernel is

similar to the box filtering operation. The implicit filtering process can be elucidated with the help of the 1-D Central Differencing Approximation.

$$\frac{u(x+\Delta x)-u(x-\Delta x)}{2\Delta x} = \frac{d}{dx}\left(\frac{1}{2\Delta x}\int_{x-\Delta x}^{x+\Delta x} u(x')dx'\right) \qquad (2.20)$$

The central difference approximation cuts off smaller contributions that are present in the higher order derivatives in the Taylor Series expansion, which is similar to how the box filter functions. It is interesting to note, however, that this box filter does not filter out all the high frequency eddies. When represented in the spectral space, the box filter does not cut off at the filter width. Rather, it behaves in a manner as depicted in Figure 2.2. The Box Filter is not effective in attenuating the high frequency contributions. This problem is not circumvented in calculations in this work.

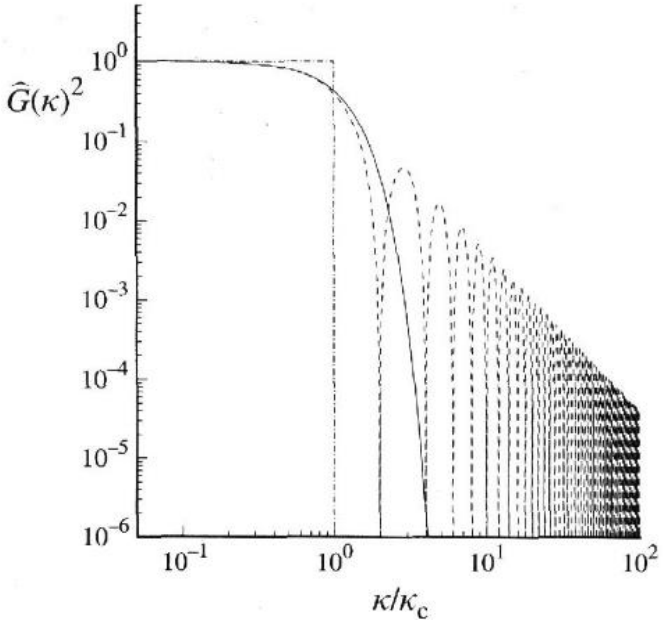

Figure 2.2: Attenuation Factors for (i) Box Filter (Dashed line) (ii) Gaussian Filter (Solid Line) (iii) Spectral Cut-Off Filter (dot-dashed line) [16].

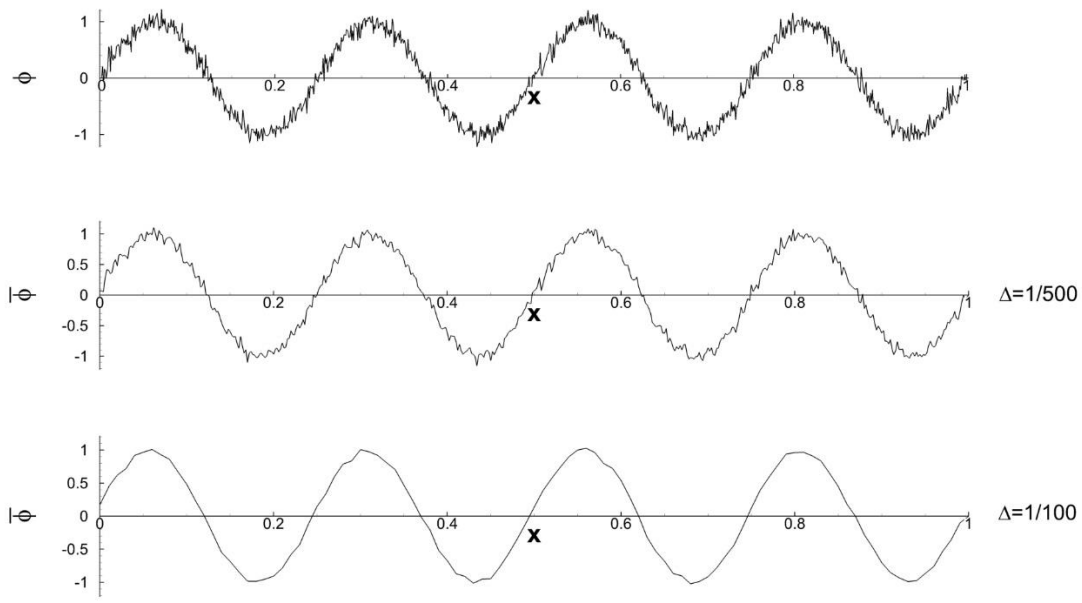

Figure 2.3: Spatial Box Filtering operation on a random field imposed on a sinusoidal wave.

$$\frac{\partial \overline{u_j}}{\partial x_j} = 0 \tag{2.21}$$

$$\frac{\partial \overline{u_i}}{\partial t} + \frac{\partial \overline{u_j u_i}}{\partial x_j} = -\frac{1}{\rho}\frac{\partial \bar{P}}{\partial x_i} + \nu \frac{\partial^2 \overline{u_i}}{\partial {x_j}^2} + g_i \tag{2.22}$$

The filtering operation is performed for the Navier-Stokes equations to yield the Filtered Navier-Stokes equations. The convection term in the momentum equation is expanded using the Leonard Decomposition method which splits the field variable, Φ, into the filtered/resolved component $\overline{\Phi}$, and the subgrid/residual component $\widetilde{\Phi}$ (Note that this notation is not conventional, it is used to avoid confusion with Reynolds Decomposition). This decomposition yields three undetermined terms, called Leonard Stress, Cross-Term Stress, and SGS Reynolds Stress.

$$\overline{u_i u_j} = \overline{u}_i \overline{u}_j + \underbrace{\left(\overline{\overline{u}_i \overline{u}_j} - \overline{u}_i \overline{u}_j\right)}_{Leonard} + \underbrace{\left(\overline{\overline{u}_i \widetilde{u}_j} + \overline{\overline{u}_j \widetilde{u}_i}\right)}_{Cross-Term} + \underbrace{\left(\overline{\widetilde{u}_i \widetilde{u}_j}\right)}_{SGS\ Reynolds} \tag{2.23}$$

Leonard Stresses are of the order of the truncation error in a second order accurate differencing scheme. It is, therefore, implicitly represented in calculations [14]. Separate modelling is not necessary. The Cross-Term and SGS Reynolds Stresses are modelled together

by the use of a SGS model. The eddy viscosity class of models are used in this work which is represented as per the Boussinesq Hypothesis presented in Section 2.2. According to this, the sum of Cross-Term Stress and the SGS Reynolds Stress is written in terms of the strain rate and a SGS eddy viscosity (Equation (2.24)). The rationale behind using the eddy viscosity hypothesis for the SGS stresses is that the SGS eddies are small enough to behave in a manner similar to molecules. The larger eddies, whose behavior is expected to deviate from molecular dynamics, are directly captured.

$$\tau_{SGS,ij} = \nu_{SGS}\left(\frac{\partial \overline{u_i}}{\partial x_j} + \frac{\partial \overline{u_j}}{\partial x_i}\right) + \frac{2}{3}k_{SGS}\delta_{ij} \quad (2.24)$$

$$\nu_{SGS} = C_k \Delta \sqrt{k_{SGS}} \quad (2.25)$$

$$k_{SGS} = \frac{1}{2}(\overline{u_i}^2 - \overline{u_i}^2) \quad (2.26)$$

The SGS eddy viscosity is represented as a product of the characteristic length scale and the characteristic velocity scale for the SGS motions. Unlike RANS, the length scale of the modelled eddies is known a priori to be equivalent to the Cut-Off filter width, Δ_{SGS}, which is calculated as the cube root of the volume of the computational cell. The filter width is represented inaccurately in high aspect ratio cells, which is reflected in the quality of the solution at those cells (details in Section 3). The Dynamic One Equation SubGrid Kinetic Energy model is used in this work, which solves an additional scalar transport equation for the SubGrid Kinetic Energy (k_{SGS}). The SGS eddy viscosity for this model is calculated as Equation (2.25) and The SubGrid Kinetic Energy is defined as in Equation (2.26). The transport equation for subgrid

kinetic energy is provided in Equation (2.27).The details of this model are provided in Kim & Menon [35].

$$\frac{\partial k_{SGS}}{\partial t} + \frac{\partial(\overline{u}_j k_{SGS})}{\partial x_j} = -\tau_{SGS,ij}\frac{\partial \overline{u}_i}{\partial x_j} - C_\epsilon \frac{k_{SGS}^{1.5}}{\Delta} + \frac{\partial}{\partial x_j}(\nu_{SGS}\frac{\partial k_{SGS}}{\partial x_j}) \qquad (2.27)$$

The model constants, C_k and $C_{\epsilon,}$ are left to be determined. The constants can either be determined empirically or determined from the resolved field variables, like in the RANS model. The methodology of determining the model constants in LES is, however, different from the RANS model. The methodology is called the Dynamic Procedure, first proposed by Germano et al. [36]. To calculate the model constants "dynamically", a secondary filter is used, called the test filter, where the filtered field variables are filtered once again. The model coefficient is then evaluated from the SubGrid contribution calculated by using the test filter. This methodology was first implemented and tested successfully for the Smagorinsky SGS model, which is an algebraic model. A requisite for the dynamic procedure is that the gap between the cut-off filter and the test filter is small enough for the SubGrid turbulence to be similar for both filters.

The dynamic procedure used in the one-equation model is different from the Germano model. The Localized Dynamic Kinetic Energy model is used in this work, which is also a model based on scale-similarity. Experimental results have suggested the existence of similarity between the SGS stresses and the Leonard Stresses (this relation is called the Germano Identity). Exploiting this feature, the Localized Dynamic model is drafted on this premise that the SGS stress in the main filter (Δ_{SGS}) will be proportional to the Leonard stress in the test filter ($\hat{\Delta}$). The model constant, C_k, is left to be determined, which is calculated based on a least-squares approximation of the above relation. The process in described in Equations (2.28)-(2.30). The

model constant, C_ϵ, is determined in a similar way. The test filter width is set to be equal to twice the main filter size in this work.

$$L_{ij} = -2C_k\sqrt{k_{test}}\widehat{\Delta}\widehat{\overline{S_{ij}}} + \frac{1}{3}L_{kk}\delta_{ij} \quad (2.28)$$

$$L_{ij} = \widehat{\overline{u_i}\overline{u_j}} - \widehat{\overline{u}_i}\widehat{\overline{u}_j};\ k_{test} = 0.5(\widehat{\overline{u_k}\,\overline{u_k}} - \widehat{\overline{u_k}}\,\widehat{\overline{u_k}}) \quad (2.29)$$

$$C_k = 0.5\frac{L_{ij}M_{ij}}{M_{ij}M_{ij}};\ M_{ij} = -\widehat{\Delta}\sqrt{k_{test}}\,\widehat{\overline{S_{ij}}} \quad (2.30)$$

3. NUMERICAL SOLUTION STRATEGY IN ANSYS FLUENT

The aim of this section is to provide insight into the necessary steps needed to perform numerical simulations for incompressible turbulent flow in ANSYS Fluent using the numerical algorithms and discretization techniques that are available in ANSYS Fluent Release 16.0. This section will serve as a primer for future researchers looking to continue this work using Commercial Finite Volume Solvers. The section will start with a brief introduction to ANSYS Fluent and continue to describe the steps using from pre- to post- processing in this work.

The version of ANSYS Fluent used in this work is ANSYS Fluent Release 16.0 in a HPC framework. ANSYS Inc. is a company devoted to developing engineering simulation software that address multi-disciplinary requirements with a holistic integrated environment which has internetworked capabilities from the development to delivery stage. ANSYS Fluent is the Computational Fluid Dynamics (CFD) solver that is written in the C language. ANSYS Fluent is designed to be robust and versatile, by offering a well-validated, numerically stable Finite Volume solver. These features of ANSYS Fluent make it attractive in the industry. However, for simulations of large scale flows with relative simplicity to industrial problems, such as the ones seen in this work, it should be noted that the methods used in this solver are detrimental to computational performance. Although ANSYS Fluent has excellent parallelisation capabilities (can scaled over 172,000 cores [37]), the resources available for this work cannot exceed 256 cores. There is a trade-off in using commercial CFD solvers for large-scale numerically simple problems, since they are designed to handle more complex scenarios. The use of the Algebraic MultiGrid (AMG) solver (in place of the recommended direct numerical solver), the use of Unstructured grids (instead of block-structured grids), and severely under-relaxed schemes, slow down the speed of simulation. However, valuable time is saved in code development and

validation that would amount to a much larger timeline, which outweighs the merits of using a tailor-made in-house code. This is one of the primary reasons why commercial CFD code is increasingly being used in academic research today with a result-oriented mind-set that allows the user to focus on the fruits of the simulation. The speed of simulations in the current work are accelerated by proper implementation on the HPC framework by taking advantage of faster networking interconnect and restricting the span of the simulation to a single system with shared memory. It has been noted in benchmark tests that the use of a Infiniband network speeds up ANSYS Fluent Simulations by over 200% [38]. The simulations are also set up conservatively by using prescribed guidelines for grid generation (meshing) and by using strategies that ensure quick flow development to steady state. The details of the solution strategy are discussed in subsequent sections. Knowledge of the computer architecture of the HPC is vital for resourceful implementation. Since computer architecture is very specific to the cluster, its details are not explored in this text.

3.1 Solution Strategy

In this work, the Finite Volume method is used to simulate turbulent flow in an infinitely periodic domain in three dimensions. A single simulation case uses DNS to capture a majority of the scales of turbulence up to the dissipative scales. A majority of the simulations make use of the LES and RANS techniques to model turbulence in order to save computational effort. The simulation strategy for these simulations is depicted in the flowchart in Figure 3.1. Subsequent sections talk about the methods used in this work for meshing, solver setup, time advancement, and initial solution field specification.

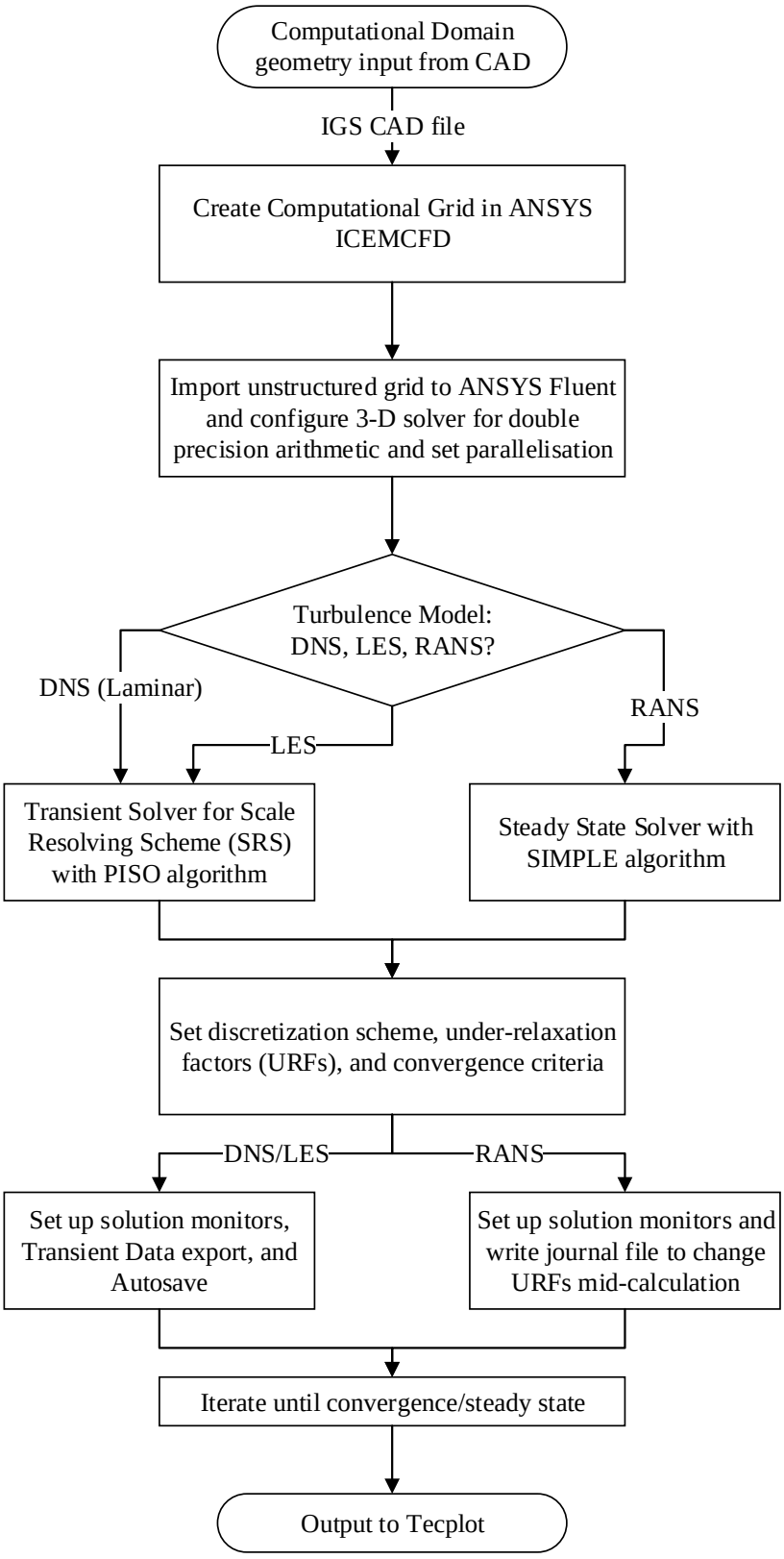

Figure 3.1: Setup procedure for performing numerical simulations in ANSYS 16.0.

3.2 Computation Grid Generation

Computational grid generation is a vital step in numerical simulations that directly controls the computation efficiency of the simulation and the accuracy of the solution. In ANSYS 16.0, two grid generation tools are available – ANSYS Meshing, and ANSYS ICEMCFD. ANSYS Meshing is a powerful tool that utilizes automatic algorithms to generate grids that satisfy global quality criteria using an unstructured topology. Typically, the methods that are available for CFD in ANSYS Meshing use an Advancing Front methodology starting from the surface grid to fill the volume of the computational domain using both Hexagonal and Tetrahedral Cells (it is also possible to choose a single type of cell geometry). Octree methods that fill the volume first and then perform refinement near the surfaces are also available.

In this work, the use of simple geometry enables extensive user customization of grids with the use of the ANSYS ICEMCFD package. ANSYS ICEMCFD offers a range of automatic grid generation algorithms also, but it is chosen for its ability to generate block structured grids. The use of block structured grids for the choice of geometry and numerical method is ideal, since the flow is dominated by boundary layers and a spectrum of scales of turbulent structures are present. Block structured grids are controlled by user-specified grid sizing parameters that can stretch the grids near boundaries and ensure smooth transition from block to block, thereby eliminating undesirable elements. Block structured grids also possess the merits of using a structured topology, where knowledge of the cell connectivity is known a priori. This results in faster computation time and less memory used for storing the mesh, while offering excellent scalability across parallel cores. However, the computational merits are not available while using ANSYS Fluent, since it requires an unstructured grid as an input. The unstructured grid will be partitioned automatically by Fluent using a METIS algorithm.

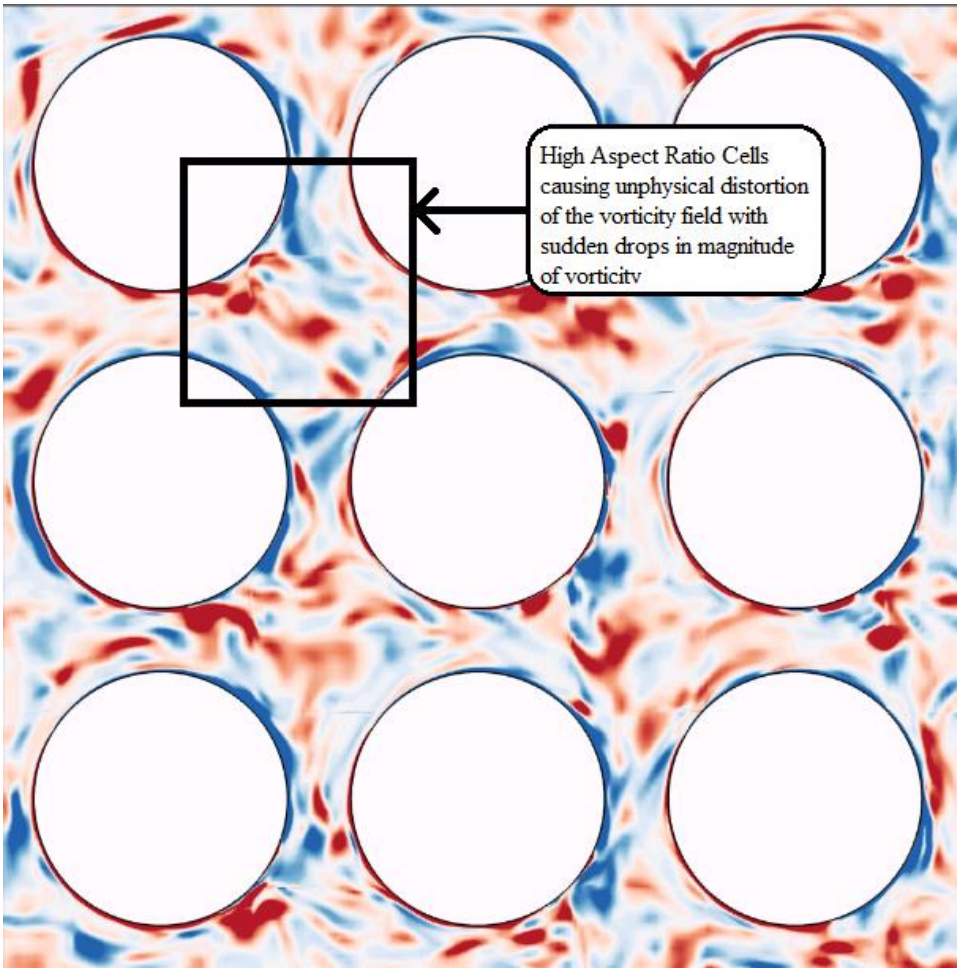

Figure 3.2: Contours of *z*-vorticity for a sample case with high aspect ratio cells in the path of the wake causing artificial dissipation of the vortex structures (visible as distinct lines).

The parameters used to judge grid quality in this work are cell aspect ratio, cell skewness, and cell-cell orthogonal connectivity. It should be noted that it is neither possible nor necessary to ensure that local quality is ensured in every cell. For instance, high aspect ratio cells at the wall cannot be avoided without an unreasonable number of cells, but these high aspect ratio cells cannot extend to the bulk of the domain. The ill effect of using high aspect ratio cells that extend to the bulk volume is shown in Figure 3.2. In this case, high aspect ratio cells that arise from the boundary are present alongside low aspect ratio cells. This results in a jump in cell size at that location that also introduces a jump in the discretization error. The jump negatively impacts the vortex shedding process by distorting the structure of vortices. The effect of high skewness and

non-orthogonality are more profound in the computation of field variable gradients. However, these problems are not encountered often in the present simulations. Several cells have high local skewness and non-orthogonality that are rectified using the solution method. Creating a perfect grid is virtually impossible while using body-fit grids.

As mentioned previously, the simplicity of the block structured grid generation method offers great control over sizing parameters. To create a block structured grid, the computational domain must be split into numerous blocks (or subdomains) that fit together seamlessly. In this work, the blocks that contain the solid obstacles are deleted, and the equations are not solved in this block. These blocks would need to be retained if the user decides to use the Immersed Boundary Method, which would become necessary as the solid obstacle shape becomes intricate. Using body-fit grids for intricate geometry would inflate the grid size drastically. Once the blocks are split suitably, algebraic sizing functions are imposed on the block edges to specify the distribution of cells within the block. An O-grid blocking strategy is used around the obstacle surface to facilitate grid stretching near the wall without affecting the cells in the surrounding blocks. The blocking strategy used in this work is shown in Figure 3.3. Once the grid is generated using the block and cell sizing specifications, the grid is then converted to an unstructured grid in the same software package to make it suitable for ANSYS Fluent.

The grid sizing requirement varies according to the turbulence model used for simulation. While the same grid that is used for DNS can be used for LES and RANS as well, the merits of using a turbulence model are lost in the process. The thought process behind grid generation for each model in this work is explained briefly to provide an idea of the kind of approximations that have been made in this work.

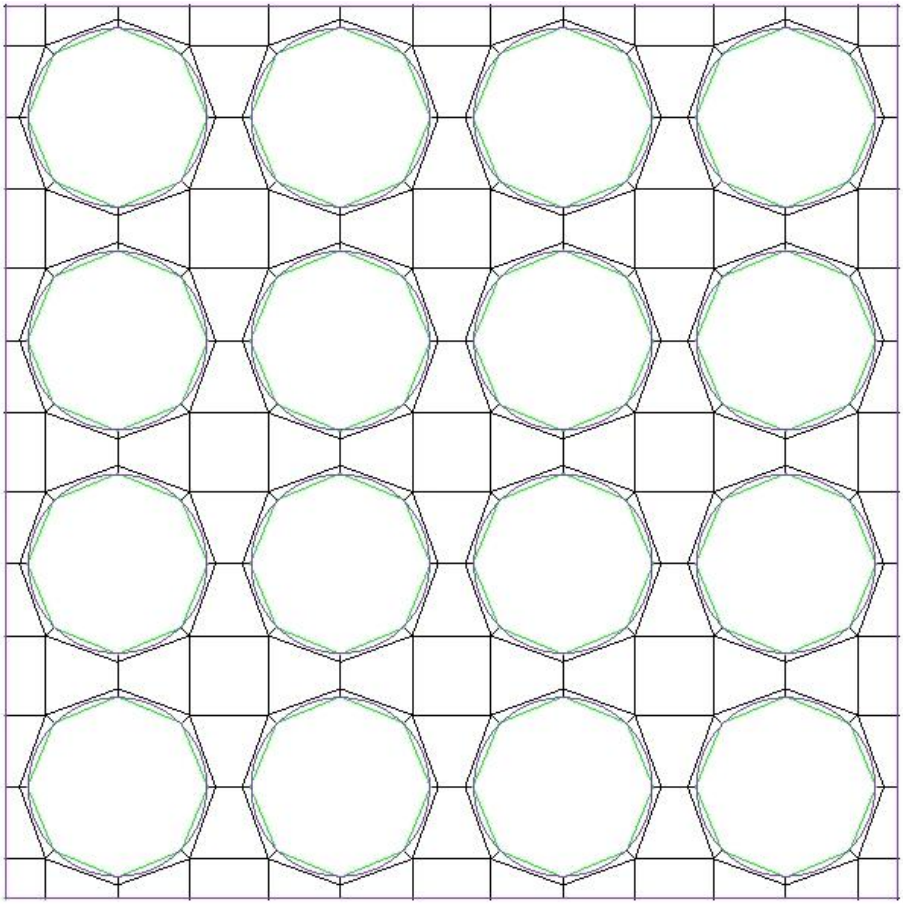

Figure 3.3: Blocking strategy for In-Line arranged solid obstacles – purple lines represent geometry, black lines represent block edges connected to two blocks, green lines represent block edges which are connected to one block.

Direct Numerical Simulation (DNS)

The requirement for computational grids for DNS are straightforward. For perfect DNS, cube shaped cells should be used to fill the domain, thereby eliminating any error due to lack of quality. The size of each cell must be sufficient to completely resolve an eddy the size of the Kolmogorov length scale (η). A simple modified wave number analysis will provide the required grid size to capture a sine wave which is the size of the Kolmogorov Length Scale. The Kolmogorov Length Scale can be estimated using Equation (3.1).

$$\eta = \left(\frac{\nu^3}{\varepsilon}\right)^{1/4} \sim \left(\frac{\nu^3}{\left(\frac{u_m{}^3}{d}\right)}\right)^{1/4} = \frac{d}{Re_p{}^{3/4}} \qquad (3.1)$$

Where ν is kinematic viscosity, ε is the turbulence dissipation rate. Turbulence dissipation rate is estimated according to the Kolmogorov Hypothesis to obtain a relation between η and Re_p. Turbulence is expected to appear in porous media for a Pore Scale Reynolds number (Re_p) above 150. Even at this small Reynolds number value, the Kolmogorov Length Scale is expected to be smaller than the diameter of the obstacle by a factor of 1/40. It should be noted that this factor will be even smaller near the wall where turbulence dissipation is higher. The computational mesh required to resolve an eddy of this size with reasonable accuracy (~50%) is too large to use with the resources available. Since perfect DNS is not possible, compromises are made wherever necessary. At the wall, the wall normal spacing constraint is maintained such that $\Delta y^+ \sim 1$ and $\Delta y/\eta \sim 1$. It is noted by Moin and Mahesh [39] that the contribution of the eddy scales of below 15η towards the mean dissipation is negligible in isotropic turbulence. Assuming that the scales of turbulence below 15η are isotropic is reasonable in the bulk flow. Since the near-wall turbulence cannot be accurately captured with the available resources, it is left under-resolved in this work. When the grids are stretched near the boundaries, the perfect aspect ratio cells are lost and streamwise placement of cells need to be taken into consideration. The grid is generated such that 200 cells are placed along the circumference of the cylinder and the cells along the length of the cylinder are designed to have an aspect ratio of 1 in the bulk. To estimate the local Kolmogorov length scale, precursor RANS simulations are performed to obtain an estimate of ε. For the choice of Reynolds number for DNS (Re_p = 1,000), the grid size is fixed to be less than 100,000,000 cells in order to be able to complete the simulation in a reasonable amount of time. In spite of making these approximations, the grid size turned out to be

~90,000,000 cells and the simulation took 4 weeks to simulate with 200 Intel Xeon processors in the NC State Linux Cluster. The lack of availability of time and computational allocations warrants the use of a less intensive method that would still deliver reliable data.

Large Eddy Simulation (LES)

Large Eddy Simulations enable the use of coarse grids for simulation that need not resolve all the way up to the dissipative eddy scales. As discussed previously, LES functions on the premise that not all scales of turbulence contribute equally to the solution field and that the potency of the scale to effect significant change reduces with its size. While simulating three dimensional flows, an increase in grid sizing by a factor of 2 reduces the grid size by 8 times, which amounts to a substantial saving in terms of CPU-Hours used for simulation. In LES, using coarse grids to resolve the velocity field would need to be augmented with SubGrid Scale (SGS) models to reduce the overall error in numerical discretization. The SGS model used in this work assumes that the unresolved scales of turbulence are isotropic in nature. Since this model has delivered satisfactory results for a wide range of flows with internal and external flows, both of which possess flow features that appear in this geometry, the calculations are proceeded by assuming that only the largest scale eddies are strongly anisotropic. The grids for LES are designed as per the guidelines provided by Choi and Moin [40] and Chapman [41]. These guidelines are designed for external aerodynamics flows and are used with confidence in this work since the flows are similar. The requirements for internal flows are less stringent and are therefore implicitly satisfied. In previous work, it was observed that the behaviour of the flow changes with porosity. For the range of porosity $0.43 \leq \varphi \leq 0.67$, the boundary layer for each obstacle is assumed to interact with the boundary layer on other obstacles to form a profile that spans the entire width. For the range of porosity $0.67 \leq \varphi \leq 0.80$, the boundary layers are assumed to form

independently. Note that these assumptions are made for the purpose of grid generation only. The Chapman estimate of grid sizing for LES specifies the number of points that are required to be placed in the boundary layer in order to resolve it, which requires pre-requisite knowledge of the expected width of the boundary layer. Chapman also recommends that the first cell be placed such that $\Delta y^+ \leq 1.5$, and that the second cell be placed within the viscous sublayer. Theoretically, this is sufficient to capture the linear profile that is expected in the viscous sublayer. In this work, more than two points are placed in the viscous sublayer since wall stress is a parameter of interest. The cell size growth ratio is limited to 1.1, and cell size matching is ensured at all edges. LES is highly sensitive to abrupt changes in cell size. In LES, both discretization error and turbulence modelling error are coupled with the cell size. A sudden change in cell size would result in an unphysical drop in the SubGrid Scale eddy viscosity, which negatively impacts the solution field. The implementation of a cell volume dependent mathematical model in LES requires careful selection of grid sizing parameters. The maximum size limit of the cells in the grid is set to be equal to the Taylor Microscale of the flow. The Taylor Microscale was initially believed to mark the beginning of the Inertial range of eddies in the turbulence spectrum. Presently, it is believed that the Taylor Microscale of the flow represents a length scale below which viscous effects are significant. Using the Taylor Microscale as the filter cut-off width has yielded accurate results for channel flows [42], while used with isotropic LES SGS models. The Taylor Microscale of flow was estimated as given by Equation (3.2) (refer Pope [16]).

$$\frac{\lambda}{d} = \sqrt{10} Re_p{}^{-0.5} \qquad (3.2)$$

From the estimated value of Taylor Microscale at Re_p = 10,000, 100 points are placed on the circumference of the cylinder. In those cases with sharp corners, the grids are stretched on the circumference to populate grid points near the vertices.

Reynolds Averaged Navier-Stokes (RANS) simulation

RANS simulations are less stringent in their requirement for grid sizing since none of the scales of turbulence are resolved. The end result will contain only a vortex pair attached behind each solid obstacle. The maximum grid size needs to be small enough to resolve the vortex pair only. RANS simulations model the entire spectrum of turbulence scales using a physical model that is based on the concept of Reynolds Averaging. The model also assumes isotropy in turbulence by representing the characteristic velocity using the turbulence kinetic energy. Since physical grid requirements do not appear to be stringent, care is taken to ensure that the model grid requirements are satisfied. Virtually the same mesh is used in the *xy*- plane in order to maintain a $\Delta y+$ of unity at the wall and to capture the boundary layer with an adequate number of cells. However, since vortex generation and dynamics are not a factor in this simulation, the cell count in the *z*- direction is reduced significantly, since no gradients are expected in that direction for a steady state Reynolds Averaged result. This intuition is proven right in simulations, and is utilized in all the RANS cases. The maximum limit for the aspect ratio of the cells in the bulk is set to 5. Note that the algebraic sizing function only makes use of the cell size, growth ratio, and the global maximum cell size to populate the grid. The aspect ratio has to be implicitly set by specifying the maximum cell size.

A sample grid created using the blocking strategy in Figure 3 is shown in Figure 5. In all of the cases in this work, grid matching is ensured between boundaries in each direction. Matching boundaries are preferred while forming periodic boundary conditions so that the high and low boundaries contain the same distribution of cells. If the cells are mismatched, the solution on one boundary would have to be interpolated on its periodic shadow, thereby requiring more time for computation while introducing an additional error term from the interpolation function.

3.3 Solver Setup

Solver setup involves the following steps - grid partitioning, choosing the governing equations, the discretization scheme, setting the boundary conditions. A brief overview of the methods used are presented in this section. The grid is partitioned automatically for the selected number of processors by ANSYS Fluent using the METIS partitioner. The METIS partitioner coalesces fine grid cells to form a coarse mesh and then partitions the coarse mesh. The partitions are then uncoarsened and refined. A pressure based segregated solver is used with the PISO scheme (see Issa [43]) for LES and DNS, and the SIMPLE scheme (see Patnakar [44]) for RANS. A second order accurate discretization scheme is used for the spatial terms and for time advancement (time advancement is used only for LES & DNS; RANS uses a steady state solver). For LES, a Central Differencing Scheme is used for both the convection and diffusion terms. Central Differencing Schemes are less diffusive than Upwind schemes, but its merits come at the price of numerical stability. Using a Central Differencing Scheme for the convection terms makes the solution prone to numerical oscillations. To avoid this, the scheme known in ANSYS Fluent as Bounded Central Differencing Scheme is used for simulations that uses the Central Differencing Scheme as long as the variables satisfy a boundedness criterion. When the boundedness criterion is not satisfied, an upwind scheme is used locally to ensure stability. This scheme is particularly useful for LES, where the turbulence model introduces a lot of numerical diffusion in the form of the SubGrid Scale Stresses. For DNS and RANS, the second order accurate Upwind Scheme is used for the convection terms to avoid issues due to stability. Upwind Differencing Schemes are not ideal for DNS due to their dissipative nature. However, using a Central Differencing Scheme produced a solution with unphysical oscillations. Since ANSYS Fluent is not designed to perform DNS, the “laminar” flow model is used, and it is assumed that the laminar solver

algorithm is not equipped to handle turbulent flows. Introducing numerical dissipation in the form of the Upwind Differencing Scheme solved the issue. This choice of differencing scheme takes a toll on the accuracy of the simulation.

The GPM geometry is assumed to be infinitely periodic in this work. This implies that all boundaries observe the periodic boundary condition. The velocity and pressure specification on the domain boundaries is unknown. With no information about the flow a priori, the pressure gradient that drives the flow would have to be estimated. To obtain the desired Reynolds number of flow, this method of momentum source specification is not good practice as it relies on trial and error to arrive at the desired magnitude of pressure gradient. It should be noted that explicit specification of the momentum source, while yielding excellent convergence within the time step, would require an enormous number of time steps for flow development. Since the transient behavior of the flow from a static condition is not of interest in all simulations, the trial and error is automated in the algorithm such that the solver maintains a specified mass flow rate. An initial guess is provided and the magnitude of the momentum source is adjusted twice per iteration while computing the mass fluxes in the PISO algorithm. A velocity field is obtained with the guess value of the momentum source. The discrepancy in mass flow rate between the calculation and specification is computed from the velocity field and the momentum source is adjusted by scaling the mass flow discrepancy into the form of a dynamic pressure which is use to correct the momentum source term. This method introduces large amplitude oscillations in the initial time steps during which time, the solution is not to be trusted. Once the large amplitude oscillations vanish, the solution field may be used for analysis or for statistical sampling if a steady state has also been reached. It should be noted that the disappearance of large amplitude oscillations is independent of attaining a steady state condition. If the initial guess is accurate, the large

amplitude oscillations may vanish before a statistically steady state is reached. The source term correction procedure leaves its signature on all the field variables, as shown in Figure 3.4.

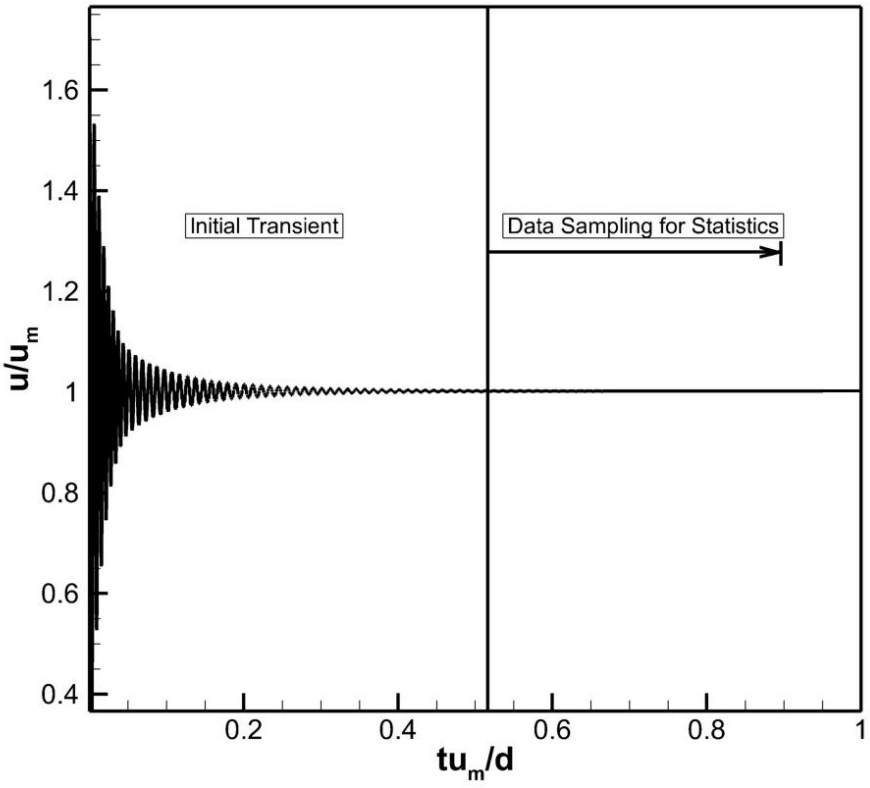

Figure 3.4: Time history of the volume averaged velocity magnitude illustrating the initial transient stage in simulations with mass flow rate specification.

For simulations where the initial transient stage is important, the steady state solution is first obtained so that the magnitude of momentum source is known. The momentum source is specified directly and mass flow rate is ensured with reasonable accuracy such that the Reynolds number does not change. Since the momentum source term is sensitive to the turbulence model in these cases, the transient simulations cannot be performed with the momentum source specification from a different model.

3.4 Initial Flow field specification

The initial flow field specification is a very important step in the solution process which has the potential to accelerate the flow development process and also aid in convergence. For transient simulations with LES and DNS, several methods are used to specify the initial flow field. The simplest initial flow field specification is that with a constant variable specification. The entire solution field can be set to zero velocity and zero gauge pressure and the solution can be started with confidence that this specification is physically sound. This method introduces additional stages in the flow development process that prolongs the length of the simulation unnecessarily. A better specification can be made, especially since the steady state solution is independent of the initial flow specification. An alternate method is to impose perturbations on a constant velocity flow field that accelerates the process of turbulence formation and development. To do so, the constant velocity field is modified by adding a zero mean spectral perturbation field. A sample initial solution field using this method is provided in Figure 3.5.

Both of the above methods are used in this work when the simulation required the initial transient to be captured. For simulations till steady state, another method of specification was used which interpolates a steady state solution from a very coarse grid onto the fine grid, thereby providing a realistic starting solution that also saves computation time. Data from steady state RANS simulations can also be used as an initial solution. However, the RANS solution field would still require imposed spectral perturbations to mimic the effect of turbulence. The coarse mesh solution initialization method is preferred, since the same field variables would be used and the variables can be interpolated easily.

Since ANSYS Fluent is a well-validated, robust solver, the initial flow specification is not of great concern for the steady state solver. However, steps are taken in this work to ensure that

the convergence rate is improved. The initial flow field for the RANS steady state simulations comes from solving the Euler equations of flow on successively finer grids in order to provide an initial velocity field that introduces the boundary conditions into the solution before the iterations start to experience the brunt of the viscous terms.

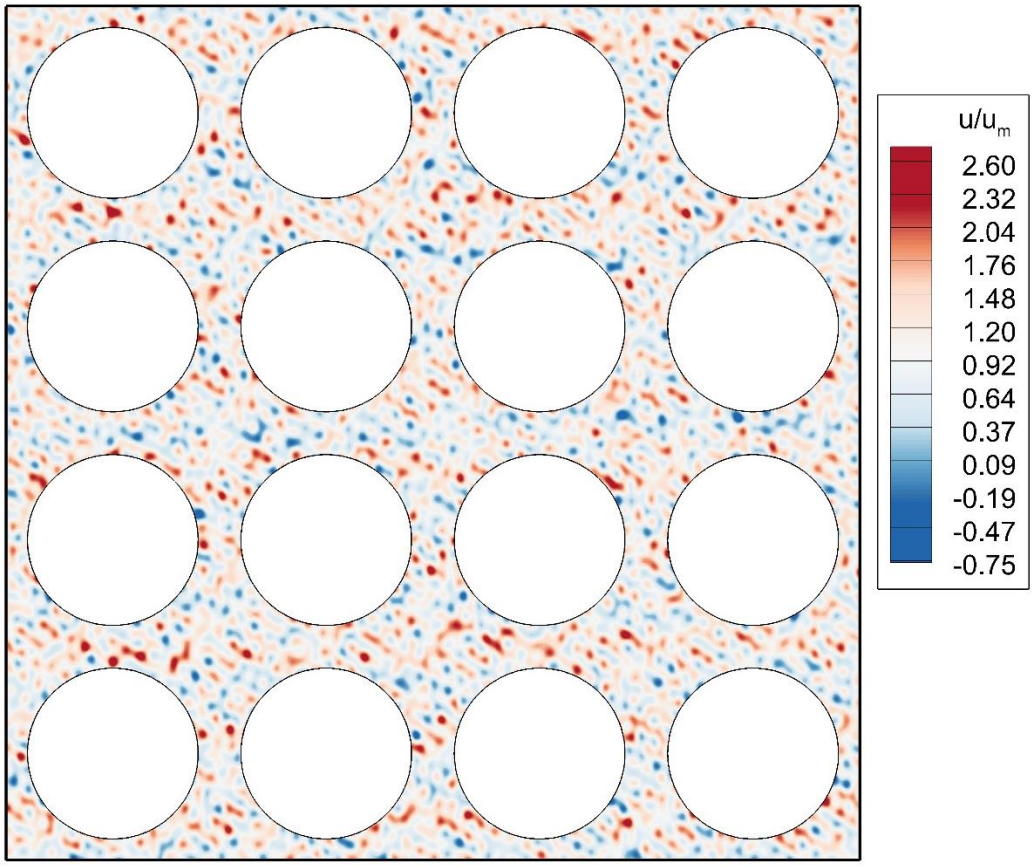

Figure 3.5: Spectral perturbations imposed on a uniform velocity field of unit magnitude, used as an initial solution for scale resolving simulations.

3.5 Simulation Quality Parameters

A grid convergence study is not possible in the case of LES, since the quality is expected to increase until the mesh resolution approaches the requirements for Direct Numerical Simulations. The quality of simulations is assessed using a parameter known as the Index of Quality [45]. The Index of Quality is a parameter that is best suited for isotropic turbulence and is used advisedly to provide a reasonable measure of quality. An index value of unity

corresponds to a fully resolved turbulent flow. LES_IQ values for the present simulations have been calculated to be consistently greater than 0.85, which falls within reasonable approximation of the scales of turbulence for the LES method. For DNS, the quality parameter, Δ, is utilised as per refs. [5] [6] [11]. The parameter measures the discrepancy in mechanical energy loss when calculated by two methods – loss measured across the boundaries of the computational domain and loss measured in the volume of the computational domain. Since the energy equation is not solved during simulations, it opens up an opportunity to verify the accuracy of the simulation. By manipulating the governing equations for momentum, a single equation can be written that conserves the mechanical energy in the domain. The mechanical energy that is lost in the domain must be compensated by the applied pressure gradient for the system to satisfy energy conservation. This method is well defined for DNS, but using it with LES would require the knowledge of the SubGrid Scale variables and the LES_IQ serves as a simple method to test the quality of the simulation.

4. RESULTS AND DISCUSSION

In previous work (see Section 1.3), turbulent flow was simulated in homogeneous porous media for a wide range of porosity to study the dependence of the turbulence structures on porosity. A symmetry-breaking phenomenon was introduced in Section 1.3, where the momentum of the fluid is seen to deviate from the principal direction along which the pressure gradient is applied. To study this phenomenon in detail is the objective of this thesis. In order to study the phenomenon, the following cases were set up, that are summarized in Tables 4.1 – 4.6.

Simulations are performed for a range of porosities within the critical value, above which symmetry-breaking will not occur at a Reynolds number of 10,000. The simulations are first performed using LES for different values of porosity, and are validated using RANS simulations and DNS. Parametric variations are implemented by changing the shape of the obstacles. The shape of the obstacles are expected to have a significant impact on both the macroscopic and microscopic flow. Most of the simulations are performed for 2-D GPMs. However, 3-D GPMs are also a frequent occurrence in practice, hence, a single simulation with spherical obstacles in a 3-D GPM is used to verify the occurrence of the phenomenon in the absence of two dimensionality. The cost of simulating flow in 3-D GPMs is higher as the REV-T domain size would increase and the number of cells required to fit the body of the obstacles are higher. Continuing with parametric variations, a series of simulations are performed for a wide range of Reynolds numbers to find out the critical Reynolds number above which the phenomenon would occur. Symmetry-breaking is not expected to occur at extremely low Reynolds numbers due to a lack of supply in momentum. LES is used for simulations at different Reynolds numbers because of its superior performance in the Transition regime to that the RANS schemes that are available in ANSYS Fluent. Once it is verified that the symmetry breaking phenomenon occurs at

reasonably low Reynolds numbers, the use of Direct Numerical Simulation (DNS) became viable. The use of DNS for a Reynolds number of 10,000 is not possible with the resources available at this time. Simulations are also performed using the RANS method to investigate the effect of obstacle arrangement in the GPM, and the effect of obstacle surface roughness on symmetry-breaking.

Table 4.1: LES cases for Circular Cylinder Obstacles at Re_p = 10,000 for different values of porosity to study the dependence of macroscopic flow angle on the extent of confinement.

Case ID	**Porosity, ϕ**	***d/s***	**Applied Pressure, $g_x d/\rho u_m^2$**	**Δy^+**	**LES_IQ**
1	0.43	0.85	7.15	1.08	0.87
2	0.50	0.80	4.38	0.95	0.87
3	0.56	0.75	2.56	1.20	0.87
4	0.61	0.70	1.96	1.09	0.87
5	0.67	0.65	0.80	1.02	0.90
6	0.72	0.60	0.53	0.99	0.89
7	0.8	0.5	0.21	1.07	0.91

Table 4.2: RANS cases for Circular Cylinder Obstacles at Re_p = 10,000 for different values of porosity to validate the LES results.

Case ID	Porosity, ϕ	*d/s*	Applied Pressure, $g_x d/\rho u_m^2$	Δy^+
8	0.43	0.85	6.35	1.01
9	0.50	0.80	3.49	0.92
10	0.56	0.75	2.36	1.25
11	0.61	0.70	1.45	1.01
12	0.67	0.65	0.64	1.12
13	0.72	0.60	0.45	0.92
14	0.8	0.5	0.18	1.01

Table 4.3: LES cases for 2-D and 3-D GPMs at Re_p = 10,000 for different solid obstacle geometries to study the dependence of GPM geometry.

Case ID	Obstacle Shape	Porosity, ϕ	Applied Pressure, $g_x d/\rho u_m^2$	Δy^+	LES_IQ
15	Square Cylinder	0.50	0.36	0.80	0.84
16	Square Cylinder	0.67	0.15	0.75	0.88
17	Sphere	0.72	0.44	0.53	0.93

Table 4.4: LES cases for Circular Cylinder Obstacles for different values of Reynolds number to study the dependence of macroscopic flow angle on the availability of momentum.

Case ID	Porosity, ϕ	Reynolds Number, Re_p	Applied Pressure, $g_x d/\rho u_m^2$	Δy^+	LES_IQ
18	0.5	100	0.064	N.A.	N.A.
19	0.5	500	0.38	0.21	0.95
20	0.5	3000	2.07	0.4	0.92

Table 4.5: DNS case for Circular Cylinder Obstacles for $Re_p = 1{,}000$ and $\varphi = 0.5$ to determine the independence from turbulence models.

Case ID	(%Error) $\langle\theta\rangle^i$	Δx^+	Δy^+	Δz^+	Δ (%)
21	1.37	8.53	1.22	12.18	16.8

Table 4.6: RANS cases for Circular Cylinder Obstacles at $Re_p = 10{,}000$ and $\varphi = 0.5$ for a staggered solid obstacle arrangement.

Case ID	Obstacle Arrangement	Staggering Angle	Applied Pressure, $g_x d/\rho u_m^2$	Δy^+
22	Horizontally staggered	26.5^o	1.98	0.94
23	Vertically staggered		3.05	1.02

Before proceeding to a detailed analysis of the phenomenon and its dependence on geometric and flow parameters, it is important to identify the key features of the flow and introduce a naming convention for the flow and geometric features to avoid confusion in the sections to come. The naming convention is presented in Figure S.1.

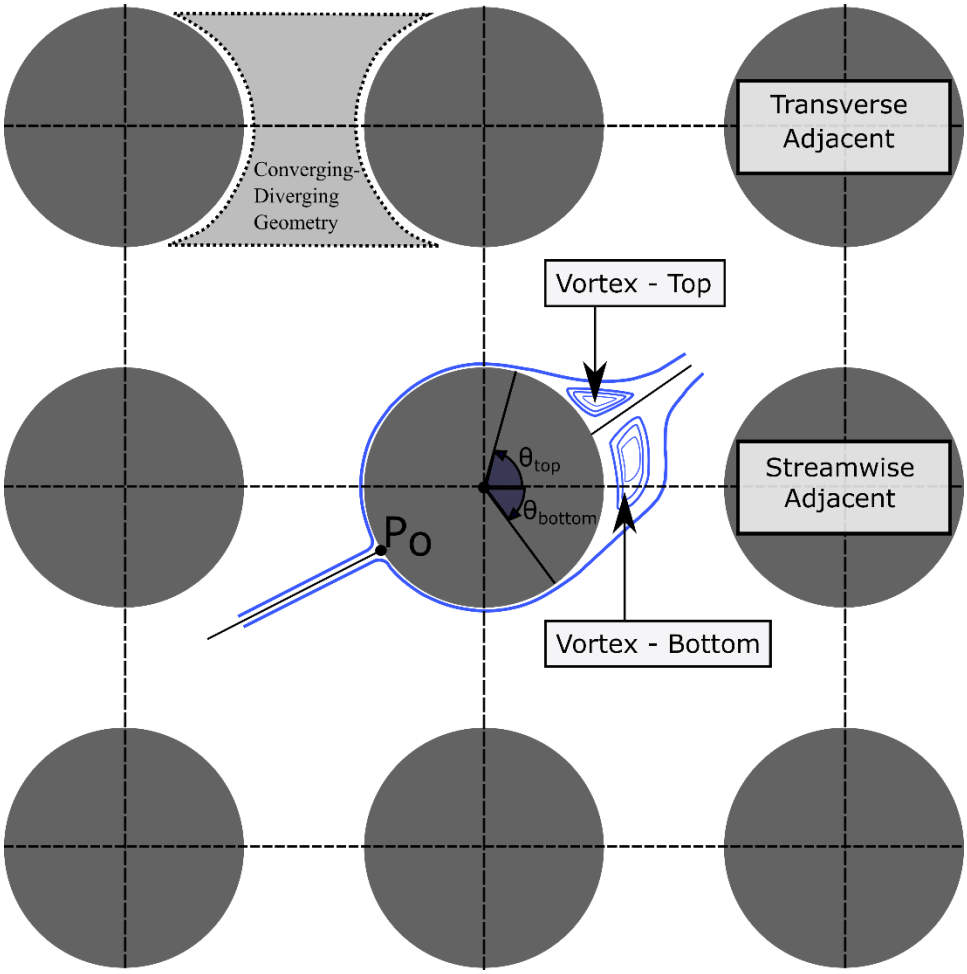

Figure 4.1: Naming convention for elements of the vortex shedding process.

4.1 A description of the Symmetry Breaking Phenomenon

The most striking observation from Figure 4.2 is that the macroscopic flow angle is dependent on porosity, which highlights the extent of confinement induced by the solid obstacles. There exists a regime of flow with regard to porosity ($\varphi>0.95$) where the flow pattern surrounding a GPM obstacle behaves independent of other obstacles in the medium. True independence is virtually

impossible. However, the interaction between the wake behind an obstacle and the surface of the streamwise adjacent obstacle is weak and the wake interaction between transverse adjacent obstacles is non-existent. Note that the streamwise adjacent obstacles are located along the principal direction while the transverse adjacent obstacles are located normal to the principal direction, above the streamwise adjacent obstacle. This would result in the flow possessing characteristics that are typically observed in external flows. In the case of lower porosities ($0.8<\varphi<0.95$), a strong interaction exists between streamwise adjacent obstacles with the wake from one obstacle impinging on the wall of the streamwise adjacent obstacle.

In porous media with low porosity ($\varphi<0.8$), the influence of the proximity of the walls of the adjacent obstacles becomes apparent. For these geometries, the flow possesses characteristics that are similar to that of internal flows. At $\varphi=0.8$, the smallest gap in between adjacent obstacles is equivalent to the obstacle diameter. As the porosity reduces further, the gap reduces as well, while the obstacle diameter continues to increase. The size of vortices scales with the diameter of the obstacle in the case of external flows. This is indeed what would happen in the case of high porosity ($\varphi\geq0.8$), where there is sufficient room for the vortices to form and dissipate between streamwise adjacent cylinders.

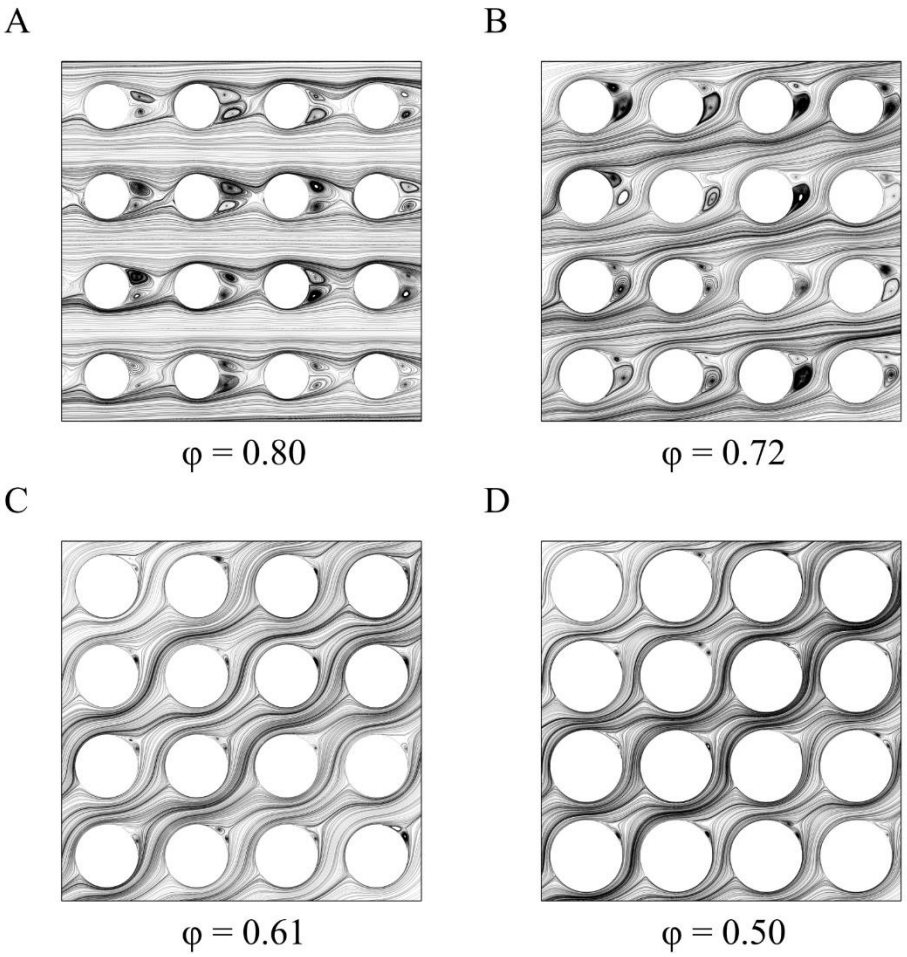

Figure 4.2: Mean flow streamlines at the midplane for varying porosity φ (A-D) show the presence of a macroscopic flow angle that depends on φ.

For the case of low porosity, the inherent confinement alters the flow behaviour resulting in two possible scenarios. The decisive factor for each scenario is determined by the ability of the flow to remain attached to the surface of the obstacle. This ability is directly derived from the supply of momentum in regions of demand. In the dire absence of supply, the flow is forced to separate at a prescribed location while preserving symmetry. The vortex that is associated with this separation point is typically large and would scale with the size of the obstacle. A vortex of this size cannot be transported in a medium that is as constrained. When the size of the shed vortex is comparable to the gap between two obstacles, the vortex cannot maintain its form as it passes through the gap due to the presence of a strong local adverse pressure gradient in the gap.

In a sense, the vortex would plug the porous medium until the vortex disintegrates. However, this does not happen in practice owing to the massive loss in momentum that would have incurred. Rather, the generated vortex forms a zone of recirculation in between the streamwise adjacent obstacles. The bulk of the flow continues to pass over the recirculation zones since the gap is "bridged" by the vortices. The recirculating vortices are slowly and continually dissipated in the shear layer in between the recirculation zone and the bulk flow in the form of a Kelvin-Helmholtz instability, thereby making room for new fluid that enters the recirculation zone after separation.

If adequate momentum is available to the fluid, the flow follows a different path that results in the deviatory flow that is seen in Figure 4.2. The associated Reynolds number of flow marks the incidence of the von Karman instability which is characterized by a detached vortex system. The vortex shedding process has to mutate in a manner that allows for more room for dissipation. A change in the location of the separation point, such that the locations are not symmetric, causes a shift in the direction of vortex shedding such that the vortices no longer impinge on the streamwise adjacent obstacle that is in such close proximity. In the case with porosity $\varphi = 0.72$, the gap between adjacent cylinders is sufficiently large, allowing the formation of a vortex on either side of the obstacle symmetry plane. Asymmetry in the location of the separation point tilts the shedding path and allows the vortices to be dissipated in the mean flow. As a result of this shift, it can be observed that the vortices formed by this procedure are of different sizes. As the porosity is lowered further ($\varphi \leq 0.61$), the flow remains forcibly attached under the influence of the stagnation pressure for long enough to separate on the same side of the obstacle symmetry plane. Separation on either side of the obstacle symmetry plane is not possible here since the gap is too small to allow the vortex that is formed on one side to enter the

mean flow on the other side. Since vortices propagate in the direction dictated by the separated shear layer, separation on the same side results in the interaction between transverse adjacent obstacles. The wakes of the obstacles in the case of low porosity impinge on the transverse adjacent obstacle rather than the streamwise adjacent obstacle.

In order to understand the asymmetrical nature of the mean flow and the change in the separation point, some features of the geometry that correspond to internal flows must be considered. The periodic arrangement of obstacles is perceived differently by the flow in the case of low porosity. Rather than looking at the arrangement in terms of the obstacles, one must think of the GPM for low porosity as an arrangement of paths for the fluid. The GPM is essentially formed by a network of "converging-diverging" nozzles that are connected in two directions. This enables a possible explanation for the ability of the flow to remain attached in the converging portion of the nozzle due to the additional momentum supplied by the favourable pressure gradient that typically exists in converging nozzles. This ability is enhanced as the porosity becomes lower, until a critical value is reached where the two obstacles are close enough that the flow would be forced to trip from the influence of the constriction. To visualize this better, a simulation is performed starting from a constant, symmetric initial solution until the deviatory flow is sustained. The simulation is performed for a Pore Scale Reynolds number (Re_p) of 10,000, which is well within the limit of fully turbulent flows [13], and for a porosity of 0.50, which is not close to any critical value of the governing parameters.

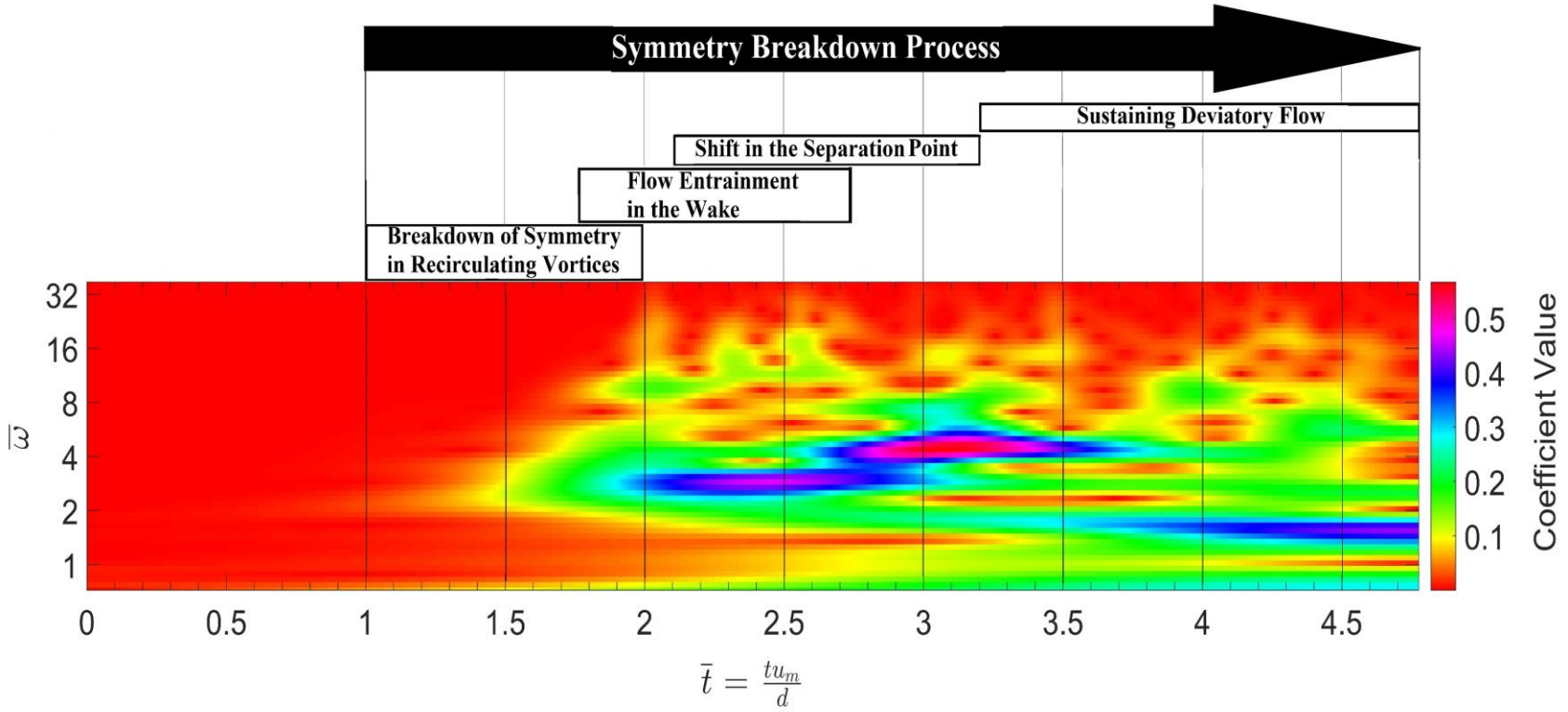

Figure 4.3: CWT scalogram plot for the time signal of *y*- velocity probed at the geometric centre of the streamwise adjacent void. The scalogram shows the various stages towards the breakdown of symmetry, which highlights key time strands in the dataset that must be analysed to understand the progression of symmetry breaking. The contours are coloured by the normalized amplitude of the wavelets whose change in value represents the significance of the event at that time. The frequency (vertical) axis represents the rate at which the event occurs. The scalogram is correlated with streamline plots to obtain the accurate location of the time strands. The flow is balanced by symmetry initially, denoted by the region with zero amplitude. The amplitude builds up slowly followed by rapidly occurring events leading to deviatory flow, indicating a non-linear build-up of asymmetry. The peaks associated with flow entrainment and separation point relocation are located at a higher frequency band than the remainder of the flow. The frequency segregation informs, prior to the streamline analysis, of the rapid nature of change in higher frequency time strands to ensure that important flow features are not ignored.

The enormous dataset (collected from 15,000 time steps) that is acquired by collecting the time history of field variables must be processed suitably to extract the important features. Mere visualization is insufficient owing to the sheer volume of information that is presented concurrently. Continuous Wavelet Transform (CWT) is used as a tool to identify the time intervals in which significant events take place. A data probe for the *y*-velocity is placed in the centroid of the void in between streamwise adjacent obstacles. The time history of the *y*-velocity is transformed into wavenumber space varying with time. Significant events are identified based on the magnitude of the coefficients of the wavelet weighting function (see Figure 4.3).

4.1.1 Preservation of Initial Symmetry

Starting from a uniform flow field, the initial stage, up until the flow first separates, closely resembles a creeping flow scenario with the flow streamlines closely following the contours laid out by the walls of the obstacles. This attached flow behaviour cannot be sustained at this large value of Reynolds number. The flow separates as early as $\bar{t}$ = 0.2 (*t* is non-dimensionalized with d/u_m).

4.1.2 Development of Asymmetry

The Navier-Stokes equations are non-linear, which contributes random characteristics of its own accord. The von Karman instability does not require the initial flow to contain any perturbations for the instability to manifest in a manner that breaks symmetry. Since the recirculating vortices are detached from the surface of the obstacle, a second shedding cycle occurs once again in a manner that preserves symmetry. However, this symmetry is short-lived as the newly formed vortex pushes into the recirculation zone causing the recirculating vortices to break down into multiple structures marking the beginning of asymmetry. It is observed that a phase difference in shedding emerges; this is characteristic of the von Karman instability. Consequently, the recirculating vortex system that breaks down does so in an uneven manner such that the

structures on the leading phase side dissipate before the structures on the lagging phase side. The lagging process ensures that the separation point on the respective side remains virtually unchanged (see Figure 4.4). In all of the simulations shown in Figure 4.2, the flow is oriented such that the transverse flow contribution is along the positive *y*-direction. It is equally probable that the flow be oriented along the negative *y*-direction. The directional preference of the deviatory flow in the *y*-direction is decided, randomly, by the initial phase difference.

The vortex breakdown process continues until all but a single vortex structure from the recirculating vortex on the leading phase side are lost to dissipation. The single remaining vortex is detached from the shedding process and lingers on the flow incident surface of the streamwise adjacent obstacle. The advancing vortex from the next shedding cycle pushes the lingering, recirculating vortex downstream. The phase difference in vortex shedding enables the lingering vortices to pass into the mean flow sequentially without having one vortex be a hindrance to the other.

The recirculating vortex on the leading side is pushed first, such that the vortex is also dissipated in the process. The passage of one vortex of the lingering pair ensures that the other one remains in the same location. The accumulation of vortex structures on the lagging side results in a low pressure region to be formed. Since the vortex has passed on the leading side, the pressure gradient in between the two sides, aided by the converging-diverging nature of the geometry, pulls fluid from the leading side to the lagging side resulting in the transverse flow contribution. It is essential that the entrainment of fluid is sustained in order for the mean flow at steady state to be oriented at an angle to the principal direction.

In symmetric flow, there are three stagnation regions on the flow incident surface of the streamwise adjacent cylinder. All three stagnation points occur at the termination point of

vortices. In symmetric flow, the magnitude of the stagnation pressure is also symmetric, thereby maintaining a balance in the pressure distribution and contributing a negligible amount of momentum in the *y*- direction. When the von Karman instability causes an imbalance and subsequently flow entrainment, the stagnation point on the leading side becomes much stronger. This imbalance in the pressure distribution on the flow incident side of the obstacle provides a driving force in the transverse direction.

Channelled by this driving force, the new vortex that is formed on the leading side deviates in its path from the principal direction to enter the converging-diverging section with momentum in the transverse direction. The vortex disintegrates in the throat of the section where it encounters an adverse pressure gradient, which is not conducive towards the preservation of the large vortex structure. This marks the passing of the first vortex in the transverse direction.

As more fluid is entrained, the separation point is dragged downstream by the favourable pressure gradient. In the case of $\varphi > 0.61$, this would be the end of the whole process and the mismatch in separation point would be sustained by the stagnation region. For lower porosity ($\varphi \leq 0.61$), the void in between streamwise adjacent obstacles is not large enough to contain this vortex system, especially since the shedding path is tilted. The shift in the separation point must continue in order to tilt the shedding path further away from the proximal obstacles.

When the shed vortices are driven by the proximity to the stagnation region, the flow has a tendency to reattach in the converging section of the geometry (for $\varphi \leq 0.61$) and separates again much closer to the lagging separation point on the same side of the plane of symmetry. The vortex that is encompassed by the separation and reattachment process resembles a separation bubble. The separation bubble is short-lived as it increases the tortuosity of the flow path and cannot be sustained. The separation bubble diminishes in size with time. Once the separation

bubble vanishes, the separation point shifts to the same side of the obstacle symmetry plane as the lagging vortex side. Once this shift is completed, the flow is sustained as long as momentum is supplied.

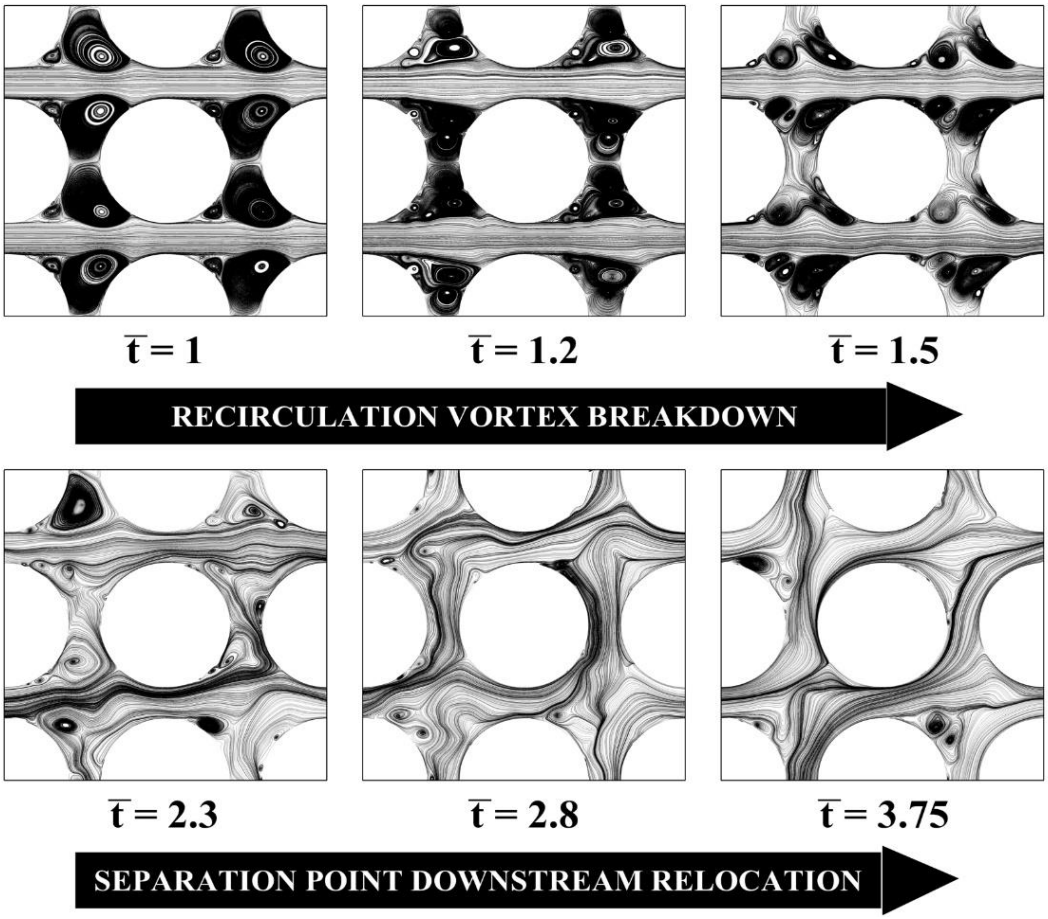

Figure 4.4: The two fundamental stages in the symmetry breakdown process are depicted with streamlines plot at significant locations in time.

The mean pressure distribution on the flow incident side of an obstacle is shown in Figure 4.5. The absence of symmetry in the pressure distribution is the driving factor for the deviatory flow in the long run. The flow propagates in the direction of negative slope of pressure. The pressure distribution appears to vary with porosity, the implications of which are discussed in the next section.

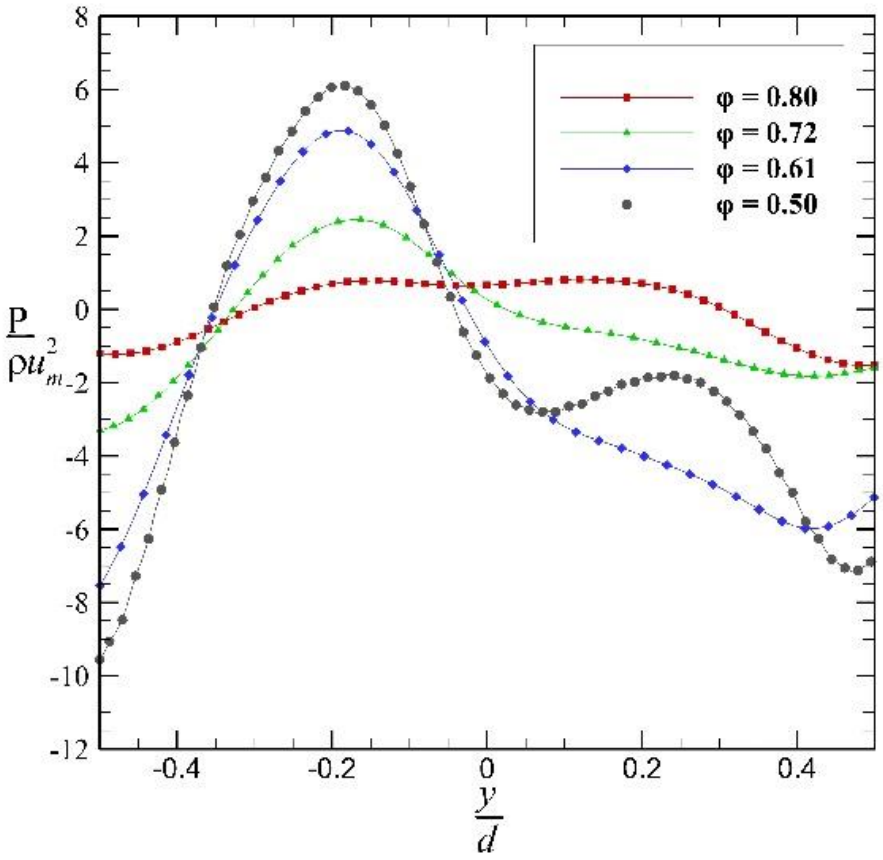

Figure 4.5: Pressure distribution (non-dimensionalized with mean bulk dynamic pressure) on the flow incident surface of the solid obstacle.

4.2 The development of symmetry breakdown from the perspective of stagnation pressure on the surface of the solid obstacle

The pressure distribution on the surface of the solid obstacles plays a critical role in symmetry breaking. The location and the magnitude of the stagnation point on the flow incident surface of the solid obstacle determines the driving force in the direction normal to the symmetry plane. The time history of the magnitude and location of the peak pressure points are plotted in Figure 4.6, which illustrates the transition from symmetric to deviatory flow. Note that the magnitude of peak pressure is non-dimensionalized with the mean dynamic pressure of the macroscopic flow. The location at which the peak pressure occurs is measured from an azimuthal angle of 180^o such

that the origin shifts to the flow incident surface of the solid obstacle. The initial flow starts out with two stagnation points associated with the symmetric two vortex system. The stagnation point that is located above the symmetry plane is denoted as the top stagnation point and the one that is located below is called the bottom stagnation point. In this case, the statistically steady flow possesses a positive *y*- momentum component, implying that the top stagnation point will vanish once the deviatory flow develops. For deviatory flow, the plot displays the peak pressure value on the top quadrant of the flow incident surface, which is not a point where the flow stagnates. The peak value of pressure in the deviatory flow is significant in its contribution to *y*-momentum as it is detrimental to the supply of momentum by the bottom stagnation point.

The observations that are made from the time variation of the magnitude and the location of the peak pressure correlate well with the features that are observed in the variation of *y*-velocity in the streamwise adjacent void (see Figure 4.3). This confirms the notion that the stagnation point and the peak pressure contribute directly to the build-up of *y*- momentum. The deviation of peak pressure (which is equivalent to the deviation in stagnation pressure until asymmetry develops) is defined in this work as σ_{P_o}, calculated as the normalized peak pressure difference. The variation of σ_{P_o} with time is plotted in Figure 4.7.

The variation of σ_{P_o} possesses many sharp peaks that are associated with the impingement of the wake emanating from the solid obstacles. While most of the peaks fall within the bracket of the dynamic standard deviation of the curve, some peak overshoots are significantly stronger than the remainder. Upon correlation with streamline plots (not presented in this work), it was concluded that the strong peak overshoots occur when the shed vortices are approaching the flow incident surface of the solid obstacles and the phase difference in shedding causes the stagnation pressure on the leading phase side to be much higher than the pressure on the lagging phase side.

These peaks illustrate the presence of a phase difference, but they have not been observed to cause any direct significant change to the driving force. Therefore, the strong peaks have been removed from Figure 4.7 using a median filtering operation with the cut-off threshold equal to the local standard deviation. The filtered data is then scaled to enunciate the regular peaks.

The flow starts off with zero deviation (a condition for symmetry) and starts to deviate at $\bar{t}$ = 0.4 (non-dimensional time is used as defined in Figure 4.3) during the formation of the first vortex pair itself. The deviation is minute, but the von Karman instability is dependent on the presence of a minute disturbance in the flow field to grow. Once the first vortex pair reaches the flow incident surface upon detachment, the stagnation pressure can be seen to shoot up, leading to a 10% deviation in favour of the top stagnation point. This is a key observation made in several visualizations, that the flow is inclined in the opposite direction first, before the complete development of asymmetry changes the direction to the positive *y*-direction. The location of the stagnation point is also symmetric until $\bar{t}$ = 1, where the first strong deviation is observed. Once the von Karman vortex mechanism sets in, peaks in deviation, magnitude, and location start to appear.

Along with the presence of peaks, the median trend of the deviation also increases until a statistically stable value is reached, denoted by mean deviation. The deviation continues to oscillate about the mean throughout the remainder of the sampling time. The increasing trend is characteristic of the build-up of asymmetry that is likely to be irreversible (which is the case here). Infinitely periodic domains are conducive to the sustenance of deviation, since an infinite fluid reservoir is available. In the absence of this infinite reservoir (for example, in cases where the porous medium fills the shape of a larger entity immersed in a fluid), such a large deviation (over 100%) may not sustain, but rather the deviation would oscillate about a smaller value.

The first peak in pressure that occurs at $\bar{t}$ = 0.8 marks the first interaction of the vortices with the surface of the adjacent solid obstacle. The impingement of the vortex pair on the surface of the solid obstacle results in a large value of stagnation pressure that is over a magnitude greater than the mean dynamic pressure of the macroscopic flow. The magnitude strength possessed by the stagnation pressure is crucial to its ability to manipulate the macroscopic flow field. Subsequently, peaks in the peak pressure magnitude plot occur whenever a vortex is incident on the surface of the solid obstacle. However, the peak pressure on the top and bottom locations develop a phase difference after the first peak leading to temporally localised pressure gradients that develop in magnitude as the vortices interact with each other. The magnitude of the stagnation pressure can be seen to reduce after the initial development stage ($\bar{t}$ > 4). The strength of the vortices that would be shed in the absence of symmetry breaking is clearly demonstrated by the magnitude of the stagnation pressure in the developmental stage, which would incur a much larger loss in the momentum of the flow.

The location of the peak pressure on the top and bottom follows a trend that is similar to that of the magnitude. Initial symmetry is preserved until $\bar{t}$ = 0.8, after which, the location of the peak pressure responds to the variation in the magnitude and σ_{P_0}. Discontinuities in the plot of the location of the peak pressure occur due to the departure of a vortex from the streamwise adjacent void. The discontinuity in location is typically accompanied by the change in orientation of the streamlines in the vicinity of the peak. The first discontinuity is observed at $\bar{t}$ = 1.5, which kick-starts the development of momentum in the *y*- direction. The departure of the vortex in this time-frame is documented in Figure 4.4. The location of the peak jumps upstream when the vortex departs in the *x*- direction and downstream when the vortex departs in the *y*- direction.

After $\bar{t}$ = 3, stagnation does not occur on the top surface and the peak pressure contributes only towards reducing the local gradient in the pressure distribution.

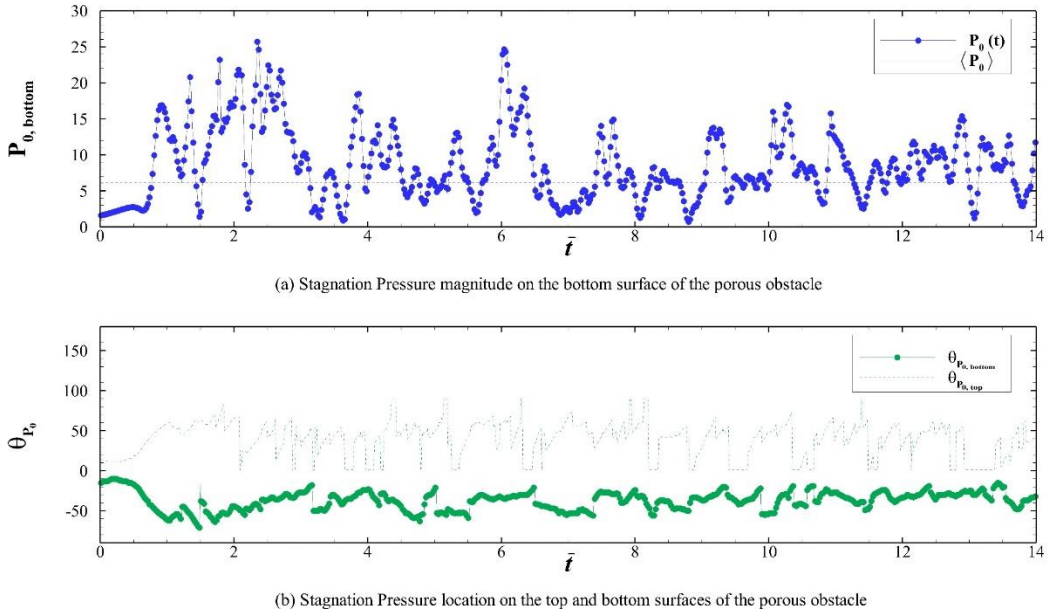

Figure 4.6: (a) Magnitude and (b) Location of the stagnation points on the surface of the solid obstacle illustrates the deviation of the magnitude and the symmetric location of the stagnation points resulting in the build-up of asymmetry and ultimately symmetry breakdown.

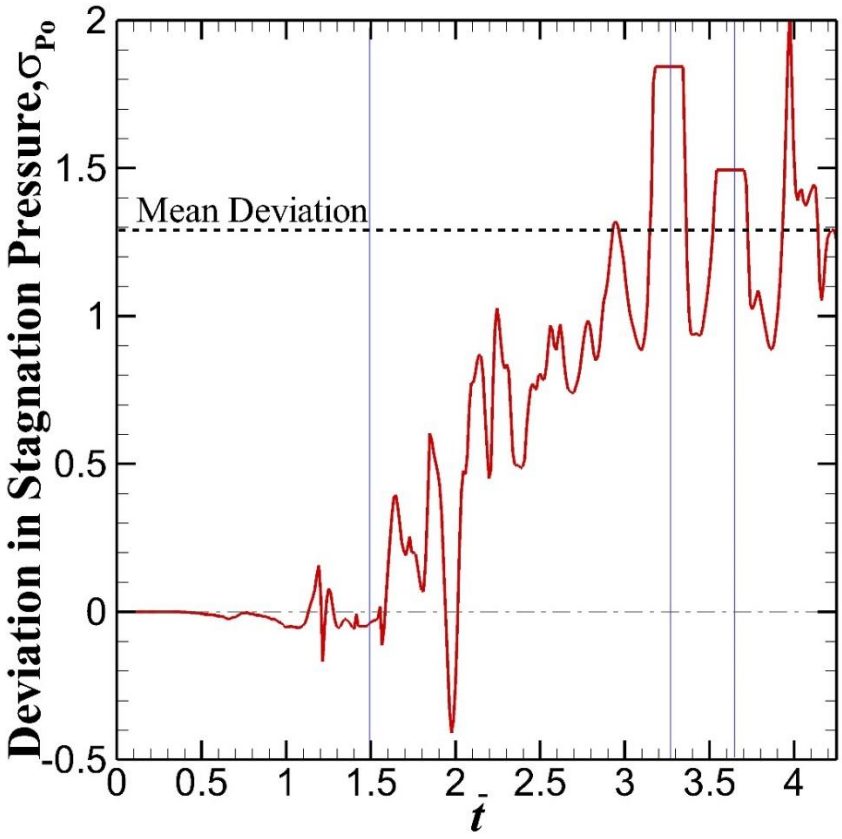

Figure 4.7: Time variation of percentage deviation in stagnation pressure magnitude betweent the top and bottom surfaces of the solid obstacle. The blue vertical lines mark the location of peak overshoots.

4.3 The parameters that control the deviatory flow

The symmetry-breaking phenomenon is not a universal effect that is present in all porous media. In fact, it is highly specific to geometry and boundary conditions. A few parameters that enable symmetry-breaking are presented here, followed by a thorough analysis of its effects.

4.3.1 Porosity

One of the observations that was made earlier is that the macroscopic flow angle changes with porosity. The macroscopic flow angle rises slowly from zero until the porosity is low enough for the vortex size to be constrained. At this stage, a large spike in macroscopic flow angle is

observed as the separation point shifts from opposing sides to the same side of the obstacle symmetry plane. A maximum exists close to $\varphi = 0.61$, after which the macroscopic flow angle reduces slowly. This is attributed to the space constraint that is posed by the larger obstacles. The mean pressure distribution is nearly symmetric for the case of $\varphi = 0.80$ (see Figure 4.5) resulting in a very small magnitude of macroscopic flow angle. As porosity reduces, asymmetry is observed in the pressure distribution and the ratio of mean stagnation pressure to the mean bulk dynamic pressure increases. This signifies that the angle increases as a consequence of the increased ability of the flow to remain attached derived from a stronger stagnation pressure. In the case of $\varphi = 0.50$, a secondary peak is observed which is still not strong enough to separate the flow. The secondary peak, however, reduces the slope of the pressure distribution which in turn reduces the macroscopic flow angle. The secondary peak is attributed to the proximity of the stagnation point on the transverse adjacent obstacle. As the porosity is reduced further, this peak is expected to grow. When the porosity is changed, the features of the flow also change to accommodate the symmetry-breaking flow field. Some of these changes are paramount to the sustenance of the deviatory flow while the remainder are caused by it. These key aspects of the flow are discussed in detail in the subsequent sections.

Measurement of the Vortex Core Size

The nomenclature of the elements of the flow that are associated with vortices and flow separation are illustrated in Figure 4.1. The variation of vortex core size with porosity in Cases 1-7 is plotted in Figure 4.8. The fundamental observation in this plot is that the individual vortices in a pair have different sizes. This implies that the shedding process is asymmetric; this is described in the Section 4.1.2.

The vortex core diameter does not vary monotonically with porosity. The sudden drop in vortex core diameter is an indication of the suppression of the vortex core size in low porosity as

a result of the decreasing void volume. A remarkable observation is that individual vortices of a pair seem to vary independently of one another in core size, as well as the nature of its variation (increases or decreases) with porosity. The vortices on the bottom (naming convention in Figure 4.1) increase in size as porosity reduces until a critical value of porosity, beyond which the size decreases. The vortex size increases first as a consequence of increasing solid obstacle diameter. The size continues to increase until the generated vortices are too large to be contained in the void volume. Beyond this point, the vortex size will reduce as dictated by the void size.

On the top side, the vortex core size decreases first as porosity is reduced until the same critical value of porosity is reached as for the bottom vortex. This reduction in size is a consequence of the growing size of the bottom vortex and the tilt in shedding path that constrains the vortex from both sides. The core size increases once the vortices start to shed on the same side of the symmetry plane of the solid obstacle. This increase is attributed to the location of the separation point for the top vortex changing to match the bottom vortex. Despite the opposing trend in vortex core size, it is worthwhile to note that the transition in slope occurs at the same porosity for both sides.

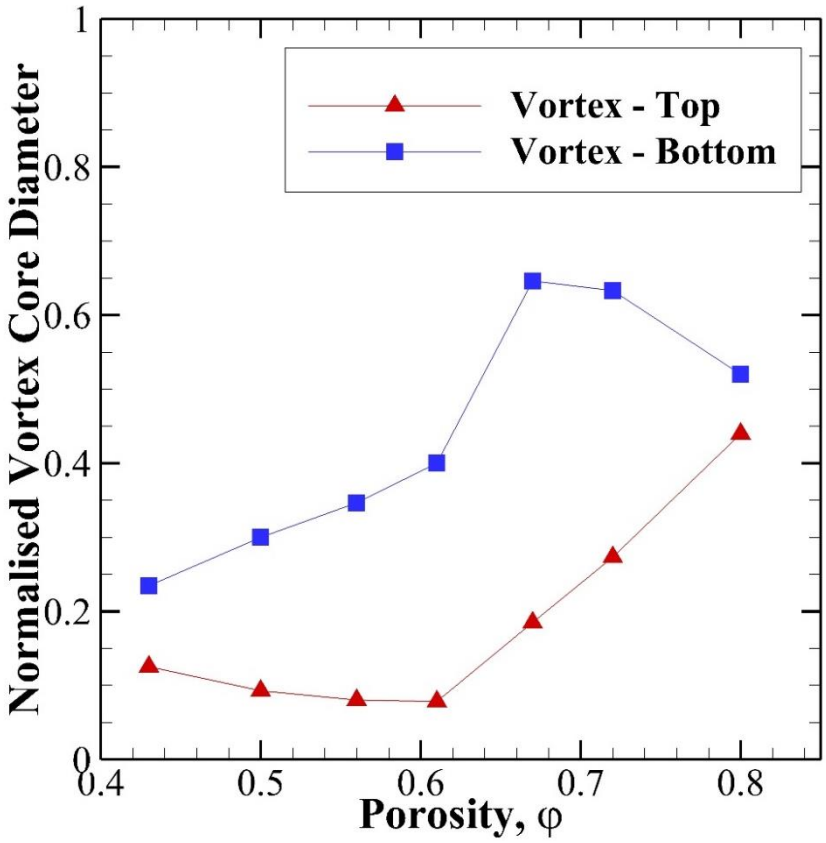

Figure 4.8: Variation of non-dimensional Vortex Core diameter with porosity for Cases 1-7.

It is expected that the size of the two vortices will become equal as porosity tends to unity. Speculation for the low porosity cases is that the vortex sizes should approach equality as well. However, the flow may separate sooner as a consequence of constriction in between adjacent obstacles resulting in a pair of symmetric vortices that will be larger than the ones predicted by extrapolation.

Influence of porosity on the macroscopic flow angle

The macroscopic flow angle, $\langle\theta\rangle^i$, is calculated as the vector angle of the filtration velocity for the REV-T. For medium porosities greater than 0.80, the flow pattern is symmetric resulting in a macroscopic flow angle of zero. The variation of macroscopic flow angle with porosity is plot in Figure 4.9. The macroscopic flow angle increases almost exponentially with decreasing porosity ($0.61<\varphi<0.8$). A large increase in macroscopic angle that results in a jump in between 0.67 and

0.61 is a consequence of the shift in the separation point from opposing sides to the same side of the symmetry plane of the solid obstacle. Some discrepancy exists as to whether this is a region of high sensitivity to porosity or whether there exists an actual jump in the macroscopic flow angle. An actual jump is more likely since the difference in characteristics of the two configurations is drastic in a way that cannot be matched. The jump occurs at the value of porosity where the hindrance caused by the small void size forces the change in configuration.

A peak value of macroscopic flow angle will be observed at that value of porosity where there exists a balance between two events. The porosity must be small enough for the shift in separation point to occur, displacing the location of the separation point to the same side of the symmetry plane. Consequently, the porosity must not be so low that the confining walls of the obstacles do not allow the change in the orientation of the vortex shedding path through the small void. The location of the peak will typically follow the location of the jump. In our simulations, the peak value of macroscopic angle occurs at $\varphi = 0.61$.

Once the peak value is attained, decreasing the porosity further will no longer increase the angle. The proximity of the adjacent walls of the solid obstacles will influence the flow in a way that decreases the macroscopic flow angle. The proximity of the obstacle walls ensues the proximity of flow features on the walls, such as the stagnation point. The stagnation point on an adjacent cylinder will reduce the effective pressure gradient in the *y*- direction, which drives the flow to increase the macroscopic flow angle. In spite of an increase of stagnation pressure with reducing porosity for the same Reynolds number, the increase is counterbalanced by a reduction in the pressure gradient resulting in a smaller macroscopic flow angle.

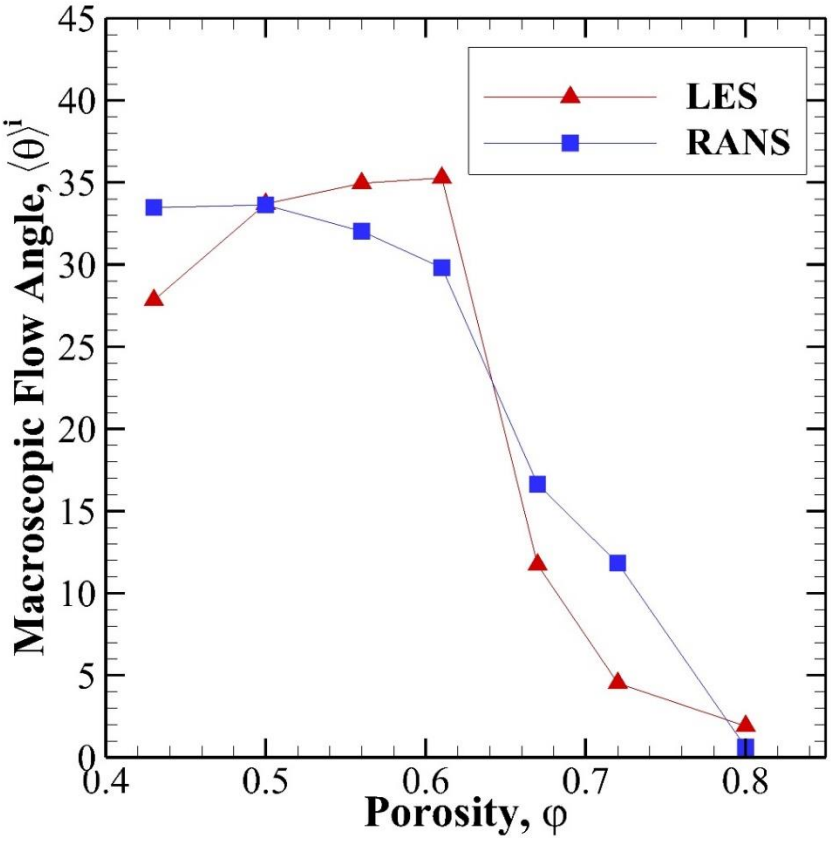

Figure 4.9: Variation of macroscopic flow angle with porosity, calculated using the LES and RANS techniques.

To validate the results from LES, RANS simulations and DNS are also performed. DNS is used for a case with $\varphi = 0.5$ at $Re_p = 1000$ to conclude that the macroscopic angle prediction with LES has an error of only 1.37% for this case. Turbulence model independence of symmetry breaking has been established using DNS, and it is important to note from the comparison of the macroscopic angle that the phenomenon of symmetry breaking is largely dependent on the large scale eddies. The RANS simulations agree very well, qualitatively, with the trend predicted by LES. The jump in macroscopic angle is predicted to be located at the same range of porosity ($0.61<\varphi<0.67$). The macroscopic angle increases exponentially at first, reaches a peak value, and then starts to decrease. The peak value of macroscopic angle occurs at a porosity of 0.5 in

RANS, rather than at 0.61 as predicted by LES. RANS also predicts a sharp increase in angle near $\varphi = 0.80$, resulting in a larger zone of sensitivity to porosity. It is observed for a porosity of 0.61 that the RANS model predicts flow separation on opposing sides of the plane of symmetry of the solid obstacles, while the vortex is formed on the same side of the symmetry plane. This is an unphysical solution since the converging nature of the void will cause the flow to reattach. This is isolated to be the cause of the discrepancy between the LES and RANS results. The errors introduced by the steady state solver, modelling errors, and the use of wall functions will contribute to a poorer solution near the wall. LES is subject to modelling errors as well. Error in LES arises from the fact that most of the scales near the wall are not resolved. A completely resolved Direct Numerical Simulation is the only method that would be able to predict the actual trend.

Influence of porosity on the location of the stagnation point

A key observation from the vortex core diameter measurements is that one of the vortex cores is larger than the other, which is a rarity for flows around circular cylinders. Intuition would lead to the conclusion that the smaller vortex is formed by the separation point that is located far downstream on the surface of the solid obstacle. However, this is not the case, and the reason behind this is investigated by analysing the characteristics of the flow on the surface of the solid obstacle.

In Figure 4.10, the location of the stagnation point is plotted against porosity. The stagnation point shows little variation with porosity signifying that it is the incident flow that decides the location of the stagnation point rather than the orientation of the vortices. For the case of high porosity, only one stagnation point is formed in the centre of the incident surface, much like the case in external flows involving circular cylinders. It should be noted that wake impingement on the adjacent solid obstacle would decide the location of the stagnation point,

rather than the incident flow in porous media flows. A symmetric mean wake pattern would not result in a shift in the stagnation point.

When the porosity decreases such that it enters the range of $0.67 \leq \varphi \leq 0.8$, flow is entrained by the vortex interaction in a single direction that causes a shift in the stagnation point. Close to the transition point to deviatory flow ($\varphi \sim 0.80$), two peaks in the pressure distribution on the wake incident surface of the solid obstacle are observed. Each peak is associated with stagnation caused by the impingement of a partially dissipated vortex. With regard to the mean flow, one peak clearly dominates the other resulting in a single stagnation point at the location of the stronger peak. In the transition region, characteristics from both regimes are observed with the deviatory flow being localized in the wake alone while the remainder of the flow remains unaffected. Given that the case with a porosity of 0.8 is close to transition, the behaviour is easily upset by small disturbances such as the numerical error associated with the discretized periodic boundary conditions. Far from the influence of the boundaries, the flow pattern is identical throughout the domain.

Past the transition region into the regime of deviatory flow, there exists a single peak in the pressure distribution on the surface of the solid obstacle since the shedding path is titled to divert the wake away from the proximal solid obstacles. Between the porosities of 0.61 and 0.67, a change in the location of the stagnation point is observed, though the change is minor. This change is brought about by the interaction of the wake with the transverse adjacent obstacle (due to separation on the same side of the symmetry plane) which pushes the stagnation point away from the region of wake dissipation. It is indeed a surprising inference that the location of the stagnation point seems to be independent of porosity in the regime of deviatory flow given that the flow mechanisms differ quite drastically.

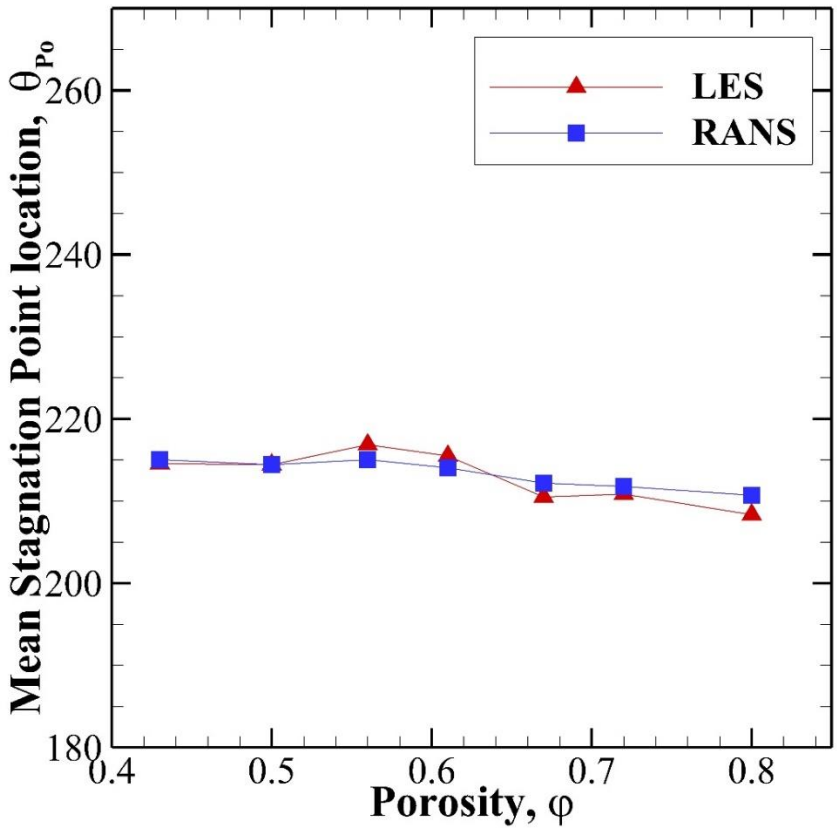

Figure 4.10: Location of the Stagnation point on the solid obstacles plotted against porosity.

Influence of porosity on flow separation

The location of the separation point is plotted in Figure 4.11 for the top and in Figure 4.12 for the bottom vortices (refer Figure 4.1 for nomenclature). The location of the separation point for the top vortex does not change significantly. It is important to note that some change is present, however, the relative magnitude of change when compared to the trend for the bottom surface is much less. This would lead to the belief that the location of the separation point at the top is merely responding to the location at the bottom and the associated size of the bottom vortex. The location of the separation point on the top surface can be seen to shift downstream when the porosity is reduced in the range of 0.67-0.8, while the normalised vortex core size decreases. In

the porosity range of 0.43-0.61, the location of the separation point shifts downstream like previously, but the normalised vortex core size increases. A discontinuity in behaviour is present in the correlation between the location of the separation points and the vortex core size between the porosities of 0.61 and 0.67. This discontinuity is visible as an upstream shift in the location of the top separation point in this range of porosity and as a jump in the vortex size.

The location of the separation point for the bottom vortex varies with porosity in a manner that is very similar to the variation of macroscopic flow angle. It is also observed that the magnitude of macroscopic flow angle is decided by the location of the separation point for the bottom vortex, forming a cause and effect relationship between the two. The other parameters, while relevant, do not directly influence the macroscopic flow angle. The location of the separation point for the bottom vortex is decided by the magnitude of the stagnation pressure (refer Figure 4.5) on the streamwise adjacent solid obstacle. The shear layer at the separation point will always advance in a direction that is tangential to the velocity at the separation point. The direction of propagation can be changed by external factors such as diffusion (momentum exchange with the mean flow) and obstruction (presence of a local pressure gradient induced by the solid walls or other eddies).

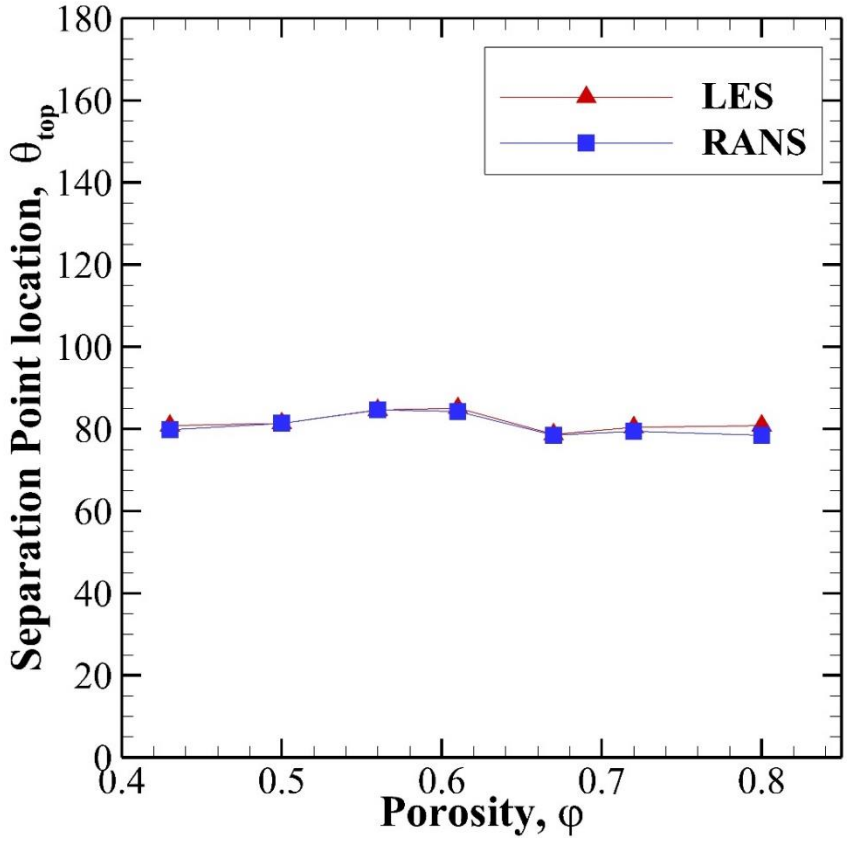

Figure 4.11: Location of the separation point that forms the top vortex on the solid obstacles versus porosity.

In the range of porosity $0.67 \leq \varphi \leq 0.80$, the location of the separation point for the bottom vortex is below the symmetry plane of the solid obstacle, progressively shifting closer to the symmetry plane as porosity is decreased. The shift in the location of the separation point is constrained by the size of the vortex and the magnitude of the stagnation pressure. The direction of propagation of the vortices is inclined from the direction of propagation of the separated shear layer at the separation point in order to circumvent the wall of the streamwise adjacent solid obstacle, with the magnitude of inclination increasing with decreasing porosity. Since it is the directional propagation of the separated shear layer that determines the amount of fluid entrained in the *y*-direction from the bulk flow, the inclination is nullified by the bulk flow once the

obstacle that is immediately adjacent has been circumvented. This results in a small macroscopic flow angle even though the direction of propagation of the wake in the streamwise adjacent void is steeply inclined (refer Figure 4.2).

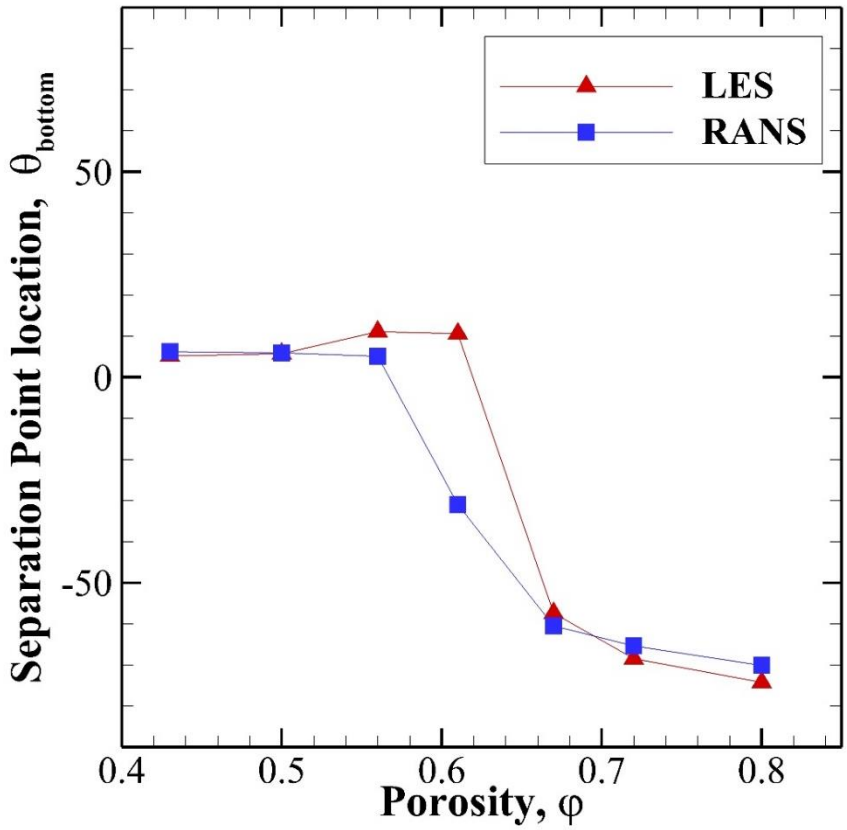

Figure 4.12: Location of the separation point that forms the bottom vortex on the solid obstacles versus porosity.

The location of the separation point for the bottom vortex shifts across the symmetry plane in between the porosities of 0.61 and 0.67. For the range of porosities, $0.43 \leq \varphi \leq 0.61$, the location of the separation point for the bottom vortex is on the same side of the symmetry plane as the top vortex, as discussed before. The path of the shed vortices deviates in a manner that causes the wake to make contact with adjacent solid obstacles in the transverse direction. In this scenario, the wake is highly oscillatory near the surface of the obstacle. The shed vortex propagates away from the separation point in a direction tangential to the velocity at that

location. This direction is not aligned with the mean flow direction. The phase difference in shedding plays a significant role in attaining the mean flow direction. The vortex that has detached from the surface is hindered by the supply of momentum from the flow separating on the other side, which slowly changes the direction of the local flow tangential to the newly shed vortex direction resulting in a correction in the direction for the mean flow. Consecutive corrections in each half shedding cycle results in a mean wake propagation direction that is in between the direction that is dictated by the separated shear layers.

In the RANS simulations, the locations of the separation points agree reasonably well with both quantitative and qualitative matching of the locations. An exception is seen in the case with a porosity of 0.61 in the location of the separation point associated with the bottom vortex. This discrepancy was discussed earlier while analysing the macroscopic flow angle. This prediction of the location of the separation point is unphysical. It is observed that the flow separates on opposite sides of the symmetry plane while the vortex is formed on the same side. While this configuration presents a transitional regime in the range of porosities, the constant addition of momentum in the converging section of the void, where the flow is seen to separate in RANS, will cause the flow to reattach. The supply of momentum is aided by the pressure gradient in the void which has the highest favourable gradient for a porosity of 0.61 amongst all the tested cases. Therefore, the flow is least likely to separate in the converging section for the porosity of 0.61. The solution is seen to be hanging between the effects of the two contrasting behaviours that are associated with these flow features, resulting in a macroscopic flow angle that is much less than what is predicted by LES.

4.3.2 Solid Obstacle Shape and Arrangement

The shape of the solid obstacles plays a critical role in determining whether the flow can remain attached for longer on its surface. We investigated cylindrical obstacles, which gradually change the behaviour of the flow from an attached to separated condition. Simulations were also performed for square cylinders, rotated square cylinders (diamond shape), and spherical obstacles. The use of square cylinders and diamond shaped cylinders did not yield deviatory flow for values of porosity where it is expected to occur. The reason behind this is that both square cylinders and diamond shaped cylinders possess sharp corners that force the flow to separate at that location. In the case of square cylinders, the converging diverging section that is necessary to accelerate the flow is absent as well. In the case of spherical obstacles, the macroscopic flow angle is present. The use of spherical obstacles yields a flow field that deviates from the principal direction resulting in a three dimensional flow angle. The deviation is seen in 3 different arrangements of the solid obstacles – in-line, horizontally and vertically staggered. However, the staggered arrangements have a lower magnitude of macroscopic flow angle when compared to the in-line arrangement. A change in the obstacle arrangement would alter the path of the vortex wake, and even the vortex structure in the case of vertical staggering.

Influence of solid obstacle shape on the macroscopic flow

While the shape of the solid obstacle is not a parameter in the determination of macroscopic flow angle, it introduces a necessary criterion for its occurrence. The deviatory flow is expected to occur only for certain solid obstacle shapes like the circular cylinder, while other shapes are subject to a change in the flow physics that restricts the symmetry breaking phenomenon. The governing factor of the shape of the solid obstacles that allows symmetry breaking is the pressure gradient that it imposes on the incoming flow. It is established in the previous sections that symmetry breaking is a feature of porous media with low porosity. At low porosity, there exists a

mutual exchange of energy between the flow and the obstacle voids. While it is the flow that determines the pressure exerted on the walls of the solid obstacles, the shape of the solid obstacles will determine the distribution of pressure. In high porosity, the influence of the pressure distribution on the solid obstacle wall on the bulk flow is insignificant. As the porosity is reduced, the influence becomes substantial enough to alter the bulk flow behaviour. Therefore, at low porosity, the bulk flow is strongly dependent on the pressure distribution on the wall of the solid obstacle.

In an attempt to replicate the asymmetric flow pattern with other solid obstacle geometries, both two and three dimensional GPMs were used as listed in Table 4.3. When square cylinders were used to form the 2D GPM, the deviatory flow did not appear. The 2D mean flow streamlines for this geometry are plotted in Figure 4.13. The mean flow streamlines indicate that the flow pattern is symmetric. Two large recirculating vortices are formed in the streamwise adjacent void. The flow separates at the sharp vertex of the square shaped geometry. The large magnitude of stagnation pressure and the favourable pressure gradient distribution are very important factors that promote symmetry breaking. In this square geometry, a converging-diverging section is not present to allow the formation of a favourable pressure gradient through geometry alone. A favourable pressure gradient can be induced through asymmetry in the stagnation pressure. However, the locations of the stagnation points in this geometry are fixed by the geometry at the locations of the sharp vertices, which observe perfect symmetry.

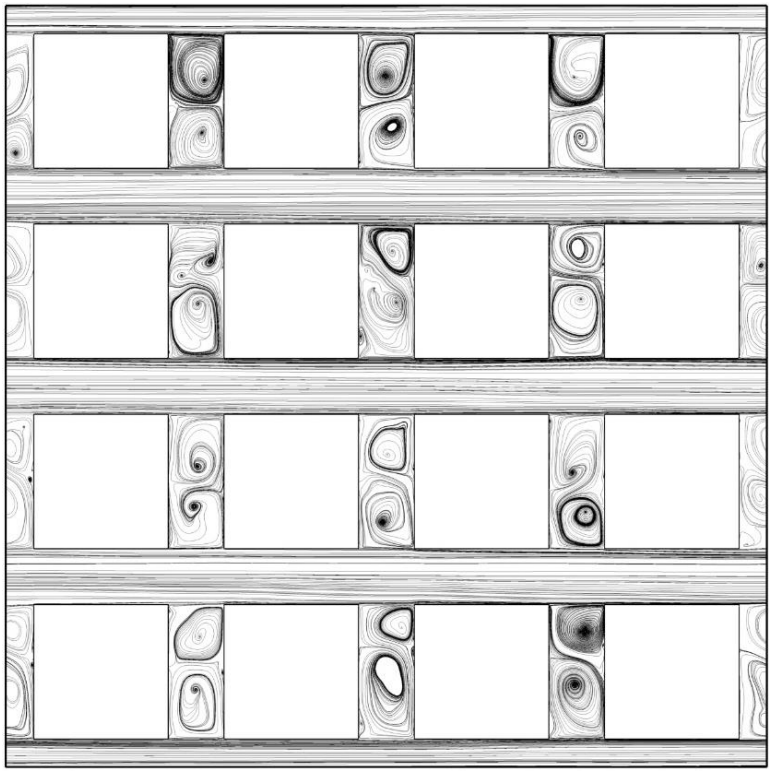

Figure 4.13: 2D mean flow streamlines at the midplane for Case 15 – with square GPM obstacles

The flow patterns in Case 15 contain zones of strong recirculation. The bulk flow enters the streamwise voids only through the vortex formation process. If the porosity is increased such that the size of the void is equal to the size of the obstacle (Case 16), fluid would enter the void from outside the envelop of the vortex. Theoretically, as the size of the solid obstacle reduces to zero (porosity increases to 1), the solid obstacle shape would cease to influence the flow pattern. This was another objective of reducing the diameter of the solid obstacle, to induce similarity between circular and square shaped obstacles. However, it should be noted that the reduction of the obstacle size beyond a certain critical value would diminish the possibility of symmetry breaking. It was observed that the flow pattern for Case 16 was symmetric as well, indicating that it is unlikely that symmetry breaking would occur for a square cylinder solid obstacle geometry.

To introduce a converging-diverging section in the square cylinder geometry, the orientation of the obstacles with respect to the principal direction is rotated by a 45^{o} angle. This operation is performed for Case 16. As seen in Figure 4.14, the presence of a converging-diverging section does not induce symmetry breaking in this case. Two important features of this flow lend an explanation to the absence of symmetry breaking. The size of the vortex is much larger than the size of the throat section. A phase difference in shedding is present in this flow. When the shedding of a new vortex at the top vertex breaks down the existing vortex, some fluid is entrained to the other side. However, this momentum is not sufficient to shift the direction of the flow entirely. Inadequacy in momentum is a consequence of the mandatory flow separation at the vertex of the geometry, and the separation point cannot shift past the vertex. The ability of the separation point to shift downstream is a requirement to sustain the deviatory flow that is not satisfied by the square cylinder geometry due to the presence of sharp vertices.

To be able to quantify these inferences to make reliable predictions for the macroscopic models, the circularity (sphericity for 3D GPMs) of the geometry should be analysed with regard to its influence on the macroscopic quantities and the symmetry breaking phenomenon. In this document, criteria have been established for the occurrence of symmetry breaking based on the curvature of the geometry. The geometry of the solid obstacle must possess a smooth curvature such that the associated pressure distribution on the wall of the obstacle is first and second order continuous. Second order continuous is an important criterion that ensures that an abrupt change in pressure gradient does not occur, which would cause the flow to separate at the location of the abrupt change. In the case of square cylinder obstacles, the vertex forms an abrupt change in the pressure gradient distribution causing flow separation. When the obstacles are rotated by 45^{o}, the pressure gradient is discontinuous with a low magnitude of discontinuity (compared to the case

without rotation) at the top and bottom vertices resulting in flow separation at that location. Future work must address whether piecewise continuity in pressure gradient distribution is sufficient to allow the separation point to shift as long as the magnitude of discontinuity is small.

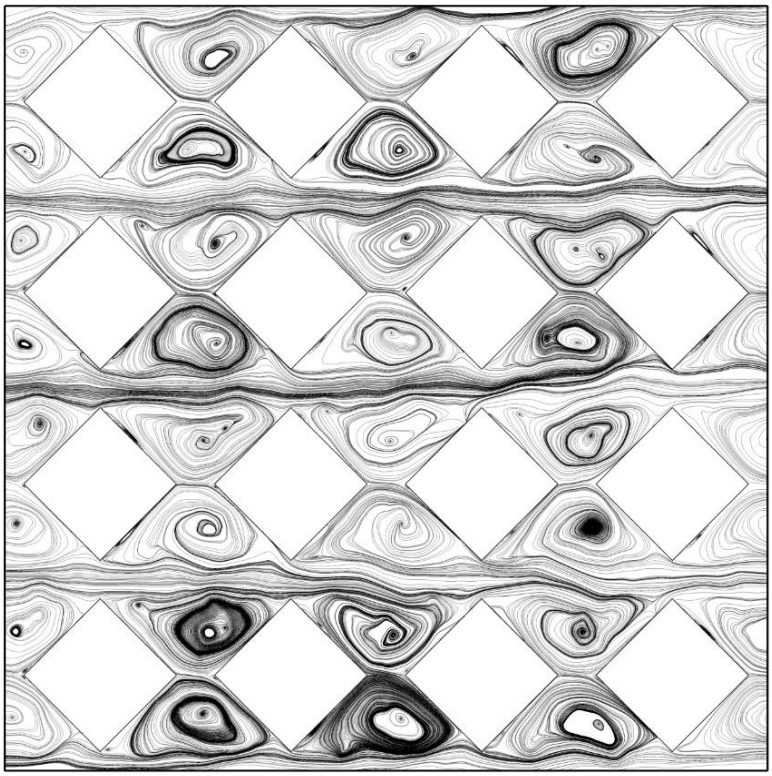

Figure 4.14: 2D instantaneous fully developed flow streamlines at the midplane for Case 16 with 45o rotation in obstacle orientation.

3D GPMs are also tested to verify the occurrence of symmetry breaking. Since circularity of geometry is an important criterion for symmetry breaking, spherical solid obstacles are chosen to form the solid matrix. The porosity of the medium is chosen such that symmetry breaking would be expected (based on the predictions from 2D GPMs) while taking care to ensure that the small gap that is associated with this geometry does not invalidate the numerical model. 3D GPMs are not explored in detail since the computational expense of these simulations is very high. Simulations are performed to only address the possibility of occurrence of symmetry breaking. It is observed that symmetry breaking is present in 3D GPMs as well. Symmetry

breaking occurs in two directions forming a 3D macroscopic angle with respect to the principal direction. It would appear that the two dimensionality of the cylinder geometry in 2D GPMs was suppressing symmetry breakdown in the third direction. Another feature of 3D GPMs is that the flow separation process is three dimensional. In 2D GPMs, the location of the separation point was the same at planes in the third direction. The vortices appearing in the mean flow are two dimensional as well for 2D GPMs. Simulations with 3D GPMs introduces an additional level of complexity pertaining to three dimensionality of the flow features. The 2D mean flow streamlines are plotted in Figure 4.15. Since the features are three dimensional, the 3D mean flow streamlines are also plotted in Figure 4.16.

The 2D streamlines are not indicative of all the flow features for 3D GPMs. They are useful in illustrating that the flow is inclined at that plane. This inclination is also observed in the 3D streamlines in Figure 4.16(A). However, it is apparent that the flow pattern in 2D is not an accurate depiction of the three dimensional flow features, especially since only one vortex is visible in this visualization. The most obvious deduction that is made from the 3D streamlines is that this is a two vortex system (see Figure 4.16(B)). The vortices are tilted away from the principal direction in both polar and azimuthal directions with respect to the centre of the spherical obstacle. The vortices can also be seen to propagate in opposing directions away from the surface of the obstacle. The proximity of the adjacent obstacle is responsible for the propagation of the vortex such that it is against the direction of the macroscopic velocity. This feature is in contrast to 2D GPMs where the vortices are propagated in the same direction. Simulations with other porosities and close investigation of the dynamics of the flow is necessary to understand this flow better.

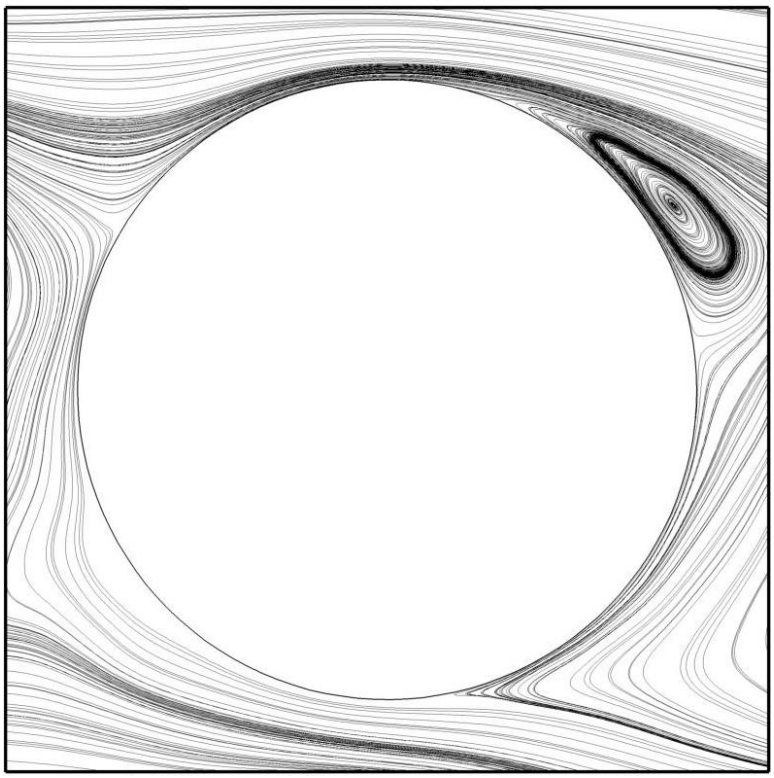

Figure 4.15: 2D mean flow streamlines for Case 17 at the midplane of the spherical obstacles.

The effect of obstacle shape on the dynamics of vortex shedding

A contrasting behaviour is observed in the mechanism of vortex dynamics and vortex dissipation between the deviatory flow in circular cylinders to the other cases where deviation is not observed. The vortex dynamics plays a crucial role in determining whether or not the inclination will appear, and vice-versa. In the case of the circular cylinder obstacles, it is observed that the vortices that are formed at the rear of the obstacle detach themselves from the surface of the cylinder to be carried away into the stream by the bulk momentum. The shed vortices are then

dissipated in the mean flow by shear. The vortex dissipation process is not complete until the vortex interacts with the surface of the adjacent cylinder.

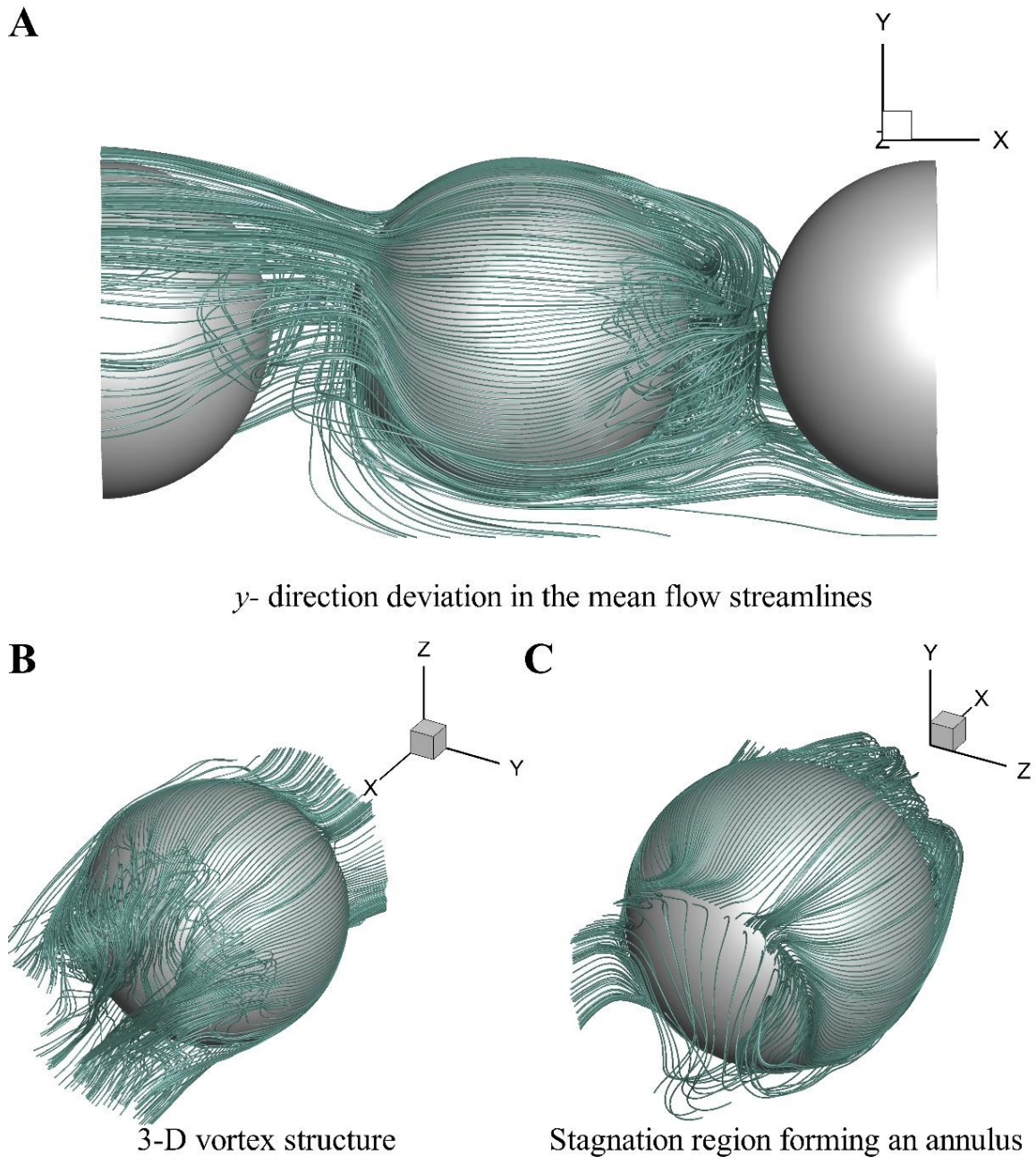

Figure 4.16: 3D mean flow streamlines for Case 17 describing the features of deviatory flow for spherical obstacles. Momentum source is applied in the *x*- direction.

For high porosity, the vortex is dissipated in the transverse adjacent void in the presence of a local adverse pressure gradient. For low porosity, the vortex impinges on the diagonally adjacent cylinder as a consequence of the steeply inclined nature of the flow, where it is dissipated by the shear in the boundary layer.

In the case of the square cylinder, the vortices that are formed are stationed in the rear of the cylinder throughout their existence. This results in a recirculation zone in the rear of the cylinder, quite like the flow in a lid driven cavity. The proximity of the adjacent cylinder "traps" the vortex in the gap between the two cylinders due to the presence of a large stagnation pressure at the vertices of the square geometry. The flow in the transverse adjacent void proceeds to bypass the streamwise adjacent void over the recirculation zones stemming the possibility of a new vortex to be generated. The flow in the transverse adjacent void behaves like a channel flow, carrying the bulk of the momentum with it. As a result, the time scale of the vortex formation and dissipation cycle is much smaller than the time scale of the channel-like flow. The channelling effect and the fixed location of the vortex in the streamwise adjacent void are together responsible for a smaller applied pressure, g_x, in the case of the square cylinder when compared to the circular cylinder for the same value of porosity (refer Table 4.3). At low porosity, symmetry in flow pattern leads to a reduction in pressure drag as the pressure force that is applied on the front and rear surface of the obstacle cancel out, thereby reducing the requirement for applied pressure gradient to maintain the flow rate.

The fluid in the vortex that is located in between the obstacles cannot continue to recirculate forever. As the vortex loses energy, a new vortex that is generated on the opposite side slowly displaces the older vortex in a manner that pushes the older vortex out of the gap. The older vortex cannot still enter the transverse adjacent void due to the large momentum that is

carried by the channel-like flow. As a result, the older vortex is continually dissipated in the shear layer in the form of a Kelvin-Helmholtz instability while being pushed towards it. The Kelvin Helmholtz instability is visible in the instantaneous streamline plots shown in Figure 4.14.

The scenarios investigated here do not represent the behaviour of the flow for the entire range of parameters for the shape of the obstacle, as it is a consequence of the surface pressure distribution (has a strong dependence to the length and velocity scales). The vortices may make their way out of the streamwise adjacent void in the case of square cylinders for a higher porosity where the void size is much larger than the obstacle size. In the case of the circular cylinder, the vortex shedding mechanism is not only dependent on the porosity, but also on the Reynolds number of flow. The detached vortex mechanism will cease to exist when the Reynolds number is reduced sufficiently such that the flow separates much earlier leading to the formation of large zones of recirculation. However, this is unlikely in the classes of flows that are considered turbulent unless the flow is tripped by some artificial manner (for example, the placement of a notch in the obstacle geometry in the diverging section of the void). Extremely low porosity may also result in early separation of flow leading to large recirculation zones. Therefore, the dynamics of vortices cannot be generalized by shape alone, since there are several other factors that have to be taken into consideration.

Influence of solid obstacle arrangement on the macroscopic flow

The use of an in-line solid obstacle arrangement to form the GPM ensures that the wake behind each solid obstacle is in perfect harmony. In-line arrangement also ensures that the net force that arises from asymmetric pressure distribution on each obstacle surface is aligned. A question arises as to whether the phenomenon of symmetry breaking would appear if the solid obstacles are arranged in a different manner. It is possible to use a staggered arrangement with relative

ease to simulate flow in low porosity conditions using an REV-T of the same size. It should be noted at this stage that the phenomenon of symmetry breaking is inherent at these Reynolds numbers for circular solid obstacles. The close spacing between the obstacles in porous media with low porosity would be present regardless of the arrangement. However, since the obstacles are not aligned, symmetry breaking may not amplify sufficiently to affect the macroscopic flow. To simulate the possibility of zero amplification, two cases were simulated where the rows and the columns of the GPM were staggered by a distance equal to half the pore size (0.5s), such that the wake behind the obstacles are out of phase by the maximum possible distance. The RANS turbulence model is used for this simulation to reduce computational expense.

The mean flow streamlines are plot for both types of staggered arrangements in Figure 4.17. It can be observed that the macroscopic flow angle is present for both cases, in spite of the misalignment in the wake. The magnitude of macroscopic flow angle is lesser in the case of both staggered arrangements when compared to the in-line alignment. A different vortex system is also observed in the case of vertical staggering, that resembles the vortex system from a higher porosity (similar to $\varphi = 0.72$). The vortex system is identical to the in-line arrangement in the case of horizontal staggering.

Two parameters control the macroscopic flow angle in the present cases with staggered arrangements - the proximity of the obstacle walls and the tortuosity of the wake path. It can be observed that the vortex core size and the separation point location are identical in the case of in-line and horizontal staggered arrangements. This is a result of the two arrangements possessing the same wall to wall distance between the obstacles in the principal direction. However, the macroscopic flow angle is smaller in the case of the horizontally staggered arrangement due to the tortuosity of the wake path. The wake exits the streamwise adjacent void, circumvents the

closest transversely adjacent obstacle and terminates on an obstacle that is more than one GPM unit cell dimension away from the generation point. The longer path taken by the wake weakens it and reduces the magnitude of the stagnation pressure upon impingement. Hence, a separation bubble is formed on the surface of the obstacle when the separation point shifts, similar to the separation bubble seen in low Reynolds numbers (refer Section 4.3.3).

In the case of vertically staggered arrangement, the obstacle wall proximity is altered when the streamwise adjacent obstacle is moved. The void that is adjacent in the principal direction is larger than in the other two cases. This results in a change in the size of the vortices, along with a change in the macroscopic flow angle that now resembles a case with higher porosity. A simulation of the dynamics of the vortex system is necessary to comment more on this case.

A change in the obstacle arrangement can severely alter the macroscopic behavior of the flow. Since random arrangements are a frequent occurrence in nature, it is important to parametrize this behavior. Two key parameters that affect symmetry breaking in these cases are the dispersion of obstacles in the streamwise direction and the tortuosity of the path of the flow. The sensitivity of the dispersion of the solid obstacles suggests that a similar effect would be present with oblong solid obstacles in in-line arrangements as well.

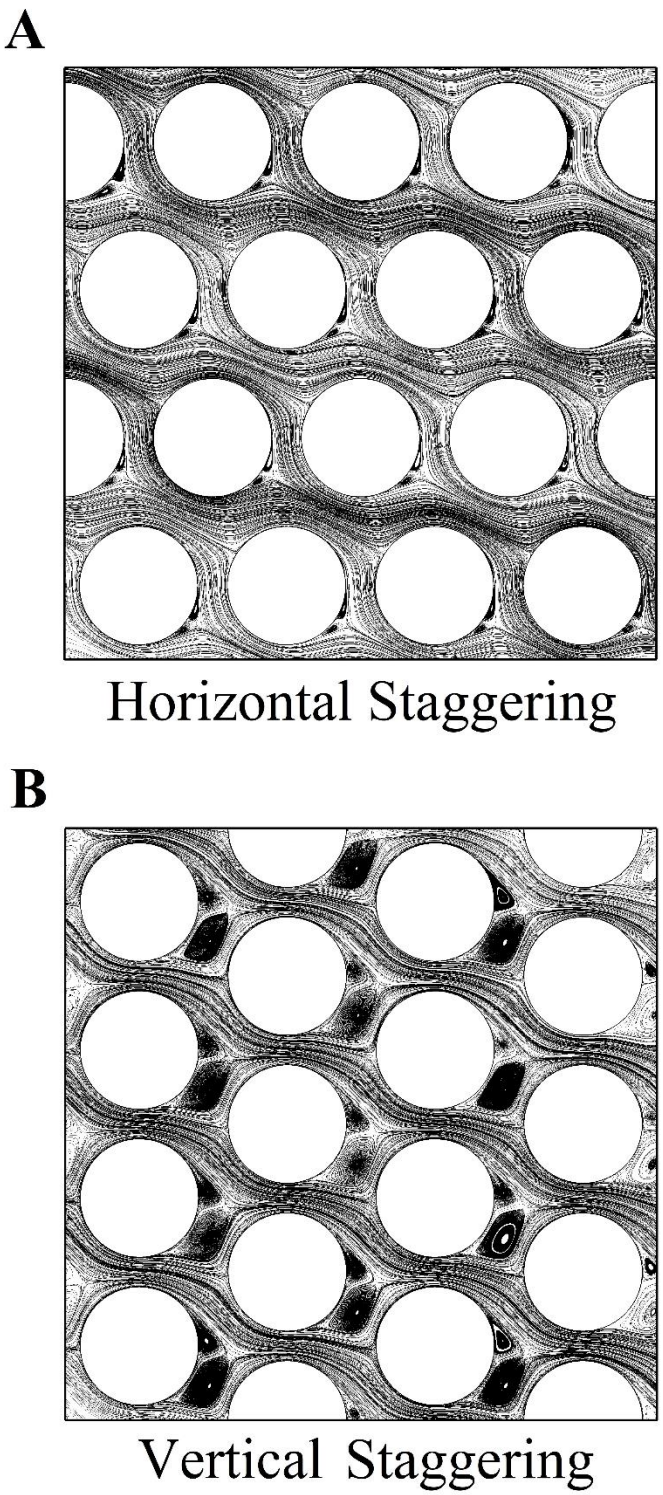

Figure 4.17: 2D mean flow streamlines at the midplane for different obstacle arrangements; φ = 0.5, Re_p = 10,000 – (A) horizontally staggered arrangement ($\langle\theta\rangle^i = 21.4^o$), (B) vertically staggered arrangement ($\langle\theta\rangle^i = 15.9^o$).

Surface Roughness

Surface roughness affects the boundary layer on the wall of the solid obstacle for fully turbulent flows by causing the boundary layer to lose momentum at a larger rate. Since the macroscopic flow angle is determined by the location of the separation point, a change in the boundary layer may drastically affect the macroscopic flow angle. To investigate the influence of surface roughness, a RANS turbulence model with a log-law rough wall function was used to simulate the flow. For a hydrodynamically smooth surface finish, disparity exists in the macroscopic flow angle between the log-law wall function and a more accurate two layer TKE wall model. The magnitude of the macroscopic flow angle for the log-law wall function can be assessed with qualitative value only. The macroscopic flow angle decreases as the surface roughness parameter, equivalent sand grain roughness (K_s^+), increases (refer Table 4.7). The change in macroscopic flow angle with surface roughness is a manifestation of the change in the location of the flow separation point.

Table 4.7: RANS simulation cases[1] for circular cylindrical obstacles illustrating the influence of surface roughness of the solid obstacles on the macroscopic flow angle for $\varphi = 0.5$

Case ID	Roughness boundary layer regime	Equivalent Sand Grain Surface Roughness, K_s^+	Macroscopic Flow angle, $\langle\theta\rangle^i$	Pore Scale Reynolds number, Re_p
24	Laminar	1.56	30.93	23,624
25	Transitional	7.97	29.06	24,112
26	Turbulent	98.4	8.63	24,887

[1] The author wishes to acknowledge the contribution of Timothy S. Su towards providing data for the simulations involving surface roughness.

4.3.3 Reynolds Number

The simulations that are presented in this work are performed for a Pore Scale Reynolds number (Re_p) of 10,000. This is identified to be far enough from the effect of transition. Simulations were also performed at lower Reynolds numbers in order to verify the occurrence of symmetry breaking in the absence of a large momentum reservoir. Below the Reynolds number of 300, the flow patterns are symmetric with large recirculating vortices. Between a Reynolds number of 300 and 500, the macroscopic flow angle jumps from zero to a constant value. Further investigation has led to the conclusion that the microscopic flow field experiences a gradual change with the separation bubble in the shifting stage preserved until a Reynolds number is reached where the availability of momentum is able to counter the adverse pressure gradient in the separation bubble region, allowing the flow to remain attached in that region. It is only the macroscopic flow field that experiences a sudden jump.

Influence of the Reynolds number on the macroscopic flow

The availability of adequate momentum, which drives the amplification of the von Karman instability, is an important factor for symmetry breaking. In order to investigate whether the phenomenon is limited to the turbulent flow regime, simulations are performed for the 2D GPM with low porosity by varying the Reynolds number of the flow from the creeping flow regime to the beginning of the fully turbulent flow regime. Only three cases are documented in this work representing distinct flow behaviour. In the case of creeping flow (Re_p = 0.1) around a single cylinder, the flow remains attached throughout the surface of the cylinder. In porous media with low porosity, flow separation occurs with a pair of attached vortices formed in the streamwise adjacent void (see Figure 4.18). An attached vortex system cannot induce symmetry breaking because of its inability to breakdown and dissipate away from the separation point. This implies

that the Reynolds number at which a detached vortex system is first formed would mark the beginning of symmetry breaking regime.

This behaviour is consistent throughout the laminar regime and well into the laminar-turbulent transition regime as well. As the Reynolds number is increased, the location of the separation point shifts upstream and the attached vortices grow bigger in size as a result of the change in separation point. It is observed that the vortex system changes from an attached to detached configuration in the Reynolds number range of 300-500. A consequence of a detached vortex system is symmetry breakdown. The detached vortex system also marks the incidence of the von Karman instability. The presence of the von Karman instability is a necessary condition for symmetry breaking, as well as the presence of a detached vortex system. Both of these features are essential for the uneven breakdown of vortices.

An observation at Re_p = 500 is that a separation bubble exists (refer Figure 4.19) on one side of the cylindrical surface. The location of the separation point shifts upstream first as the Reynolds number increases, and then starts to shift downstream once turbulence starts to affect the flow field. Turbulent boundary layers are prone to enhanced fluid mixing that allows the flow to stay attached for a greater distance from the stagnation point. At Re_p = 500, the separation point is located on opposing sides of the obstacle symmetry plane and yet, deviatory flow is observed. Flow entrainment after the vortex breakdown stage supplies adequate momentum to the boundary layer flow to reattach to the same surface at a more downstream location and proceed to separate on the same side of the symmetry plane. As a result, flow separation occurs twice for the boundary layer on one side with the appearance of a separation bubble to cope with the *y*-momentum supplied by flow entrainment despite the unavailability of momentum in the boundary layer to overcome the viscous shear.

At a Reynolds number of 3,000, the separation bubble vanishes when the location of the separation point is naturally pushed downstream. As the Reynolds number increases, the size of the separation bubble is expected to slowly diminish as the location of the separation point shifts downstream. Measurement of the macroscopic flow angle reveals that the flow angle is the same with and without the separation bubble, indicating that there exists a discontinuity in the macroscopic flow angle at the point where the vortex system changes from an attached to a detached configuration. The physical process that results in the change is gradual, when the microscopic von Karman instability derives momentum from the bulk flow, subject to availability, towards its amplification. Instabilities in the flow introduced by the unsteady and non-linear nature of the flow field will be damped at lower Reynolds numbers. The ability of the flow to damp the instabilities will diminish as the Reynolds number increases as the instabilities derive energy from the inertia of the flow. At a critical value of Reynolds number, the instabilities start to amplify resulting in a detached vortex system with a phase difference in vortex shedding, which in turn results in deviatory flow.

Discontinuity is present in the mean field variables at steady state since the signature of the initial transient is not present. Rather, the agglomeration of effects that develop in the initial transient stage contributes to the flow field at steady state. To recover information about the transition of flow from symmetric to deviatory with regard to change in the Reynolds number, the initial transient stage must be analyzed in detail. Transition to fully turbulent flow is expected to occur in the Reynolds number range of 100-200. However, transition in the vortex system occurs only in the Reynolds number range of 300-500. In external flows, transition in the vortex system precedes the transition to turbulence. This character of porous media flows must be verified by determining the critical Reynolds number for this geometry.

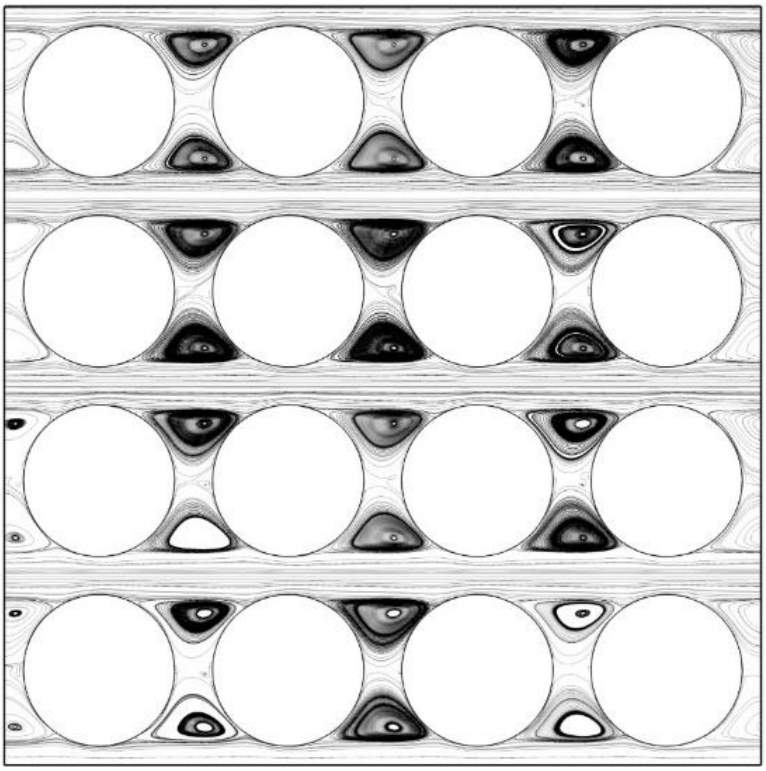

Figure 4.18: 2D mean flow streamlines at the midplane for symmetric flow at Re_p = 100 (Case 18).

To investigate whether this behaviour is repeatable, the simulations are also performed for a porosity of 0.72. The results of this simulation are not documented here. Transition from an attached to a detached vortex system and transition from symmetric to deviatory flow is observed in the Reynolds number range of 300-500. This observation provides confidence in the hypothesis that it is the transition from an attached to detached vortex system that causes symmetry breaking and that it is governed by the availability of momentum in the boundary layer. A separation bubble is not observed in the case of $\varphi = 0.72$ since the flow separates on opposite sides of the symmetry plane. The *y*- momentum is not sufficient to permit reattachment of the boundary layer.

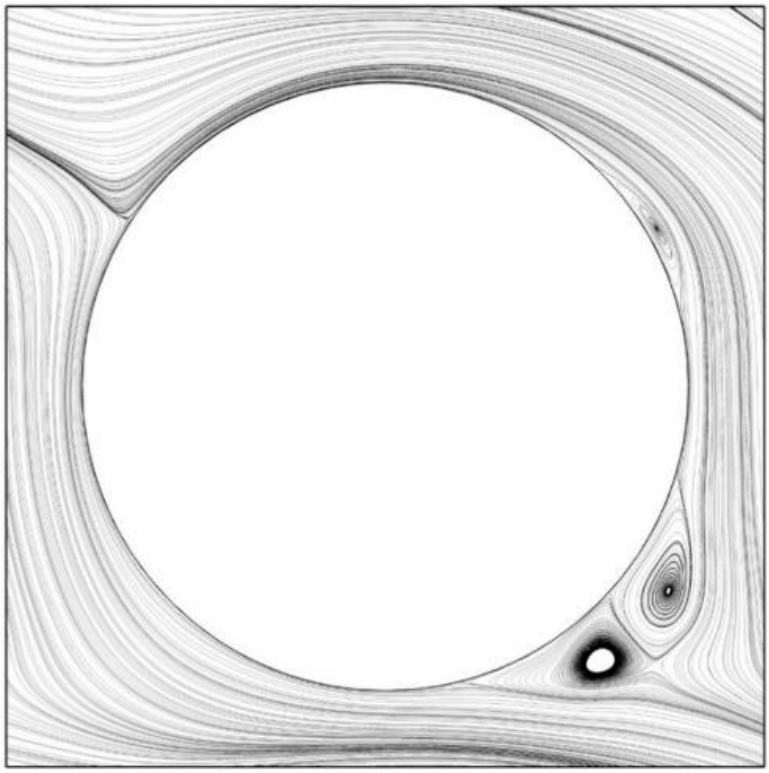

Figure 4.19: 2D mean flow streamlines at the midplane for deviatory flow with a separation bubble at Re_p = 500 (Case 19).

4.4 3-D Flow Visualization with the Q- Method

Coherent turbulent flow structures are examined by visualizing the iso-surfaces of Q-Criterion for the instantaneous flow field for circular and square cylinder obstacles. Q-Criterion is defined as the second invariant of the velocity gradient tensor. A turbulent structure is defined by a connected zone of fluid that possesses the same positive value of Q-Criterion, which represents the dominance of vorticity over strain rate in that zone. Visualizing the structures of turbulence in this manner have highlighted some aspects of flow that are unique to the shape of the obstacles. The Q-Method visualizations are provided in Figure 4.20 and Figure 4.21. The

coherent turbulent structures are extracted by plotting the iso-surfaces of normalised Q-Criterion at a value of $Q/Q_{max} = 10^{-3}$, with contours of mean *x*- velocity displayed on the iso-surfaces.

The effect of porosity is examined in Figure 4.20 for the case of circular cylinder obstacles. The shear layer on the surface of the cylinder and the process of separation is observed to be two dimensional, which is visible as sheets of high vorticity regions wrapped on the surface until flow separation. After separation, "rolls" of fluid are shed which are also two dimensional at the point of generation. As these "rolls" move away from the surface, they begin to distort in the z-direction. The distorted vortex elements interact with one other and coalesce in the wake to form tubular structures that span in the streamwise direction (the span direction changes from normal to streamwise). The coherent structures that enter the transverse adjacent void are all tubular in shape, stressing the importance of capturing the three dimensional aspects of flow for the two dimensional geometry.

The distinction between the turbulent structures for different porosities is highlighted in the manner in which the flow separates and the direction of propagation of the structures. For the porosity range of $0.72 \leq \varphi \leq 0.80$, the spacing between the obstacles is sufficiently large. However, the structures that enter the bulk flow have a preferential direction. It can be seen in Figure 4.20. for $\varphi = 0.72$ that a majority of turbulent structures are exiting the gap between the cylinders from the bottom of the cylinder. The structures that originate from the separation shear layer at the bottom are visibly larger. The inclination of flow (observed in the streamline plots in Figure 4.2) results in the path curvature of these larger structures by bringing the structures to the

top side. This results in the clustering of structures in the transverse adjacent void behind each obstacle (in the converging-diverging section).

For the porosity range of $0.43 \leq \varphi \leq 0.61$, even though the flow separates on the same side of the obstacle symmetry plane for shear layers from the top and bottom surfaces, the rolls in the separation shear layer are observed upstream of where the flow separates. These rolls are indicative of impending separation, meaning that there must exist some degree of instability upstream of the separation point. However, the flow manages to stay attached under the influence of the favourable pressure gradient in the converging section while remaining at the brink of separation. For $\varphi = 0.50$, the effect of confinement due to closely placed obstacles is apparent in the form of vortex stretching. The streamwise tubular structures are formed with a nearly circular cross-section. At the throat of the converging-diverging section in the transverse adjacent void, the structures can be seen to stretch in the z-direction. The confining space "flattens" the vortex structure at that location as a result of the geometry and the clustering of many structures in that region.

For square cylinder obstacles, the flow is comprised of two distinct regions – a channel-like region and a recirculation region (see Figure 4.21). The two regions are clearly visible as they are demarcated by coloured contours of *x*-velocity. The recirculation zones possess very low velocity, coloured in blue, and the channel-like zones possess very high velocity in comparison, coloured in red. At this instant of the flow, the vortex formation is at half cycle, implying that there exists a vortex on each side of the obstacle symmetry plane. At this instant, the influence of the vortex dissipation by shear is not visible. The dissipation of vortices results in a net reduction in the velocity magnitude in the channel-like flow that is clearly visible at the end of the

dissipation cycle. The drop in velocity magnitude is present in alternate voids, while the velocity magnitude in the voids that do not encounter vortex dissipation in that cycle remains unchanged.

A strong gradient is present in the *x*-velocity at the interface between the recirculating vortex and the channel-like flow. This strong layer of shear is prone to the formation of Kelvin-Helmholtz instabilities that ultimately dissipate the recirculating vortices. Since the recirculating vortices do not enter the channel-like region, the turbulent structures that are present in the channel-like region are generated by the influence of the wall of the solid obstacle. The turbulent structures in the channel-like flow bear a resemblance to the hairpin vortex structures that are observed in a typical channel flow. The ability to abstract parts of the porous media flow by simpler, well-known flow scenarios provides strength in understanding and modelling the phenomena in the macroscale.

When the obstacle orientation is changed for the case of square cylinder obstacles, the flow pattern changes with the preservation of its basic elements. Strong recirculation zones are present that possess a much larger time scale. A channel-like flow is still present that is more clearly visible in the streamline plot in Figure 4.14. The channel-like flow region is narrower in this case, possessing a greater degree of instability as a result of a larger zone of interaction between the recirculating vortex and the channel. The size of the recirculation zone in this case is also much larger than when the obstacles were oriented at 0^o. As a result, a stronger gradient in momentum is observed between the recirculating vortices and the channel-like flow. The hairpin shaped turbulent structures of channel flow are absent in this flow since the channel-like flow does not encounter any solid walls.

The turbulent structures in the channel-like flow are similar to that of free-shear flows with large structures concentrated at the interface of high momentum gradient. The absence of strong

bounds for the recirculating vortices provides greater degree of freedom for the vortex to influence the bulk flow.

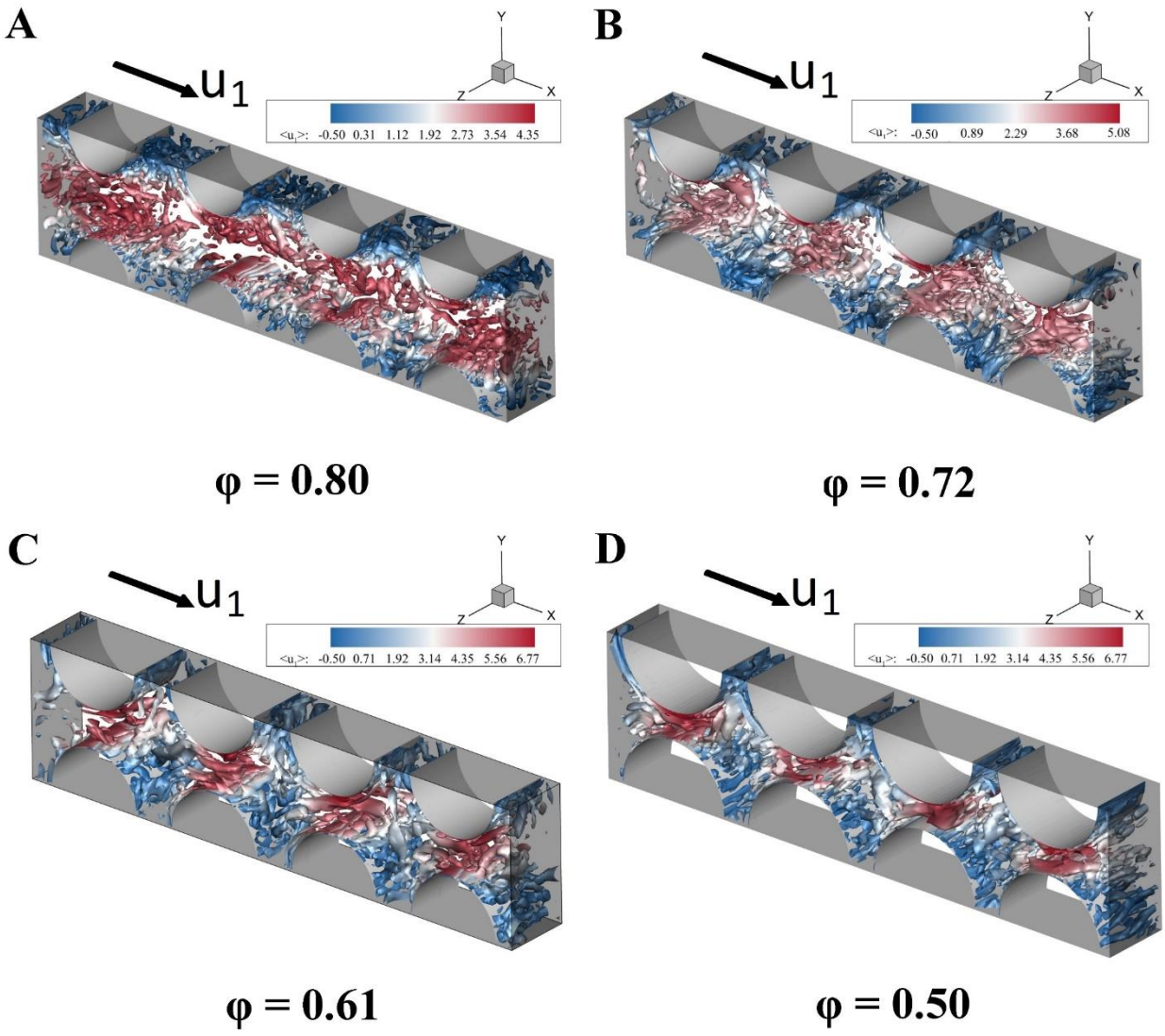

Figure 4.20: Coherent Turbulent Structure visualisation using the Q- method for circular cylindrical GPM obstacles for different porosities (A-D).

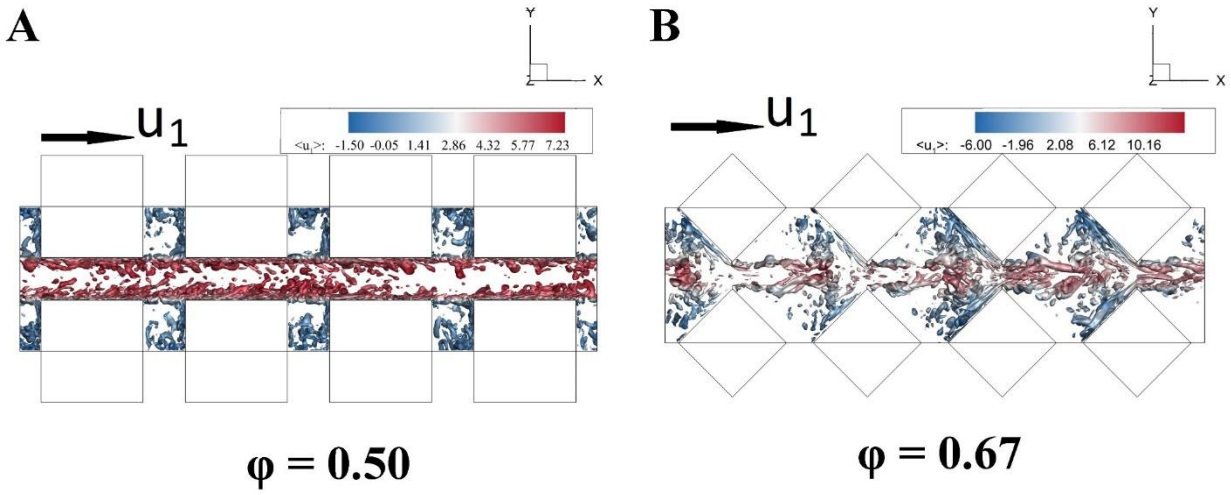

Figure 4.21: Coherent Turbulent Structure visualisation using the Q- method for square cylindrical GPM obstacles for different obstacle orientations – (A) 0^o rotation, (B) 45^o rotation.

5. CONCLUSIONS AND SCOPE FOR FUTURE WORK

5.1 Conclusions

Numerical simulations indicate that occurrence of the von Karman instability in homogeneous porous media results in symmetry-breaking macroscopic flow that causes an angular deviation of the flow from the principle direction along which the pressure force is applied. The simulations are performed for a homogeneous porous medium that would warrant symmetric flow by definition. The imbalances in the flow that are inherent in the von Karman instability are amplified and sustained with the help of the confining geometry in porous media with low porosity. The deviation originates from the phase difference in vortex shedding and the corresponding imbalances are sustained by a shift in the stagnation point while being aided by a favourable pressure gradient in the geometry. At present, the deviation is observed for a specific arrangement of porous obstacles, the cubic/in-line arrangement. This flow behaviour would not be seen in a staggered arrangement, where the geometry ensures that the streamwise adjacent obstacles are far apart such that the stagnation pressure does not have an impact on the separation point.

Several governing parameters that affect the occurrence of the deviatory flow are identified – Porosity, Porous Obstacle Shape, and Reynolds number. Porosity is one of the fundamental governing parameters that decides the appearance of deviation. It is observed that the macroscopic flow angle is more pronounced for lower porosities. However, the macroscopic angle decreases once a critical value of porosity is reached. The circularity (2-D) or sphericity (3-D) of the porous obstacles is an essential parameter for this phenomenon, due to the reliance of the flow on the geometry to remain attached in regions of adverse pressure gradient. The Reynolds number of the flow must be in the regime of fully turbulent flow in order for the flow

to possess sufficient momentum to withstand the deviation. The effect of surface roughness on the obstacle walls was also investigated in this work by using a RANS turbulence model that simulates surface roughness by using a wall function. Surface roughness will force the flow to separate early and influences the macroscopic flow through a reduction in the angular deviation. There is a wealth of information that is left to be extracted; this must be addressed by future work.

5.2 Scope for Future Work

The present work is only a first step in understanding this phenomenon and there exists plenty of scope for future work. Some of the unanswered questions in this work are mentioned below:

- The possibility of occurrence of this symmetry breaking phenomenon in real life scenarios when subjected to finite boundaries. At present, an infinitely periodic domain is used. Examples of finite or semi-infinite domains where symmetry breaking may play a significant role are – external flow around a porous obstacle, composite porous/fluid ducts. Precursor simulations have been performed for these domains where enhanced mixing at the interface is observed for the composite duct, and the wake width diminishes in size for the external flow around a porous obstacle when symmetry-breaking occurs. However, the numerical accuracy of these simulations are still questionable.

- Characterizing the influence of roughness of the surface of the porous obstacles. Smooth surfaces are a very rare occurrence in nature. The present work makes use of wall roughness functions that use the log-law assumption to simulate wall roughness. These functions may not be accurate in this context as they were developed for channel flows. Geometric roughness is an important parameter that allows the extension of this

work to realistic obstacle geometries. Geometric roughness may be simulated using sinusoidal and square wave grooves cut into the surface of the obstacles. Initial work has shown that geometric roughness plays an important role in controlling the symmetry-breaking phenomenon.

- Understanding the mechanism of the transfer of the microscopic instabilities that occur with the von Karman vortex shedding to the macroscopic field variables is important to be able to model the phenomenon.
- Including Heat Transfer to the problem to understand the influence of symmetry-breaking and porosity on the Nusselt Number. Theoretically, the heat transfer must be enhanced by the symmetry-breaking phenomenon since the vortices are smaller than in the case of symmetric flows. Vortices in porous media with low porosity act as an insulator of heat by reducing the contact surface for the incoming fluid.
- Can this phenomenon result in macroscale instabilities larger than the size of the pore scale when applied in a finite porous domain as a result of contrasting behavior in those zones that can be approximated as infinitely periodic?
- Validating the trend of macroscopic flow angle between the porosities of $0.72 \leq \varphi \leq 0.61$ where RANS and LES seem to predict quantitatively different variations.
- Extension to 3-D GPMs to investigate the underlying physics. 3-D GPMs are seen to induce a 3-D flow angle. The associated physics was observed to be quite complex.

6. REFERENCES

[1] T. Von Kármán, "Ueber den Mechanismus des Widerstandes, den ein bewegter Körper in einer Flüssigkeit erfährt," *Nachrichten von der Gesellschaft der Wissenschaften zu Göttingen, Math. Klasse*, 1911.

[2] M. E. Boghosian and K. W. Cassel, "On the origins of vortex shedding in two-dimensional incompressible flows," *Theor. Comput. Fluid Dyn.*, 2016.

[3] J. C. Schatzman, "A model for von karman vortex street," California Institute of Technology, 1981.

[4] W. W. Durgin and S. K. F. Karlsson, "On the phenomenon of vortex street breakdown," *J. Fluid Mech.*, 1971.

[5] M. F. Uth, Y. Jin, A. V. Kuznetsov, and H. Herwig, "A direct numerical simulation study on the possibility of macroscopic turbulence in porous media: Effects of different solid matrix geometries, solid boundaries, and two porosity scales," *Phys. Fluids*, vol. 28, no. 6, 2016.

[6] Y. Jin, M.-F. Uth, A. V. Kuznetsov, and H. Herwig, "Numerical investigation of the possibility of macroscopic turbulence in porous media: a direct numerical simulation study," *J. Fluid Mech.*, vol. 766, pp. 76–103, 2015.

[7] H. Iacovides, B. Launder, D. Laurence, and A. West, "Alternative Strategies for Modelling Flow over In-Line Tube Banks," in *Proceedings of the 8th International Symposium on Turbulence and Shear Flow Phenomena (TSFP-8)*, 2013.

[8] D. A. Nield and A. Bejan, *Convection in porous media*. 2013.

[9] J. Bear, "Dynamics of Fluids in Porous Media," *Soil Sci.*, 1975.

[10] M. J. S. de Lemos, *Turbulence in Porous Media*. 2006.

[11] Y. Jin and A. V. Kuznetsov, "Turbulence modeling for flows in wall bounded porous media: An analysis based on direct numerical simulations," *Phys. Fluids*, vol. 29, no. 4, 2017.

[12] F. Kuwahara, T. Yamane, and A. Nakayama, "Large eddy simulation of turbulent flow in porous media," *Int. Commun. Heat Mass Transf.*, 2006.

[13] D. Seguin, A. Montillet, and J. Comiti, "Experimental characterisation of flow regimes in various porous media-I: Limit of laminar flow regime," *Chem. Eng. Sci.*, 1998.

[14] D. C. Wilcox, *Turbulence Modeling for CFD (Second Edition)*. 1998.

[15] H. Tennekes, *A First Course in Turbulence*. 1972.

[16] S. B. Pope, *Turbulent Flows*, vol. 1. 2000.

[17] U. Svensson and K. Häggkvist, "A two-equation turbulence model for canopy flows," *J. Wind Eng. Ind. Aerodyn.*, vol. 35, no. C, pp. 201–211, 1990.

[18] H. Gao, C. Q. Qiu, D. Fan, Y. Jin, and L. P. Wang, "Three-dimensional microscale flow simulation and colloid transport modeling in saturated soil porous media," *Comput. Math. with Appl.*, vol. 59, no. 7, pp. 2271–2289, 2010.

[19] X. Lu, P. Xie, D. B. Ingham, L. Ma, and M. Pourkashanian, "A porous media model for CFD simulations of gas-liquid two-phase flow in rotating packed beds," *Chem. Eng. Sci.*, vol. 189, 2018.

[20] M. J. S. De Lemos, *The Double-Decomposition Concept for Turbulent Transport in Porous Media*. 2005.

[21] M. H. J. Pedras and M. J. S. de Lemos, "On the definition of turbulent kinetic energy for flow in porous media," *Int. J. Heat Mass Transf.*, vol. 27, no. 2, pp. 211–220, 2000.

[22] D. B. Ingham and I. Pop, *Transport Phenomena in Porous Media*. 1998.
[23] D. B. Ingham and I. Pop, *Transport phenomena in porous media II*. 2002.
[24] D. B. Ingham and I. Pop, *Transport Phenomena in Porous Media III*. 2005.
[25] C.-W. Huang, T. S. Su, V. Srikanth, and A. V. Kuznetsov, "A STUDY OF THE EFFECTS OF THE PORE SIZE ON TURBULENCE INTENSITY AND TURBULENCE LENGTH SCALE IN FORCED CONVECTION FLOW IN POROUS MEDIA," in *Proceedings of the 16th International Heat Transfer Conference, IHTC-16*.
[26] T. H. Shih, W. W. Liou, A. Shabbir, Z. Yang, and J. Zhu, *A new k-ε turbulent eddy viscosity model for high reynolds number turbulent flows*, vol. 24, no. 3. 1995.
[27] ANSYS Inc., "ANSYS FLUENT Theory Guide," *Release 17.2*. 2016.
[28] ANSYS, *ANSYS Fluent User's Guide*. 2016.
[29] W. Rodi, "Comparison of LES and RANS calculations of the flow around bluff bodies," *J. Wind Eng. Ind. Aerodyn.*, vol. 69–71, pp. 55–75, 1997.
[30] P. Moin and T. Sayadi, "A comparative study of subgrid scale models for the prediction of transition in turbulent boundary layers," *Cent. Turbul. Res. Annu. Briefs*, pp. 237–247, 2010.
[31] M. Breuer, "Large eddy simulation of high reynolds number circular cylinder flow," in *Industrial and Environmental Applications of Direct and Large-Eddy Simulation. Lecture Notes in Physics*, 1999.
[32] L. Davidson and S. Krajnovic, "Flow around a three-dimensional bluff body," in *9th International Symposium on Flow Visualisation*, 2000, no. 177, p. 177(1--10).
[33] A. Abba, C. Cercignani, and L. Valdettaro, "Analysis of subgrid scale models," *Comput. Math. with Appl.*, vol. 46, no. 4, pp. 521–535, 2003.
[34] H. Werner and H. Wengle, "Large-Eddy Simulation of Turbulent Flow Over and Around a Cube in a Plate Channel," in *Turbulent Shear Flows 8*, 1993, pp. 155–168.
[35] W.-W. Kim, S. Menon, W.-W. Kim, and S. Menon, "Application of the localized dynamic subgrid-scale model to turbulent wall-bounded flows," in *35th Aerospace Sciences Meeting and Exhibit*, 1997.
[36] M. Germano, U. Piomelli, P. Moin, and W. H. Cabot, "A dynamic subgrid-scale eddy viscosity model," *Phys. Fluids A*, vol. 3, no. 7, pp. 1760–1765, 1991.
[37] ANSYS Inc., "ANSYS, HLRS And Cray Set New Supercomputing Record," 2016. [Online]. Available: https://www.ansys.com/about-ansys/news-center/11-15-16-ansys-hlrs-cray-set-new-supercomputing-record.
[38] HPC Advisory Council, "ANSYS Performance Benchmark and Profiling," 2010. [Online]. Available: http://www.hpcadvisorycouncil.com/pdf/ANSYS_Performance_Analysis.pdf.
[39] P. Moin and K. Mahesh, "DIRECT NUMERICAL SIMULATION: A Tool in Turbulence Research," *Annu. Rev. Fluid Mech.*, vol. 30, no. 1, pp. 539–578, 1998.
[40] H. Choi and P. Moin, "Grid-point requirements for large eddy simulation: Chapman's estimates revisited," *Phys. Fluids*, 2012.
[41] D. R. Chapman, "Computational Aerodynamics Development and Outlook," *AIAA J.*, vol. 17, no. 12, pp. 1293–1313, 1979.
[42] R. Peyret and E. Krause, *Advanced Turbulent Flow Computations*. New York: Springer-Verlag, 2000.
[43] R. I. Issa, "Solution of the implicitly discretised fluid flow equations by operator-splitting," *J. Comput. Phys.*, vol. 62, no. 1, pp. 40–65, 1986.

[44] S. V. Patankar, “Numerical Heat Transfer and Fluid,” *Washington, DC, Hemisphere Publishing Corp., 1980. 210 p*. pp. 25–27, 1980.
[45] I. B. Celik, Z. N. Cehreli, and I. Yavuz, “Index of Resolution Quality for Large Eddy Simulations,” *J. Fluids Eng.*, 2005.